Departament d'Enginyeria Electrònica
UNIVERSITAT POLITÈCNICA DE CATALUNYA

Silicon heterojunction solar cells obtained by Hot-Wire CVD

Delfina Muñoz Cervantes

Director: Cristóbal Voz Sánchez

Memòria presentada per a
l'obtenció del títol de Doctor

Barcelona, juliol de 2008

A mi padre, mi madre, Andrés y la Mari

"Would you tell me, please, which way I ought to go from here?"
"That depends a good deal on where you want to get to," said the Cat.
"I don't much care where –" said Alice.
"Then it doesn't matter which way you go," said the Cat.
"– so long as I get *somewhere*," Alice added as an explanation.
"Oh, you're sure to do that," said the Cat, "if you only walk long enough."

L. Carroll, Alice's Adventures in Wonderland

“¿podrías decirme, por favor, qué camino debo seguir para salir de aquí?”
“Esto depende en gran parte del sitio al que quieras llegar” dijo el Gato.
“No me importa mucho el sitio...” dijo Alicia.
“Entonces tampoco importa mucho el camino que tomes,” dijo el Gato.
“...siempre que llegue a *alguna parte*” añadió Alicia como explicación.
“¡Oh, siempre llegarás a alguna parte,” aseguró el Gato, “si caminas lo suficiente!”

L Carroll, Alicia en el Pais de las Maravillas

Summary

Aknowledgments

Acronym list

Aknowledgments, agradecimientos, agraïments & remerciements

"No hables si lo que vas a decir no es más hermoso que el silencio"
(Proverbio árabe)

Primero de todo, agradecer agradecer a Ramon Alcubilla haberme motivado a incorporarme al Grup de Micro i Nanotecnologies del Departament d'Enginyeria Electrònica de la Universitat Politècnica de Catalunya lo cual ha permitido desarrollar esta tesis en el campo de dispositivos fotovoltaicos.

Gracias también al doctor Cristóbal Voz por dirigirme en el camino de esta tesis, en especial por su apoyo y entusiasmo durante todo este periodo.

También me gustaría agradecer enormemente a Albert Orpella, Isidro Martín, Kim Puigdollers y Michael Vetter todos los momentos compartidos dentro y fuera de la Sala Blanca, las discusiones, los cafés, las sugerencias y el apoyo incondicional.

Tampoco me puedo olvidar de todos los que compartimos la sala 213, todos los que han pasado por allí forman parte de esta tesis de alguna manera u otra y especialmente los que más me habéis apoyado en este camino. Gracias Rafa por estar siempre ahí delante, Moisés por buscar siempre una respuesta o una pregunta, Mónica por ese hombro, Jordi por el apoyo continuo en todo, Gemma por tener siempre un sí, Lukasz, Enrique, David, Gerard, por compartir comidas y cafés. Sin olvidar los que ya estáis en un despacho más grande, Sandra y Pablo. Ni tampoco los que estabais o estáis repartidos por otros despachos, Servane, Triffon.

Esta tesis tampoco hubiera sido posible sin la ayuda los técnicos de la Sala Blanca de la UPC Miguel, Xavi y Javi que siempre han estado dispuestos a ayudarme, ni sin el apoyo de Vicente siempre disponible para hacer máscaras. Gracias a todos.

Por otra parte, esta tesis no hubiera sido posible sin el apoyo de todo el equipo del Departament de Fisica Aplicada i Òptica de la Universitat de Barcelona. Quiero agradecer primero al Dr. Lloret el haberme presentado al Grup d'Energia Solar de la UB. Dentro de este grupo agradecer al Dr. Jordi Andreu su entusiasmo por las HITs y al Dr. Joan Bertomeu su comprensión. El HWCVD para mí va ligado a varios nombres de todos los que me enseñasteis sus misterios. Gracias Marta y David por vuestros primeros pasos y las horas dedicadas con alegría, y gracias Fernando por la paciencia y compartir todo este camino. Agradecer también a Jordi Escarré su presencia continua y su disponibilidad inmediata. Gracias también a los que me habéis acompañado en esta última etapa en la UB, Jose Miguel, Aldrin, Paolo, Dani, Silvia, Paz, Oriol, Marco, Freddy, Rubén, Mike, Silvia M., por enseñarme el apasionante mundo de los físicos.

Gracias a los que habés hecho estas últimas correcciones de inglés, Mike, Aldrin, Oriol y Marta.

Merci aussi a tout l'équipe du Laboratoire de Physique des Interfaces et des Couches Minces de l'École Polytechnique, spécialement au Professeur Pere Roca i Cabarrocas pour m'accepter pendant tous les séjours au laboratoire et discuter tous les résultats d'ellipsometrie même si les couches soaient obtenus par HWCVD. Merci a tous qui ont partagé le chemin français de la thèse, Enric, Jerôme, Fatiha, Yassine, et tous les autres...

Gràcies també al CerMAE-XarMAE per recolzar aquest projecte i a l'AGAUR de la Generalitat de Catalunya. Sense el seu suport amb les diferents beques aquest treball no hauria estat possible.

> *"He disfrutado mucho con esta obra de teatro, especialmente en el descanso"*
> *G. Marx*

Durante esta tesis ha habido mucha gente que ha participado directa o indirectamente fuera del ámbito propiamente universitario que me ha hecho disfrutar de este camino.

Gracias a todos los que habéis compartido conmigo el mundo de la cooperación. Gracias al equipo Vedanthangal, especialmente a Pep, Jordi y Anna por compartir viaje a Chittatur. Gràcies Montse, Xavi, Emi i al CCD per recolzar aquests projecte. Gràcies a Vedanthangal per fer-me ser feliç en el món de la cooperació. Thanks also to the CCDT in Mumbai, Sara, Amin and all the children, women and staff.

Tampoco puedo olvidar a quien me enseñó lo que era la energía solar en Perú. Gracias Miguel por hablarme de renovables, Alex por estar ahí, rodeado de sol y energía y Eduardo por tu siempre buen consejo. Gracias a todo el Grupo de Apoyo al Sector Rural por enseñarme la parte práctica de la energía.

Gracias también a la música y los que acompañáis en el camino del arte. Gracias Ferran y Ana por vivir conmigo el teatro y la música, Biel, Marc, Jordi por el circo y la música, Fede por la danza y la música, gracias a todos los compañeros de Artmúsic, Joan y Marta, y a todos mis maravillosos alumnos, especialmente la Mari.

Dar las gracias a todos los amigos que habéis acompañado este camino haciéndolo más alegre, Marta, Elena, Soraya y Jerome, Mar, Sara, Eze, Ramon, Pep, Annas i patrullerus, Sonia, Ana y Save, Antonia, Paula, Gloria, Gordana y todos los que me habéis dado una sonrisa, echado una mano o dado un abrazo.

Finalmente dar las gracias a los que siempre estáis ahí. Gracias a mi familia. Gracias mamá, papá, Andrés y Mari. Y gracias, Biel.

Acronym list

α: optical absorption coefficient

Al-BSF: aluminum back-surface-field

AFM: Atomic Force Microscopy

AM1.5: Air Mass 1.5

a-Si:H: hydrogenated amorphous silicon

c-Si: crystalline silicon

Cat-CVD: Catalytic Chemical Vapour Deposition

C_H: hydrogen content

C_O: oxygen content

CVD: Chemical Vapour Deposition

CZ: Czochralski

d: thickness

$d_{f\text{-}s}$: distance filament-substrate

D_H: hydrogen dilution

Δn: Excess minority carrier density

ε: pseudodielectric function, dielectric constant of silicon

ε_2: imaginary part of the pseudodielectric function

E_a: dark conductivity activation energy

E_c: conduction band level

E_F: Fermi level

E_g: optical band gap

E_v: valence band level

EQE: External Quantum Efficiency

Φ: flux, work function

FF: fill factor

FTIR: Fourier Transform Infrared spectroscopy

FZ: Float Zone

G_S: grain size

η: solar cell efficiency

HIT: heterojunction with intrinsic thin layer

HWCVD or Hot-Wire CVD: Hot-Wire Chemical Vapour Deposition

ITO: Indium Tin Oxide

IQE: Internal Quantum Efficiency

J: current density

J_{dio}: diode current density

J_{ph}: photogenerated current density

J_{rec}: recombination current density

J_{sc}: short circuit current density

L_D, L_{eff}, L_n: effective diffusion lengths

μ: mobility

μc-Si:H: hidrogenated microcrystalline silicon

$\mu\tau$: mobility-lifetime product

n_0: refraction index

N_A, N_D: impurity, doping

PDS: Photothermal Deflection Spectroscopy

PECVD: Plasma-Enhanced Chemical Vapour Deposition

pm-Si:H: polymorphous silicon

QSSPC: Quasy-Steady-State Photoconductance

ρ: resistivity

r_d: deposition rate

R: recombination rate

R^*: microstructure factor

RF: radio frequency

R_{oc}: open circuit resistance

R_p: parallel resistance

R_s: series resistance

R_{sc}: short circuit resistance

S_{it}, S_{eff}: effective recombination velocity

S_{0back}: back surface recombination velocity

SE: Spectroscopic Ellipsometry

SR: Spectral Response

TCO: Transparent Conductive Oxide

TEM: Transmission Electron Microscopy

T_f: filament temperature

T_s: substrate temperature

U: recombination process

V_{oc}: open-circuit voltage

σ_d: dark conductivity

V_{bi}: built-in voltage

τ_{eff}: effective lifetime

X_c: crystalline fraction

χ: electron affinity

XRD: X-Ray Diffraction

Chapter 1: Introduction

"Have you ever thought about what you would have to give up or how much work and effort you would have to dedicate to daily activities if electricity did not help you?"

1.1 The Energy problem

The global energy system faces three major strategic challenges in the coming decades: the growing risk of disruptions to energy supply because of the increasing population; the threat of environmental damage caused by energy production and use; and persistent energy poverty. The first two challenges have attracted a lot of attention from the energy-economics community, much less so the need to address the problem of energy under-development. Based on current trends, the number of people in poor countries relying primarily on traditional biomass for their energy needs will continue to rise, while the number of lacking access to electricity will barely fall.

"A quarter of the world's people, 1.6 billion, have no electricity to power an electric light" (United Nations, Energy Report)

Analyzing the United Nations (UN) Goals, energy plays one of the most important roles. Energy has strong links with poverty reduction: health, education gender and environment and also with community social-economic development. In fact, energy is a challenge for achieving the Millennium Developments Goals. In figure 1.1 a map of the world is deformed as a function of the poverty distribution. The increase of the African and South Asian territories is clear and in constrast, Europe and North America almost disappear.

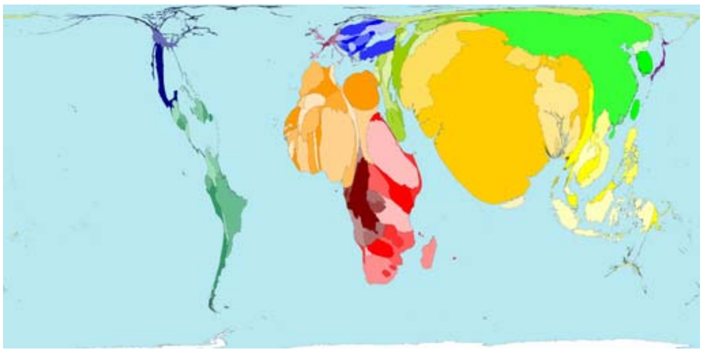

Figure 1.1: Territory size shows the proportion of the world population in poverty living there (calculated by multiplying population by one of two poverty indices [http://www.worldmapper.org/]. The human poverty index uses indicators that capture non-financial elements of poverty, such as life expectancy, adult literacy, water quality, and children that are underweight. [http://hdr.undp.org]).

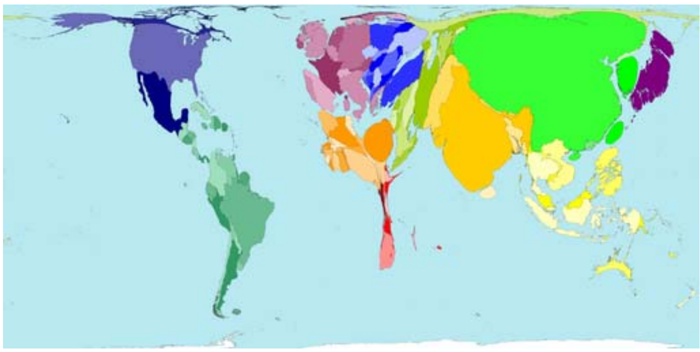

Figure 1.2: Territory size shows the proportion of all people with some electrical power in their homes living there [http://www.worldmapper.org/]. Electricity access includes that sourced from a publicly used grid and self-generated electricity. This map shows access, not the quantities of electricity used. The percentage of people with access to electricity in their own homes is over 97% in Eastern Asia, Eastern Europe, North America, Western Europe and Japan. 7 of the 10 territories with the lowest access to electricity are in Africa.

On the contrary, if we look at figure 1.2, we can see the deformed world map, but in this case, taking into account the electricity supply to the homes in the world. Most of the electricity-deprived are in sub-Saharan Africa and south Asia. For these people, the day finishes much earlier than in richer countries due to lack of proper lighting. They struggle to read by candle light. They lack refrigeration for keeping food and medicines fresh. Those appliances that they do have are powered by batteries, which eat up a large share of their incomes. Another hallmark of energy poverty is the use of traditional biomass in unsustainable, unsafe and inefficient ways. Currently, 2.5 billion people – 40% of the world's population – rely on traditional biomass such as wood, agricultural residues and dung to meet virtually all their cooking energy needs [Birol, 2007]. In many countries, these resources account for over 90% of all household energy consumption. These people live mainly in rural areas of Asia and Africa. The use of biomass is not in itself a cause for concern. But, in practice, it has a number of harmful consequences for health, the environment and economic and social development. People, most often women and children, can spend many hours gathering such fuels. This reduces the time they can devote to more productive activities, such as farming and education. Wood gathering can also lead to deforestation, resulting in local scarcity of fuel wood and severe damage to the ecosystem. In addition, reliance on traditional biomass has a direct impact on human health. The World Health Organization estimates that each year, 1.3 million people – again, mostly women and children – in developing countries die as a result of fumes from indoor biomass stoves. Only malnutrition, HIV/AIDS and lack of clean water and sanitation are greater health threats.

Consequently, meeting basic human needs, such as food and shelter, must be at the heart of any strategy to alleviate poverty. Energy services help enable those needs to be met. Indeed, access to energy is a prerequisite to human development. It contributes to social development by improving health and education and to economic development by enhancing the productivity of labour and capital.

But the main problem is that the energy system as it is established nowadays, cannot supply energy for everybody. A non distributed system based on fossils fuel absolutely politically controlled makes the access to energy to the developing countries difficult [Scheer, 2002]. So, apart from strong political will and commitment on the part of the governments to break the vicious circle of energy poverty and human under-development, investigation and research on new renewable resources (affordable for the poorest countries and non dependant from energy production countries) has to be done to allow the development of all the regions in the world.

"The Earth temperature will increase between 1.5ºC and 4ºC in the next 50 years due to the high presence of greenhouse gases caused by the human activities"

(IPCC, 2007)

Current trends in energy supply also carry the threat of severe and irreversible environmental damage – including changes in global climate. If unchecked, energy-related emissions of carbon dioxide will rise broadly in line with fossil-fuel use through to 2030, i.e. by more than half. The bulk of the increase will come from developing countries. The use of low- or zero-carbon renewable energy sources is set to expand rapidly, but emissions will be driven higher by the inexorable growth in consumption of fossil energy, especially coal. The latest work by scientists on the potential consequences of rising concentrations of greenhouse gases in the atmosphere and by economists on the costs of inaction should leave us in no doubt that the energy path we are currently on is far from being sustainable [IPCC, 2007].

"Yet there is a solution: to make the transition to renewable sources of energy and distributed, decentralized energy generation" (Scheer)

Renewable energy sources came from external sources to the Earth, primarily from the sun. Their basic property is that renewable sources do not run out, in contrast to conventional energy sources based on fossils fuel as carbon, petrol and gas. Mainly, we can consider five basic renewable energy sources: wind, biomass, geothermal, hydrodynamic and solar energy (both, thermal and photovoltaic). All of these forms of energy are in principle capable of producing large quantities of electricity for present as well as for future use. The strong points of these forms of energy production are:

- their environmentally friendly nature, as they do not contribute to the production of carbon dioxide or other greenhouse gasses.
- they allow an energy - distributed scenario, they can supply energetically poor areas avoiding the energy dependence on other countries.
- these sources for energy production are available in nearly ever-lasting abundance.

Many studies have been performed considering different scenarios for energy production and consumption for the next few decades [World Energy Outlook, 2004]. The WEO projections of energy demand and supply are subject to a wide range of uncertainties including macroeconomic conditions, resource availability, technological developments and investment flows as well as government energy and environmental policies. An increase in the use of renewable sources is always present to satisfy the demand of energy in the next decades. In table 1.1, a moderate prediction of the world energy consumption is shown. Although the percentage of the renewable sources is the same, the total energy production is double than in 2002. Furthermore, a decrease of the traditional biomass is expected, a sign of relative development in cooking technologies in the third world countries.

	2002		2030	
	Renewable use (Mtoe)	Share of total demand (%)	Renewable use (Mtoe)	Share of total demand (%)
Biomass	1119	11	1605	10
of which traditional biomass	765	7	907	6
Hydro electrical	224	2	365	2
Other renewable	55	1	256	2
Total	**1398**	**14**	**2226**	**14**

Table 1.1: World Renewable energy consumption in 2002 and prediction for 2030 in a standard scenario [WEO, 2004].

Wind, geothermal and solar technologies have to multiply their energy generation by a factor of 5 to supply the demanded energy. In particular, electricity generation from photovoltaic systems is expected to reach 100 TWh in 2030 [WEO, 2004]. The environmental advantages in terms of architectural integration, zero CO_2 emissions and low visual impact make it a good alternative relative to other sources in lot of applications, especially for domestic decentralized power stations. But nowadays, even more than other renewable sources, the PV technology is very expensive compared with fossil standard technologies. Even though, due to the great potential of solar power, further efforts are being made to achieve reasonable economic goals.

1.2 Photovoltaic energy in the world

The use of photovoltaic systems on a large scale in order to reduce fossil fuel consumption and greenhouse gas emissions requires that the energy associated with the construction, operation and decommissioning of PV systems be small compared with energy production during the system lifetime. That is, the energy payback time should be short. Over the next few decades at least the energy used to construct PV systems will be derived primarily from fossil fuels. In the long term "solar breeding" will be possible, whereby energy for the production of PV systems will be derived from PV systems. This will reduce or eliminate carbon dioxide emissions associated with PV system manufacture.

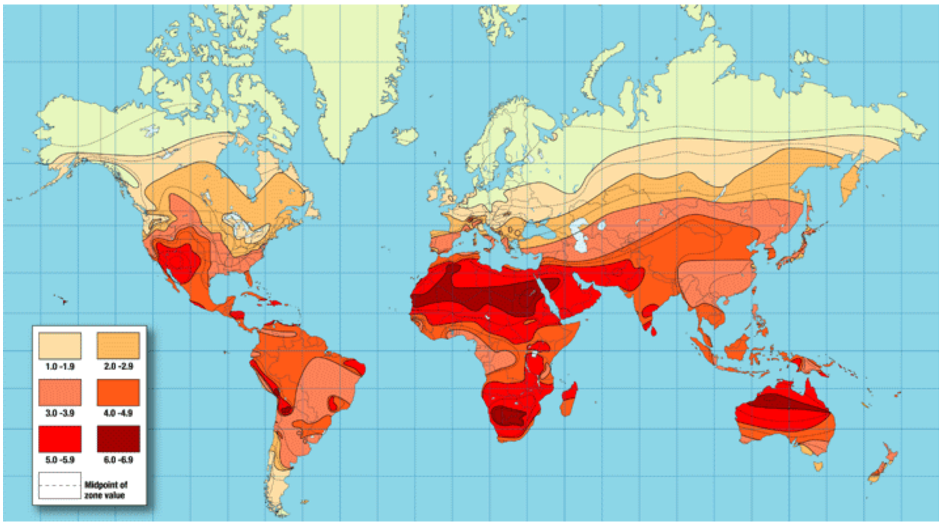

Figure 1.3: Amount of solar energy in hours, received each day on an optimally tilted surface during the worst month of the year.

In figure 1.3 a solar irradiation map is shown with the amount of solar energy in hours, received each day on an optimally tilted surface during the worst month of the year. The amount of solar energy reaching the earth every year is roughly 10^{24} J. This is more than a thousand times the annual energy consumption of the entire world, indicating that (in principle) the worldwide requirement for energy could be supplied by solar energy.

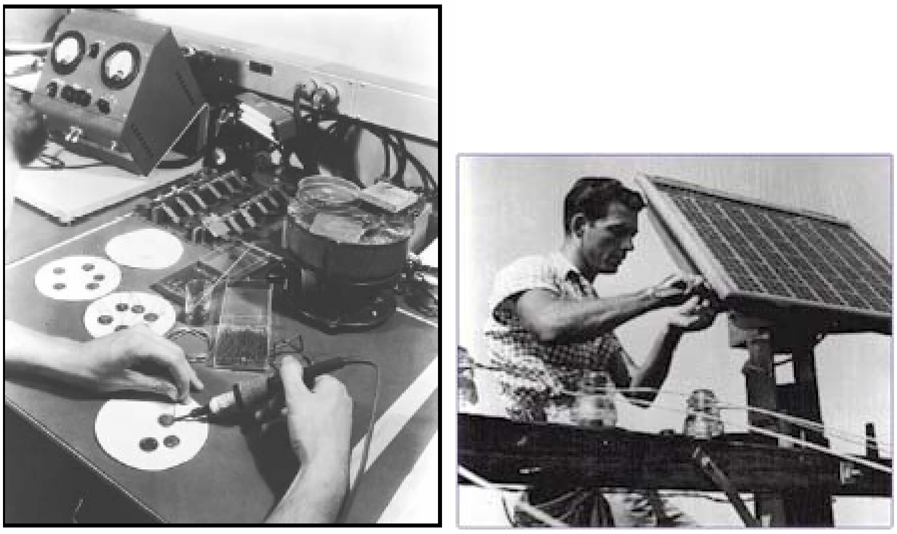

Figure 1.4: First solar cells and modules by Bell laboratories [Chapin et al., 1954].

The principle of this energy conversion is based on the photovoltaic (PV) effect: if the energy of an incident photon is larger than the bandgap Eg of a semiconductor, an electron can be excited to the conduction band leaving behind a hole in the valence band. Thus, free charge carriers are generated, which can be collected in an external circuit so that the electrical energy can be used. The first solar cells on silicon -Fritts has fabricated the first ones on thin selenium wafers with an efficiency < 1% [Fritts, 1883]- were fabricated by the Bell laboratories in 1954 with 6% efficiency [Chapin et al., 1954]. In figure 1.4, a picture of the first solar cells and module is shown. Nowadays, although other technologies have appeared in the world panorama, panels based on crystalline silicon wafers (mono-Si, multi-Si or ribbon technologies) still have more than 90% of the world market [Fthenakis et al., 2006]. The Energy Pay-Back Times (EPBT) of such systems is respectively, 1.7, 2.2, and 2.7 years for ribbon, multi-, and mono-Si technology for average southern Europe irradiance (1700 kWh/m2/yr) and 75% performance ratio. Considering typical system lifetimes of around 30 years, it is seen that, even for the most energy intensive of these four common photovoltaic technologies, the energy required for producing the system does not exceed 10% of the total energy generated by the system during its anticipated operational lifetime [*http://www1.eere.energy.gov/solar/pv_basics.html*]. Nevertheless, strong efforts are being done to diminish even more the EPBT especially on the solar cell fabrication (more than 80% of the total cost).

It is important to remark that more than 50% of the solar cell fabrication cost is related to the production of the raw material, the c-Si wafer [Knapp et al., 2001]. To date, the PV industry has been strongly dependent on the electronics industry to obtain cheap substrates using rejected silicon wafers. Two parameters negatively affect this dependence: the cyclic activity of the electronics industry (varying the price of the silicon) and the strong increase in the activity of the PV industry saturating the market [Goetzberger et al., 2002]. Hence, the lack of silicon for PV applications has accelerated the research on alternative materials and processes to the standard technology of c-Si solar cells.

1.3 Solar cell technologies

As concluded in the previous section, the interest in cost reduction combined with the actual lack of crystalline silicon has stimulated research on alternatives to the classical solar cell fabrication process. In this sense, M. Green has summarized the requirements for a photovoltaic technology to be successful in the long-term. Based on the argument that high production volumes will automatically result in total costs approaching the material costs, these requirements are: (1) thin-film; (2) high-efficiency; (3) non-toxic; (4) based on abundant materials, and (5) durable [Green, 2006].

Nowadays, the investigation in PV technologies can be grouped in three major areas [Goetzberger et al., 2003]:

a) Alternative materials

Organics: They have relatively low conversion efficiencies, in the range of 5 percent for non-commercial solar cells. Their introduction in the market is still a long term prospect because of the difficulty to obtain stable devices, although the fabrication process is quite simple [Peumans et al., 2003].

Germanium: It has a structure similar to silicon but a thinner band gap. The obtained efficiencies do not exceed those of a c-Si solar cell, while the fabrication process is similar. Nevertheless, germanium-silicon alloys can be stacked in multijunction solar cells. Then, each layer responds to different wavelengths of the sunlight because they have a different band gap. Hence, efficiencies can go beyond the limits of a single junction solar cell (> 30%) [Green et al., 2006].

Cadmium Telluride/Selenide (CdTe/CdS): These materials are strong light absorbers with an optimum band-gap of 1.44 eV. Hence, the main advantage is that layers only need to be about 1μm thick and materials costs can be significantly reduced [Hamakawa, 2004]. Efficiencies close to 10% have been achieved in commercial modules by Solar Cells Inc. [Rose et al., 2000]. Moreover, Colorado State Univ. has recently announced the construction of a plant together with AVA Solar Inc. where panels will cost less than $1 per watt peak [http://www.avasolar.com/]. Nevertheless, a concern often expressed about CdS/CdTe solar cells is the effect of cadmium on health and the environment.

Copper Indium (Gallium) Diselenide (CIS or CIGS): Although they have some terrestrial applications especially in concentrator systems, they are mainly valuable for powering space satellites. They are usually fabricated as multi-junction structures, with a record-setting efficiency of 40.7% achieved by Spectrolab-Boeing using concentration [Hering, 2007]. The four major challenges for CIS/CISG solar cells are: reducing manufacturing costs by simplifying and standardizing equipment and processes; understanding and controlling the electronic properties; developing alternate window layers (Cd-free); and developing wider band gap materials [Hegedus, 2006].

III-V semiconductors (GaAs, AlGaAs…): They are the most expensive devices, although they have achieved record efficiencies. They are the most used in aerospace applications. Their major goal is the possibility to use concentrators to diminish the area of the device. Using concentrators, record efficiencies of over 42% have been obtained.

b) Thin film a-Si:H and μc-Si:H solar cells

Hydrogenated amorphous silicon p-i-n solar cells are one of the most studied alternatives because of the abundance of the material. The highest independently confirmed stabilized efficiency is 12.1%, although commercial modules have stabilized efficiencies of 6–7% [Hegedus, 2006]. The three major challenges for a-Si:H technology are: to increase the stabilized module efficiency to 10–12%; to minimize or eliminate the self-limiting degradation; and to increase the film deposition rate without sacrificing performance.

Furthermore, the multi-junction technology can be also applied combining a-Si:H with μc-Si:H solar cells. Promising results with stable efficiencies up to 13% have been obtained in triple stack a-Si:H/μc-Si:H/μc-Si:H solar cells. These devices are less sensitive to photodegradation, and can reach module efficiencies of up to 12% [Yamamoto et al., 2005].

c) Alternative c-Si solar cells

In spite of the economic problems previously mentioned, crystalline silicon as a base material in the PV industry for terrestrial applications continues to be a good alternative. The good properties of c-Si in terms of low degradation, low environmental impact, abundance as raw material and feasibility to reach high efficiencies are remarkable. The 24.7% world record efficiency on c-Si has been published by the group of M. Green with the so-called PERL structure (figure 1.5) [Zhao et al., 1999]. Although this result reflects a great technological development, it is a long, complicated and expensive fabrication process. Consequently, there are different lines of investigation aiming to reach similar efficiencies but with drastically reduced costs.

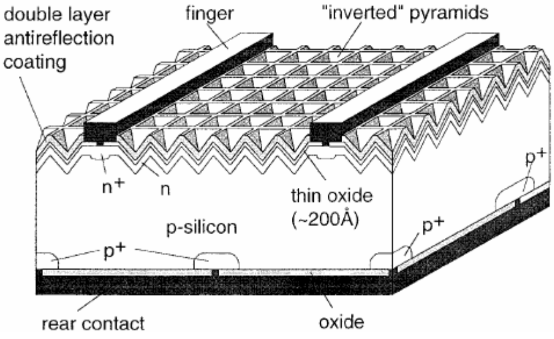

Figure 1.5: PERL (passivated emitter, rear locally-diffused) solar cell structure fabricated by the group of M. Green at University of New South Wales [Zhao et al., 1999].

One solution is to use low quality silicon prepared especially for the photovoltaic industry: *solar-grade* silicon. This is already being carried out in the industry with multicrystalline silicon. Approximately 30% of the present production of modules is based on multicrystalline silicon. This alternative is cheaper than monocrystalline silicon, but the module efficiency (15.3% record [King et al., 1994]) is still far from that obtained with c-Si (22.7% record [Zhao et al., 1997] and 19.7% on very large area [Rose et al., 2006]). On the other hand, other investigation lines focus their efforts on reducing not the quality but the quantity of silicon by using thinner wafers (figure 1.6). The main problem of thin wafers is their tendency to warp at the high temperatures (~ 1000ºC) involved in the standard fabrication process. Low cost multicrystalline silicon wafers are not compatible with high temperature steps either, but in this case due to strong lifetime degradation [Schultz, 2004].

Figure 1.6: Very thin solar cell (20.2% on 37μm) fabricated at ISE. They have also the record 21.2% on a 75μm wafer without wafer warpage [Glunz et al., 2005].

Therefore, low temperature surface passivation schemes using thin films of hydrogenated amorphous silicon (a-Si:H) [Kunst et al., 2002], [Voz et al., 2003], silicon carbide (a-SiC$_X$:H) [Martin et al., 2001] or silicon nitride (a-SiN$_x$:H) [Lauinger et al., 1996], [Leguijt et al., 1996] have gained special interest due to their compatibility with both thin and low quality c-Si substrates. The heteroestructure formed between a-Si:H and c-Si is particularly interesting, since intrinsic films can be used for passivation and doped ones to form either the heterojunction emitter or the back contact. In this sense, double-side heterojunction devices can be fabricated in a fully low temperature process.

1.4 Development of silicon heterojunction solar cells

The investigation of heterojunction silicon solar cells started in 1974 when Fuhs et al. first proposed to use heterojunctions of amorphous silicon emitter on a crystalline substrate for solar cells [Fuhs et al., 1974]. Then, in 1985 the first heterojunction solar cell was fabricated [Hamakawa et al., 1985]. From this moment, many research groups worldwide were interested in the technological development of a-Si:H/c-Si heterojunctions as an alternative to traditional diffused emitters. The heterojunction is formed by depositing a thin a-Si:H layer on the c-Si wafer at temperatures typically below 200ºC. In addition, it is a simple process with a relatively low manufacturing cost. The potential of this technology was definitely demonstrated by Sanyo in 1991 with the structure denominated HIT (Heterojunction with Intrinsic Thin layer) [Iwamoto et al., 1991] that has been continuously developed resulting in an outstanding 22% efficiency in 100 cm^2 solar cells [Taguchi et al., 2005], [*http://us.sanyo.com*]. Moreover, Sanyo has also achieved 19.5% efficiencies in mass produced modules [Tanaka et al., 2003]. The main difference compared to the first heterostructures is the inclusion of a thin intrinsic amorphous silicon layer between the doped layer and the wafer to improve the properties at the interface. Besides, Sanyo has applied the HIT concept also to low temperature BSF contacts, as in the bifacial device shown in figure 1.7. These solar cells are fabricated on CZ n-type wafers of thickness 250 μm. The deposition technique used for all the a-Si:H layers is Plasma Enhanced Chemical Vapour Deposition (PECVD). The device is finished with the deposition of a TCO antireflective coating followed by the metallic electrodes. Most details about the fabrication process have not been revealed by the company.

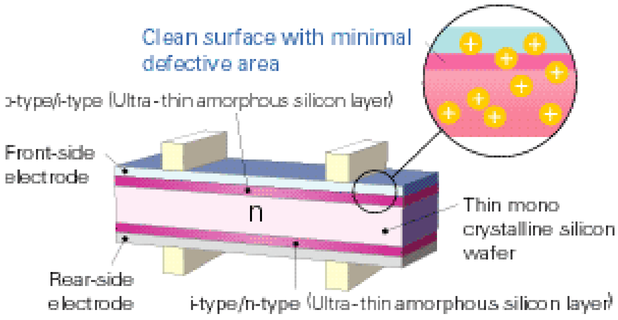

Figure 1.7: Structure of the bifacial heterojunction solar cells fabricated by Sanyo.

The main advantages of heterojunction devices are summarized next:

- *Potential for high efficiency solar cells:* as demonstrated by Sanyo with excellent results and competitive technology in the present market.
- *Good passivation properties:* given by the amorphous silicon used either as heterojunction emitter or low temperature BSF. The deposition conditions of the material can be optimized in order to obtain the desired properties in the final device.
- *Excellent stability*: the base material of the structure continues to be crystalline silicon. In this way, the typical degradation (Staebler-Wronski effect) observed in amorphous silicon solar cells does not take place. Actually, the extremely thin a:Si-H layers do not contribute to power generation and have only an interface passivation purpose.
- *Low temperatures throughout the process* (< 200ºC) that will allow technological development with thin or low quality crystalline silicon wafers.
- *Simplicity of the process*: The fabrication process is conceptually the same for the emitter and the BSF contact, not only regarding a-Si:H deposition but also the TCO and metallic contacts on both sides. Thus, the fabrication time is less than that usually required for commercial standard cells. Figure 1.8 shows the scheme of the fabrication process of a conventional solar cell compared with the heterojunction device.
- *Low technological cost*: low energetic cost (low temperature process) and less resources used.
- *Better response with operating temperature*: Sanyo has demonstrated that HIT solar cells are less affected by high operating temperatures than conventional solar cells. This is a great advantage; since the decrease in the module efficiency due to high operating temperatures is still one of the most important problems to solve in photovoltaic installations [Taguchi et al., 2000].

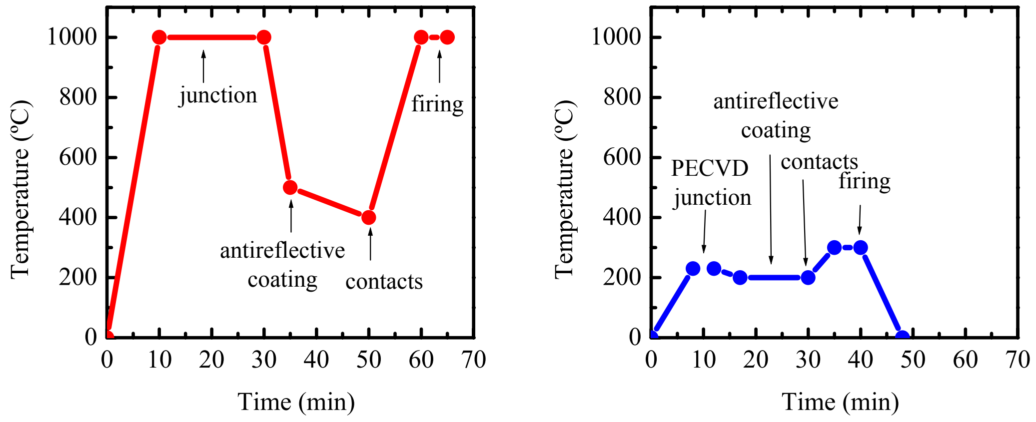

Figure 1.8: Scheme of the fabrication steps for a conventional solar cell compared to a heterojunction device. The temperatures involved in the different fabrication steps are indicated [Roca et al., 2004].

Motivated by the excellent results obtained by Sanyo, there is a high research acitivity in heterojunction solar cells. A summary of the best bifacial heterojunction solar cells reported to date is presented in table 1.2.

Reference	group	wafer			Solar cell parameters				a-Si:H Deposition technique
		type	resistivity (Ω×cm)	surface	V_{oc} (mV)	J_{sc} (mA/cm^2)	FF (%)	η (%)	
http://us.sanyo.com	Sanyo	N	?	textured	722	38.64	78.8	22	PECVD
Schmidt et al., 2007	HMI	P	1-2	textured	639.4	39.26	78.9	19.8	PECVD
Damon-Lacoste, 2007	LPICM	P	14	flat	664	33	77.8	17.1	PECVD
Feschet L. et al., 2007	IMT Neuchatel	N	1	flat	682	34	82	19.1	VHF-PECVD
Olibet et al., 2007		P	0.5	flat	690	32	74	16.3	VHF-PECVD
Page et al., 2006	NREL	P	1	textured	658	35.84	78.4	18.5	HWCVD

Table 1.2: Summary of the best results obtained to date in bifacial heterojunction solar cells.

Also by the PECVD deposition technique but using p-type wafers, the group at the Hahn-Meitner-Institut Berlin (HMI) [Schmidt et al., 2007] has obtained a remarkable 19.8% efficiency in bifacial solar cells fabricated on textured substrates. It is also worth considering the result obtained at LPICM-Ecole Polytechnique with a high V_{oc} of 664 mV [Damon-Lacoste J., 2007]. The lower efficiency of 17.1% can be mainly attributed to the lower J_{sc} value obtained with non-textured wafers.

Excellent results have been also presented by the Institute of Microtechnique (IMT) at Université de Neuchatel. This group has great experience in amorphous silicon thin film solar cells fabricated by the Very High Frequency PECVD technique. This deposition method allows higher deposition rates and is less aggressive than the conventional PECVD technique. Thus, less interface damage is expected, which is very desirable for heterojunction devices. They have worked with both n- and p-type wafers, obtaining excellent V_{oc} values only surpassed by Sanyo [Feschet L. et al., 2007] and efficiencies over 19% on n-type wafers. To date, the IMT group has limited this research to flat wafers.

Finally, the group at the National Renewable Energy Laboratory (NREL) has also obtained very good results with a completely different deposition technique, the Hot-Wire CVD. In this technique, the absence of plasma has some advantages with respect to the other deposition methods as explained in the next section. The NREL group has demonstrated the possibility to obtain good quality layers and high efficiency heterojunction solar cells by HWCVD [Branz et al., 2007]. The best efficiency obtained until now is 18.5% on p-type textured substrates with a remarkable V_{oc} of 658 mV [Page et al., 2006].

1.5 Why the HWCVD technique for heterojunction solar cells?

Although the most common a-Si:H /μc-Si:H deposition technique is Plasma-Enhanced CVD, the Hot-Wire CVD technique has appeared as an interesting alternative in the last two decades. This technique was first used to deposit a-Si:H by Wiesmann in 1979 [Wiesmann et al., 1979] and later on by Matsumura who deposited the first microcrystalline layers [Matsumura, 1991]. Matsumura also introduced the term Catalytic CVD (Cat-CVD) to describe the catalytic nature of the reactions taking place at the wire surface. Nowadays, the two different terms coexist in the literature to describe the same deposition process. Hot-Wire CVD is now becoming a mature technique in the field of thin silicon film deposition.

It offers several features that overcome some limitations in the PECVD technique:

a) absence of ion bombardment and dust formation during deposition [Schropp, 2004]
b) high deposition rates, especially for μc-Si:H films [Nelson et al., 2001]
c) low equipment implementation and upkeep costs
d) high gas utilization (tens of %) [Honda et al., 2000]
e) easy scalability to large areas [Ishibashi, 2001]

Presently, the Hot-Wire CVD technique can be used to obtain devices with state-of-the-art properties: thin film solar cells [Schropp et al., 2007], thin-film-transistors (TFT) [Stannowski et al., 2003], microelectronic mechanical systems (MEMS) and, also, heterojunction solar cells [Branz et al., 2007]. Moreover, thanks to the simplicity of its geometry, large area HWCVD set-ups have been developed allowing homogeneous deposition over surfaces as large as 92 x 73 cm [Matsumura et al., 2003]. Since 2000, the HWCVD community meets in a biannual conference where the best results and advances are presented and discussed.

For all these reasons, and especially due to the possibility of sharing the HWCVD set-up and knowledge in thin silicon films of the Solar Energy Group at the Universitat de Barcelona, in this work we have investigated a-Si:H/c-Si heterojunction solar cells fabricated by HWCVD.

Chapter 2: Device fabrication process

> *"A goal without a plan is just a wish"*
> *Antoine de Saint-Exupery*

In this chapter, we briefly describe the process followed in this thesis to fabricate heterojunction silicon solar cells. In figure 2.1, a diagram of the fabrication process shows the sequential tasks to be done. Some of the lasts steps, especially the emitter and the rear side contact deposition, can be partially modified depending on the specific device structure. Most of the work is done in the Clean Room located at the DEE in the UPC, but the a-Si:H films are deposited by HWCVD at the *Departament de Física Aplicada i Òptica* in the *Universitat de Barcelona*.

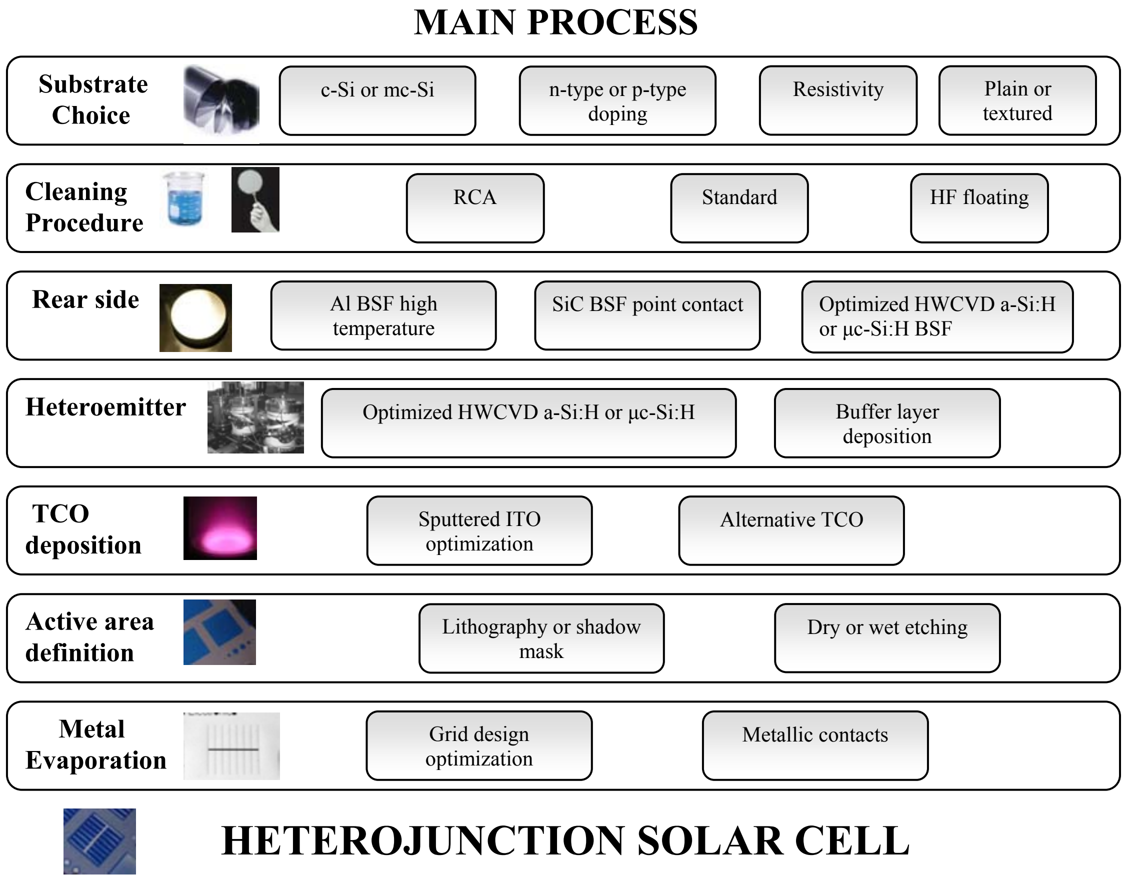

Figure 2.1: Diagram of the fabrication steps followed to obtain the complete solar cell.

2.1 Substrate Choice

All the heterojunction solar cells presented in this work have been fabricated on monocrystalline silicon wafers. The main aspects considered when choosing the material for this application were the silicon quality, the doping level and the thickness of the wafer. In the following section these aspects will be discussed in more detail.

a) *<u>What material?</u>*

Apart from thin-film technologies based on hydrogenated amorphous silicon (a-Si:H) and microcrystalline silicon (μc-Si:H), commercial crystalline silicon solar cells are fabricated on monocrystalline and multicrystalline silicon wafers.

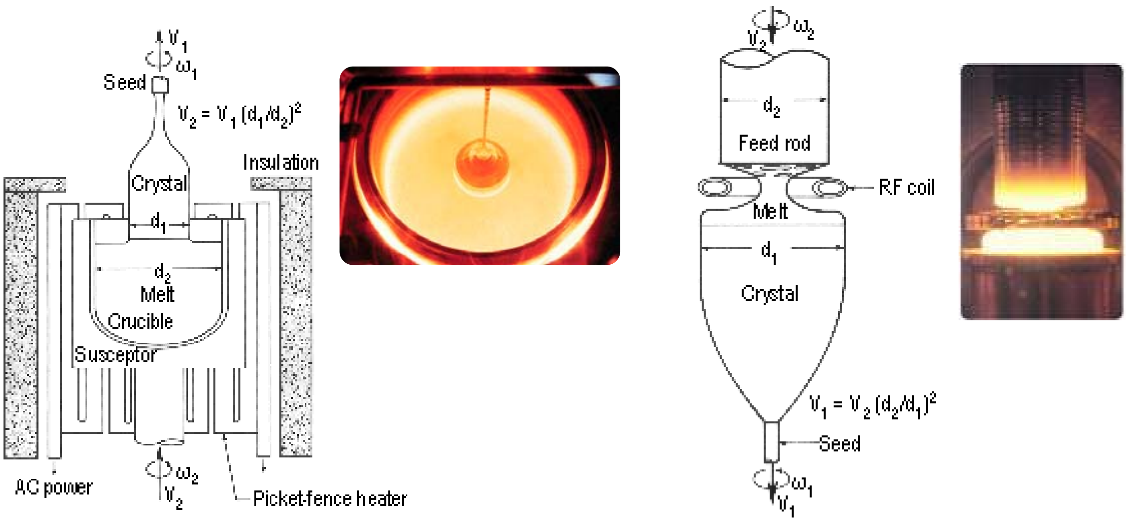

Figure 2.2: CZ and FZ processes for the production of monocrystalline silicon ingots.

Different processes can be used to obtain monocrystalline silicon wafers. The most established ones are the Czochralski (CZ) and Float-Zone (FZ) techniques. In the CZ process a crystal seed dipped into a crucible of molten silicon is removed slowly, pulling a cylindrical ingot as silicon crystallizes on the seed. In the FZ process a silicon rod is set on top of the crystal seed, while RF electromagnetic coils heat and melt the interface between the rod and the seed. Monocrystalline silicon forms at the interface, growing up as the coils are slowly raised. The FZ technique produces purer crystals than the CZ method, because they are not contaminated by the crucible used for growing CZ crystals. Once the ingots have been produced, either by the CZ or FZ methods, they must be sliced to form thin wafers. Such sawing wastes as much as 20% as sawdust, known as kerf.

Multicrystalline silicon has appeared as an alternative included in the so called *solar-grade* silicon (introduced in 1.3). The demonstration of 19.8% efficiency for a small area multicrystalline silicon cell suggests the potential lying in this lower cost substrate [Zhao et al., 1998]. The most usual method to produce multicrystalline silicon involves a casting process of molten silicon into a mould. The starting material can be lower-grade silicon, rather than the higher-grade material required for monocrystalline silicon. The cooling rate is the main factor determining the final crystal size in the ingot and the distribution of impurities. The mould is usually square, producing an ingot that can be sliced into square cells that fit compactly into a PV module.

Another group of processes to obtain crystalline silicon are known by the general name of ribbon growth. These methods can directly produce multicrystalline silicon wafers, thus avoiding the slicing step required for cylindrical ingots. The most developed ribbon growth technique is the Edge-defined Film-fed Growth (EFG) [Wald et al., 1981], which is already in high volume commercial production [Schmidt et al., 2002].

In this thesis, we have centralised our efforts in optimizing solar cells on monocrystalline silicon because of the novelty of the investigation in heterojunction devices fabricated by HWCVD. Both CZ and FZ c-Si wafers have been used depending on the specific experiment in course. Detailed passivation studies and optimization of heterojunctions were preferably performed on FZ substrates (ρ = 1-10 Ωcm) in order to assure very low bulk recombination. Thereby, the measured effective lifetime is mainly determined by the interface between a-Si:H and c-Si [Martin, 2004]. Complete solar cells were manufactured on both FZ and CZ substrates.

b) Which doping?

Traditionally, industrial solar cells have been fabricated onto p-type wafers for a few reasons [Goetzberger et al., 2003]. The most important one was the simplicity to obtain this material as surplus from the electronic industry (section 1.2). Recently, the possibility of using n-type wafers has appeared as a feasible alternative due to the shortage of crystalline silicon.

In the case of heterojunction solar cells, the record efficiency reported by Sanyo was actually obtained using n-type wafers [Taguchi et al., 2005]. In agreement, Wang et al. have proposed a series of advantages when using n-type wafers in heterojunction solar cells [Wang et al., 2004]. Figure 2.3 shows the band diagram of bifacial heterojunction devices based on both n-type (a) and p-type (b) c-Si substrates. It is important to remark the accepted larger a-Si:H/c-Si band offset in the valence band (E_v) than in the conduction band (E_c) [Stangl et al., 2001]. This effect reflects, for instance, the small difference between the electron affinities of a-Si:H (3.9 eV) and c-Si (4.05 eV).

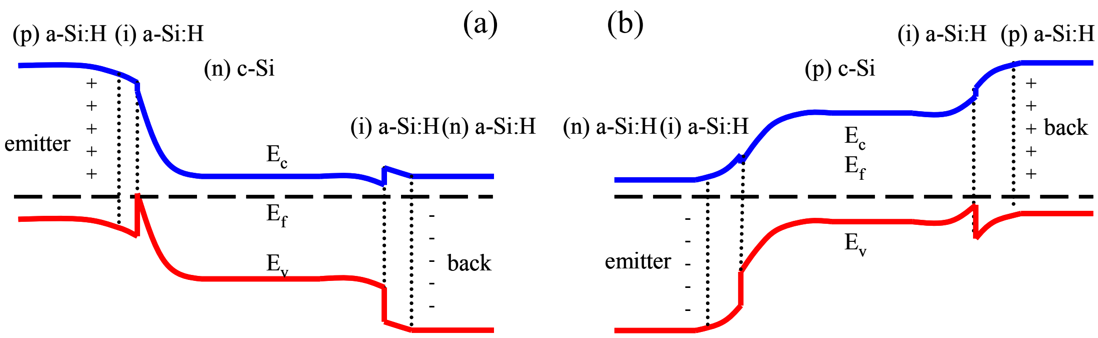

Figure 2.3: band diagram of n-type (a) and p-type (b) bifacial heterojunction devices [Wang et al., 2004].

In the case of using n-type wafers (a), the large valence band offset at the front junction results in a potential well in which minority carrier holes could be trapped, preventing efficient photo-generated carrier transport. However, the trapped holes may be able to tunnel across the thin (i)a-Si:H layer into the (p)a-Si:H emitter. On the backside, the large valence band offset provides a back surface "mirror" for holes. The offset at the conduction band is small enough to allow efficient electron collection at the back contact. Thus the (i/n)a-Si:H stack provides an excellent back contact with adequate majority carrier electron transport and excellent passivation repelling minority carrier holes from the back contact.

By contrast, on p-type c-Si wafers (b), minority carrier electron collection at the front junction will be impeded by only a little barrier created by the small band offset in the conduction band edges. Thus, minority carrier collection should be even easier than in the n-type c-Si based solar cells. However, lower open-circuit voltages are expected since the built-in voltage at the front junction is comparable to a homojunction, much less than on n-type c-Si wafers. On the backside, the small conduction band offset provides a much less effective mirror for the minority carrier electrons. Worse, the large offset in the valence band edges results in an important barrier for majority carrier holes to be collected at the back contact. Though thinner or i-layer suppression can favour tunnelling transport, the passivation quality would be partially reduced in such case.

Summarizing:

(1) optimized (n/i)a-Si:H stacks can form good emitters on p-type c-Si, but with built-in voltages comparable to homojunction devices

(2) optimized (p/i)a-Si:H stacks can form great emitters on n-type c-Si, with built-in voltages significantly higher than in homojunction devices
(3) optimized (i/p)a-Si:H stacks can form fair back contacts on p-type c-Si based solar cells
(4) optimized (i/n)a-Si:H stacks can form excellent back contacts on n-type c-Si based solar cells

According to these reasons, we can affirm that higher efficiencies could be obtained on n-type wafers. In the same sense, figure 2.4 shows a study by Jensen et al. about the influence of front surface recombination velocity (S_{it}) in the open-circuit voltage (V_{oc}) of heterojunction solar cells. The quality of the c-Si substrate is considered in the effective diffusion length (L_{eff}). It is important to remark the strong influence of surface recombination in the case of high quality ($L_{eff} > 100$ µm) p-type c-Si substrates (solid line). Then, V_{oc} values over 600 mV are difficult to reach without relatively good surface passivation ($S_{it} < 10^3$ cm/s). By contrast, surface recombination is not so critical on n-type c-Si substrates (dashed line). Moreover, Taguchi et al. have demonstrated that devices based on n-type substrates do not suffer lifetime degradation related to boron metaestable states [Taguchi et al., 2000].

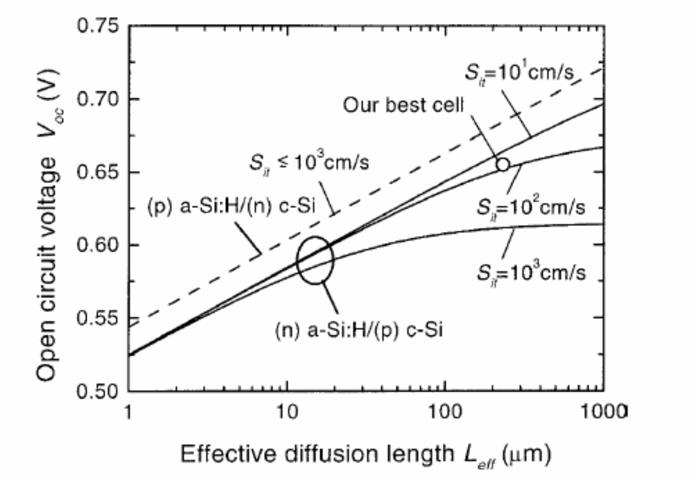

Figure 2.4: dependence of the Voc with the diffusion length for p- and n-type wafers with different surface recombination velocities [Jensen et al., 2003]

In spite of everything, most groups still work with p-type wafers due to basically technological problems [Jensen et al., 2003]. For instance, good quality p-doped a-Si:H emitters are much more difficult to obtain than n-doped ones. Besides, aluminium back-surface-field (Al-BSF) contacts can not be used in the case of n-type c-Si wafers. Due to these technological reasons the scientific community has not totally solved the debate about the best doping type for heterojunction silicon solar cells.

c) What thickness?

Traditionally, wafers over 300 microns thick have been used to fabricate crystalline silicon solar cells. This thickness gives the required mechanical strength for handling and the resistance to the stress due to different contraction of layers on front and rear surfaces during fabrication. However, just the substrates represent currently close to 40% of the final module cost, which has to be reduced to be competitive with other energy sources [Quang et al., 2004]. For example, the use of 150 μm thick wafers would increase the production around 30% with a simultaneous cost reduction of 14% [Quang et al., 2004]. Swanson announces wafer thicknesses close to 120 μm for c-Si and 180 μm for mc-Si in industrial production by 2012 [Swanson et al., 2004]. A clear example of the present effort to save c-Si is a recently developed structure denominated SLIVER [Stocks et al., 2003] that proposes the cross section of 1 mm thick c-Si wafers in strips of thickness inferior to 100 μm. This new structure achieves 17.5% efficiency with a saving of material superior to a factor 12 with respect to conventional technologies.

Concerning the standard process of silicon growth and wafer sawing, it is already relatively simple to obtain wafers around 200 μm with much reduced kerf losses. In addition, new sawing techniques have been developed in the last decade (multi-wire sawing), that allow wafer thicknesses below 100 μm [Funke et al., 2004]. In order to maintain a high cell performance as the substrate thickness is reduced, much attention must be paid to the passivation at both surfaces of the cell (reduce interface defect density). Back surface recombination can remarkably affect the final device efficiency when the wafer thickness becomes comparable to the carrier diffusion length [Aberle, 2000]. Figure 2.5 shows the solar cell efficiency as a function of the wafer thickness for different back surface recombination velocities (S_{0back}). Two main situations have been considered: a long diffusion length (L_n = 1000 μm) corresponding to good quality c-Si wafers and a short one (L_n = 200 μm) for lower quality substrates.

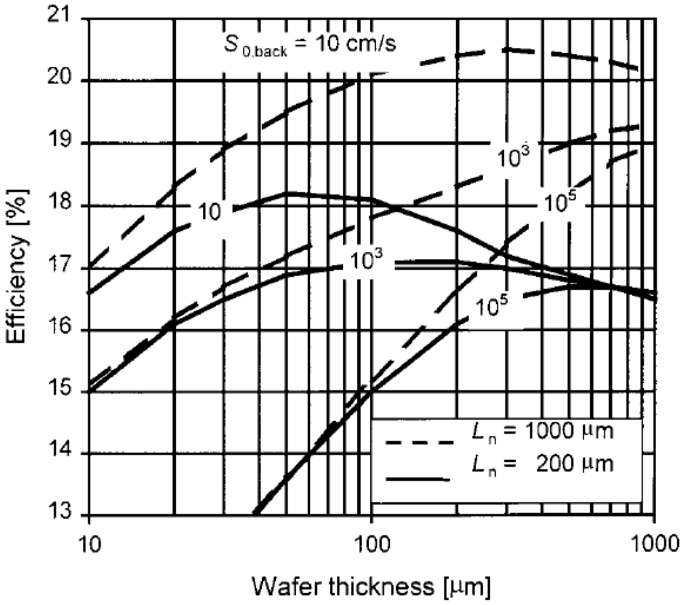

Figure 2.5: Relation between the wafer thickness and the efficiency of a solar cell for different diffusion lengths (L_n) and surface recombination velocities (S_{0back}). A good surface passivation ($S_{0back} <$ 100 cm/s) is essential for thinner wafers (< 200 µm) [Aberle, 2000].

Solar cells fabricated on low quality c-Si substrates (solid line) can exceed 18% efficiency if the wafer thickness is reduced below 100 µm, but excellent surface passivation (S_{0back} = 10 cm/s) is necessary. By contrast, poor surface passivation (S_{0back} > 10^3 cm/s) drastically reduces the final device efficiency when using thin wafers, while there is no significant influence for thicker ones. On the other hand, considering good quality wafers (dashed line); a good surface passivation increases the solar cell efficiency over 20%, though this effect is less important for thick substrates. It is very important to note that the difference between good and low quality c-Si substrates diminishes when the wafers are thinned.

As a consequence, besides an efficient wafer sawing technique, the goal is a method to easily passivate c-Si thin wafers. Optimized aluminium back-surface-field (Al-BSF) contacts can not reduce the S_{0back} value much below 10^3 cm/s [Jeong et al., 2001]. Besides, the relatively high temperatures required for Al diffusion (800ºC) are not compatible with thin substrates due to wafer bowing during the cooling process. Although silicon dioxide very effectively passivates the c-Si surface [Zhao et al., 1999], the temperatures involved in the process are even higher (~ 1000ºC) than in the Al-BSF contact. Moreover, low cost silicon wafers are not compatible either with high temperature steps due to strong lifetime degradation [Schultz et al., 2004]. Therefore, low temperature surface passivation schemes based on thin films of hydrogenated amorphous silicon (a-Si:H) [Kunst et al., 2002], [Voz et al., 2003], silicon nitride (a-SiN_x:H) [Lauinger et al., 1996], [Leguijt et al., 1996] and silicon carbide (a-SiC_x:H) [Martin et al., 2001] have gained special interest due to their compatibility with both thin and low quality c-Si substrates. A detailed discussion on these approaches can be found in section 2.3.

2.2 Cleaning procedures

Before depositing any layer on the c-Si surface, it must be cleaned from organic and inorganic impurities in order to obtain high performance devices. The cleaning procedure is also essential to prevent contamination of the process equipment and assure reliable results.

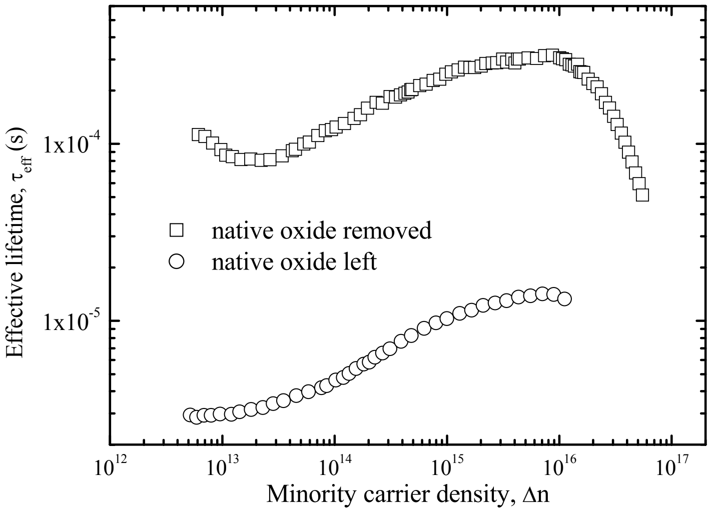

Figure 2.6 Effective lifetime vs minority carrier density curves measured by QSSPC for the same emitter deposited either on the native oxide (○) or in a sample where it has been totally removed (□).

The passivation quality strongly depends on the cleaning procedure followed before the layer deposition. Moreover, the native oxide grown onto the silicon surface must be totally removed to leave a clean interface. Figure 2.6 compares the effective lifetime measured by QSSPC for emitters deposited on silicon wafers where the native oxide has been either removed or not. The passivation quality degrades due to interface recombination when the native oxide is left on the c-Si surface. Next, we briefly describe the cleaning procedures used in this work to clean the substrates.

a) RCA cleaning

The RCA cleaning is the industrial standard process for removing contaminants from the c-Si surface. Werner Kern developed the basic procedure in 1965 while he was working for Radio Corporation of America, hence the RCA name. The RCA cleaning procedure consists of three main sequential steps:

I. **Organic Cleaning:** Removal of insoluble organic contaminants with a H_2O:H_2O_2:NH_4OH (5:1:1) solution.
II. **Oxide Strip**: Removal of thin silicon dioxide layer as a result of (I) where metallic contaminants may accumulate, using a diluted H_2O:HF (50:1) solution.
III. **Ionic Cleaning**: Removal of ionic and heavy metallic contaminants using a H_2O:H_2O_2: HCl (6:1:1) solution.

The RCA cleaning does not etch silicon, only a very thin silicon dioxide layer is removed during step II. The procedure was also designed to prevent reincorporation of metallic contaminants from solution back to the c-Si surface. When the RCA cleaning is finished, the polished side of the wafer should look specular with no residue.

b) Standard cleaning

A simpler procedure to prepare the c-Si surface is generally known as standard cleaning. The standard cleaning procedure consists of two main steps:

I. **Organic coating removal**: The wafers are immersed into a H_2SO_4:H_2O_2 (2:1) solution, generally called *piranha*. Organic residues are removed while metallic contaminants form soluble complexes. The mixture is self-heating and solution looses its effectiveness when it cools down after about 10 minutes.
II. **Oxide removal**: The thin silicon dioxide layer grown during I is removed by dipping the wafer in a H_2O:HF (50:1) solution until the surface becomes hydrophobic.

The standard cleaning is usually adequate for wafers that have been accurately handled before being processed. When that is not the case, at least one complete RCA cleaning is required to assure good and reproducible results.

2.3 Rear side fabrication

The rear side of the solar cell should accomplish three main conditions:

- Good surface passivation to reduce recombination losses
- Good internal reflection to profit irradiance at longer wavelengths
- Good electrical contact to reduce the series resistance of the device

2.3.1 High temperature BSF

The simplest solution used in the photovoltaic industry for the rear side is an Aluminium Back-Surface-Field contact (Al-BSF). The standard process consists in the deposition of an aluminium screen-printing paste (~ 20 μm) by serigraphy and a post annealing reaching temperatures up to 800ºC [Veschetti, 2005]. The final structure is a three layer system: a heavily Al-doped (1%) silicon layer, an AlSi compact alloy and a phase-mixed AlSi/Al_2O_3 layer [Huster, 2005]. The main problem of Al-BSF contacts is wafer bowing during the cooling process, which is especially important in thinner substrates (< 200 μm). Although some solutions to reduce this wafer bowing have partially succeeded [Huster, 2005], the elimination of high temperature steps is definitely attractive. On the other hand, back surface recombination velocity with optimized Al-BSF contacts can not be reduced much below 10^3 cm/s [Jeong et al., 2001], whereas internal reflection is usually below 70% [Hermle et al., 2005].

2.3.2 Low temperature passivation

Here, we consider low temperature back surface passivation alternatives to Al-BSF contacts. These structures are based on dielectric films which can provide much lower surface recombination velocities ($S_{back} < 10^2$ cm/s), but require a point contact patterning of the backside as proposed with the PERC (Passivated Emitter and Rear Cell) concept

[Green et al., 1990]. The internal reflection of these structures generally exceeds 90%, which is important to profit long wavelength irradiance in thin substrates [Hermle et al., 2005]. Although point contact formation based on photolithography is unlikely to succeed in industrial production, the recently developed laser fired contact (LFC) technology has really great potential for future applications [Schneidorlöchner et al., 2002]. However, the laser set-up and the beam positioning system introduce a relatively complex additional process.

a) Silicon Nitride

Hydrogenated amorphous silicon nitride (a-SiN_x:H) deposited by Plasma-Enhanced Chemical Vapour Deposition (PECVD) is one of the most developed low temperature (< 500ºC) passivation alternatives. Effective surface recombination velocity values of just 4 and 20 cm/s have been reported on p-type (1 Ωcm) [Lauinger et al., 1995] [Mäckel et al., 2002] [Schmidt et al., 2001] and n-type c-Si (18 Ωcm) [Kunst et al., 2002b], respectively. The excellent passivating properties of a-SiN_x:H films have been attributed to two main effects: reduction of the interface state density and field-effect passivation by the positive fixed-charge in the film [Schmidt et al., 1999]. Besides, the high hydrogen content of a-SiN_x:H films deposited at low temperature can also passivate defects in the bulk of mc-Si substrates during post-annealing [Duerinckx et al., 2002].

On the other hand, a-SiN_x:H films can be also used as antireflection coatings on the front side of solar cells. The refractive index can be tuned to the desired value (~ 1.9) by varying the nitrogen content and the films are very stable under ultraviolet radiation.

b) Silicon Carbide

Recently, excellent passivation properties have been obtained with hydrogenated amorphous silicon carbide (a-SiC_x:H) films deposited by PECVD. In particular, S_{eff} values below 30 and 11 cm/s have been reported on p-type c-Si (3.3 Ωcm) with intrinsic and phosphorous doped layers, respectively [Martin et al., 2005]. In the case of n-type substrates (1.4 Ωcm) $S_{eff} < 54$ cm/s has been obtained with intrinsic a-SiC_x:H films [Martin et al., 2002], which can be reduced to $S_{eff} < 16$ cm/s by adding a small nitrogen content to the deposited a-SiC_xN_y:H film. As in the previous case, two mechanisms contribute to the passivation with a-SiC_x:H films: reduction of interface state density related to dangling-bonds, and field-effect passivation due to the fixed-charge density in the film unbalancing the carrier densities near the interface [Ferre et al., 2005]. Passivation at the rear side of c-Si solar cells with a-SiC_x:H films has already demonstrated conversion efficiencies over 20% [Glunz et al., 2005].

c) Hydrogenated Amorphous Silicon

Hydrogenated amorphous silicon (a-Si:H) is widely used in the PV industry to manufacture thin film solar cells due to its high optical absorption coefficient and acceptable semiconducting properties [Street, 1991]. In the last decade, the excellent passivating properties of a-Si:H films on c-Si substrates have been demonstrated in several works. In this case the passivation mechanism is mainly based on the reduction of the defect density at the interface [Dauwe et al., 2002], since the fixed-charge density in high quality intrinsic a-Si:H films is very low.

Intrinsic a-Si:H films deposited by PECVD allowed S_{eff} values of 68 cm/s on p-type (1 Ωcm) c-Si [Van Cleef et al., 1998], whereas films deposited by the Hot-Wire Chemical Vapour Deposition (HWCVD) technique resulted in 60 cm/s on p-type c-Si (3.3 Ωcm) and 130 cm/s on n-type c-Si (1.4 Ωcm) substrates [Voz et al., 2003]. In the structure COSIMA (aluminium contacts to an a-Si:H passivated wafer by means of annealing) [Plagwitz et al., 2004], p-type (1.4 Ωcm) wafers passivated with intrinsic a-Si:H films (50 nm) are contacted by annealing aluminium lines at 210ºC for 3 hours. Thereby, contact resistances as low as 0.015 $\Omega\cdot cm^2$ can be obtained maintaining satisfactory S_{eff} values of 124 cm/s with a 6% contacted area.

Furthermore, heavily doped a-Si:H layers can be used as low temperature deposited BSF contacts. In combination with heterojunction emitters, this approach leads to an entirely low temperature fabrication process. Undoubtedly, the most successful result is the Heterojunction with Intrinsic Thin Layer (HIT) solar cell developed by Sanyo Electric Co. with record 19.5% conversion efficiency in mass-produced modules [Tanaka et al., 2003]. Such an excellent result has moved many groups worldwide to fabricate double-side heterojunction solar cells using different deposition techniques.

The best results reported to date have been summarized in the previous chapter (Table 1.2).

2.4 The Hot-Wire Chemical Vapour Deposition technique

There are several methods to deposit a-Si:H films [Street, 1991], but in this work we have used the HWCVD technique for both the emitter and low temperature deposited BSF contact. The set-up is located at the *Departament de Física Aplicada i Òptica* of the *Universitat de Barcelona*. A more extensive and accurate description of this system can be found in [Peiró, 1999].

2.4.1 Hot-Wire Chemical Vapour Deposition

In the HWCVD technique, silicon deposition takes place upon catalytic decomposition of reactant gases at the surface of a wire heated to temperatures in the range of 1500-2000ºC. The wire is usually a filament of Tungsten (W) or Tantalum (Ta). The common gases used for growing silicon thin films are silane (SiH_4) and hydrogen (H_2). These gas molecules are dissociated at the hot filament surface by a catalytic process after which mostly hydrogen (H) and silicon (Si) atoms are released. The processes taking place at the filament surface have been analysed to identify the nature of the resulting species [Doyle et al., 1988]. A schematic representation of the HWCVD process is shown in Figure 2.7. Some of the silicon and hydrogen atoms released from the filament can reach the substrate without any collision, whereas some other undergo secondary reactions as they diffuse from the filament to the substrate. The properties of the deposited films can be strongly affected by the products of these reactions, which may occur with other radicals generated at the filament surface or with SiH_4 and H_2 molecules inside the chamber. Therefore, the quality of the films depends on the deposition parameters: on the one hand, the substrate temperature (T_s) related to the surface mobility of radicals, and on the other hand, those parameters influencing the nature of the radicals, that is pressure (P), filament temperature (T_f) and hydrogen-silane mixture. Moreover, geometrical issues such as the filament-substrate distance ($d_{f\text{-}s}$) or filament configuration (quantity, area and shape) play also a role on gas-phase and deposition chemistry [Soler, 2004].

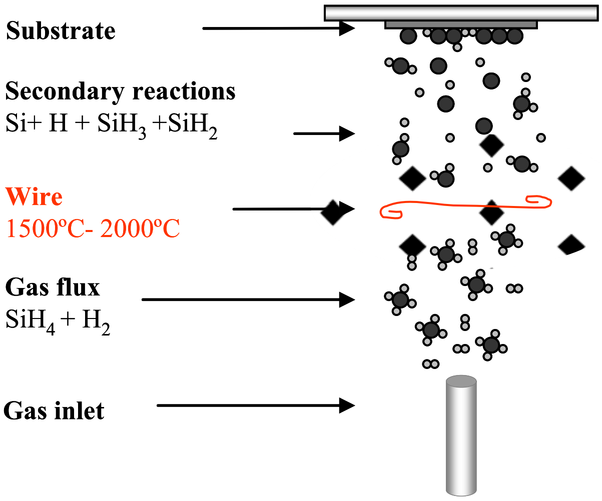

Figure 2.7: Schematic representation of the processes involved in the HWCVD technique.

2.4.2 The Universitat de Barcelona HWCVD set-up

The HWCVD set-up placed at the *Universitat de Barcelona* consists of three ultra-high vacuum chambers isolated by gate valves, as it is shown in figure 2.7. A magnetic transfer system is used to place the substrate in the desired chamber. The first chamber is devoted to deposit only undoped a-Si:H films using silane and hydrogen as precursor gases. Therefore, the intrinsic character of the layer is insured avoiding cross contamination. Unintentional doping can be specially detrimental when dealing with μc-Si:H films [Voz et al., 2000], [Song et al., 2000]. The second chamber is intended for depositing doped layers. Diborane (B_2H_6) and phosphine (PH_3) gases are the doping precursors added to silane and hydrogen to obtain p- and n-doped layers, respectively. Finally, the third one is a load-lock chamber to minimize the presence of air in the HWCVD process chambers. This last chamber also includes an RF magnetron sputtering cathode to deposit transparent conductive oxides. The inline configuration allows the deposition of several layers without exposing the samples to the atmosphere. This possibility is interesting for heterojunction structures based on stacks of an intrinsic buffer followed by a doped layer. The pumping system consists of a turbomolecular pump followed by a roots blower pump and a rotary vane pump, which allow a base pressure below 10^{-8} mbar in the HWCVD chambers.

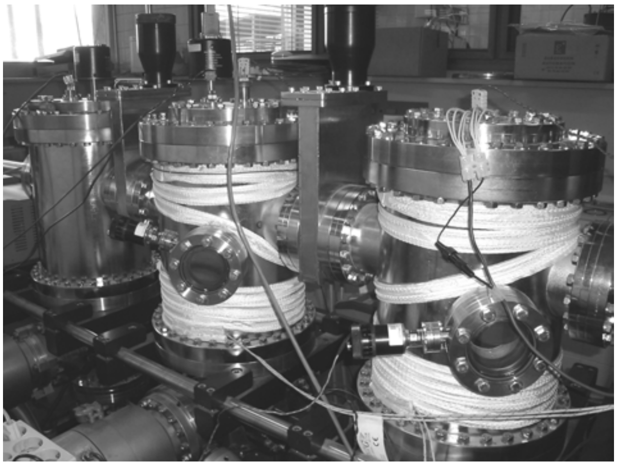

Figure 2.8: Picture of the multichamber HWCVD set-up. The system was ensembled by the Scientific-Technical Services of Universitat de Barcelona.

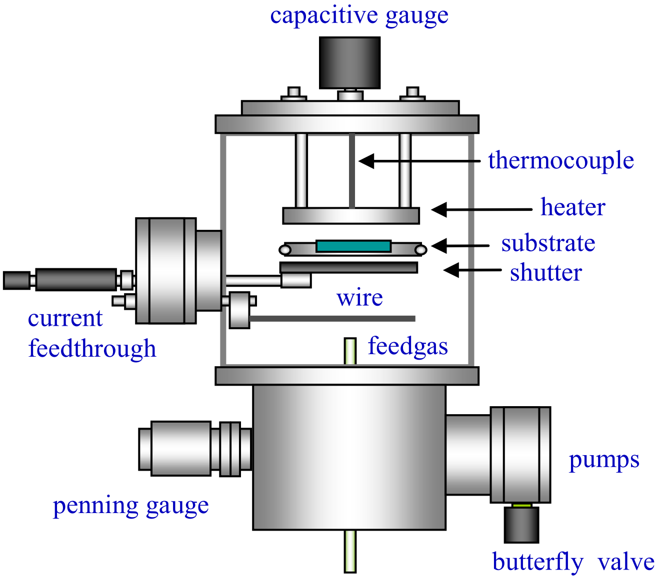

Figure 2.9: Internal arrangement of the different components inside the HWCVD chamber.

Figure 2.9 shows a schematic of the configuration inside one of the HWCVD process chambers (both are similar). Butterfly valves are used to control the process pressure during thin film deposition. Finally, the substrate temperature is controlled with a resistive heater, which in the chamber for intrinsic material is external to minimize unwanted contamination [Fonrodona, 2003]. It is important to remark that the actual substrate temperature T_S is significantly affected by the wire irradiation, but a previous calibration has taken into account this influence [Soler, 2004].

2.4.3 About the wire

In this work, we have mainly used tantalum (Ta) wires with temperatures ranging from 1500 to 1900ºC. Tantalum is a especially suitable catalytic material for low filament temperatures (T_f) because the formation of silicides on its surface is lower than on tungsten (W) filaments [Van Veenendaal et al., 2001]. The undesired formation of silicides increases the filament fragility and its probability of breakage, especially at the cold ends of the filament [Mahan 2003], [Ishibashi 2001]. Therefore, Ta filaments are a good alternative to W ones considering their longer lifetime and the better reproducibility of the process [Van Veen, 2003]. In particular, two different wire configurations have been considered in this work (Table 2.1).

	wire (material)	∅ (mm)	distance between wires (cm)	distance to target (cm)	distance to gas inlet (cm)
Configuration 1	1 (Ta)	1	X	4	1
Configuration 2	2 (Ta)	0.5	3	4	1

Table 2.1: Parameters of the two different wire configurations used in this work.

The first configuration with one Ta wire of diameter 1mm was the usual configuration in the HWCVD set-up at *Universitat de Barcelona*. The second configuration with two Ta wires was implemented during this thesis to enlarge the homogeneous deposition area to 4×4 cm^2. In this case, two parallel tantalum wires separated 3 cm each other are centred 1 cm above the gas inlet. The diameter of the wires is 0.5 mm and the distance to the substrate is 4 cm, as in the single wire configuration.

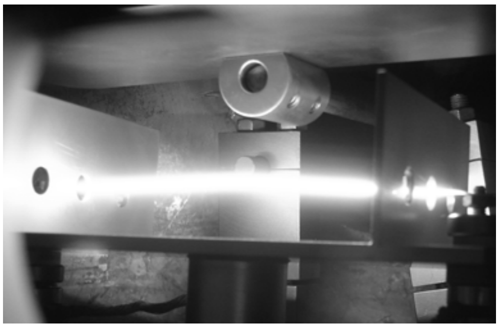

Figure 2.10: Tantalum wire during a HWCVD process.

An example of the thickness homogeneity achieved with the double wire configuration is shown in figure 2.11. As it can be observed, the variation in the thickness of the deposited film is less than 12% within a square area of 16 cm^2 [Villar, 2008].

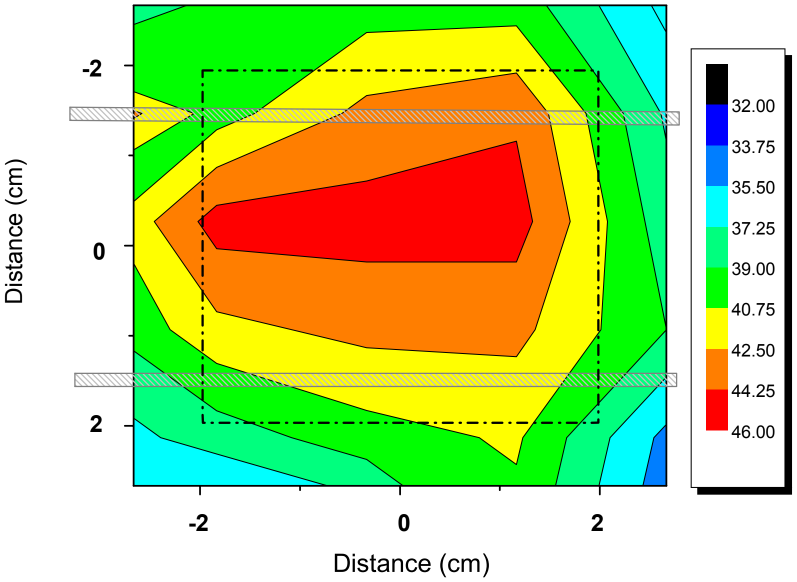

Figure 2.11: Thickness variation for an a-Si:H film deposited by HWCVD with the double wire configuration. The dotted lines indicate the inhomogeneity of a 2x2 cm^2 square area.

2.5 Fabrication of the front electrode

Once the heterojunction emitter has been deposited by HWCVD, the front electrode has to be fabricated fulfilling some requirements:

- High electrical conductivity to reduce the series resistance of the solar cell
- Highly transparent, that is, light absorption and reflection as low as possible
- Low damage to the underlying heterojunction emitter

In heterojunction solar cells, the front electrode usually consists of a transparent conductive oxide (TCO) layer and a metallic grid. The process to fabricate the front electrode is briefly described in this section.

2.5.1 TCO Deposition

The selected TCO requires a high electrical conductivity, since it must collect the carriers towards the metallic contact. Besides, it must be highly transparent to let most light enter the solar cell. In this sense not only a low optical absorption matters, but also the antireflection effect that can be obtained by tuning the film thickness. In this work, we have focused on optimizing Indium Tin Oxide (ITO) layers deposited by RF magnetron sputtering. In this deposition technique atoms in a solid target material are ejected into the gas phase due to the bombardment by energetic ions. It is performed by applying a high voltage at a frequency of 13.56 MHz across a low-pressure gas (usually argon) to create the plasma, which consists of electrons and gas ions in a high-energy state. The term magnetron indicates that the sputtering cathode includes a circular magnet that creates a magnetic field parallel to the target. This design allows higher deposition rates [Ohring, 1992]. In the set-up at UPC the vacuum chamber is connected to the pumping system formed by a turbomolecular pump followed by a rotatory pump. The 4 inches target is placed under the sample holder to avoid eventual dust deposition during the process. The distance between the target and the substrate is 3 cm, which leads to good uniformity for the desired sample size of diameter 5 cm. The sample holder incorporates a resistive heater that allows substrate temperatures up to 300ºC.

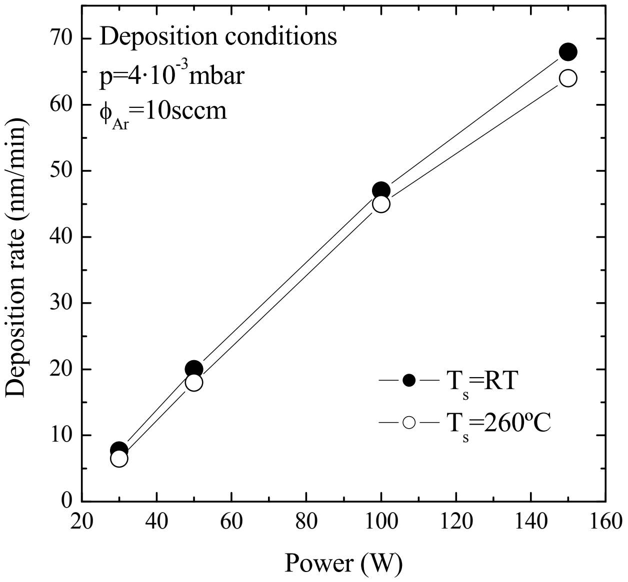

Figure 2.12: Deposition rate vs. RF power for layers deposited at room temperature (RT) and at 260ºC.

The ITO layers must be optimized in terms of transparency and conductivity. The influence of the main deposition parameters has been studied: RF power, substrate temperature, process pressure, and oxygen and argon flow. Especially remarkable is the dependence of the deposition rate on the RF power. This curve is shown in figure 2.12 for samples deposited at room temperature (RT) and at 260ºC, over the ITO crystallisation temperature (~ 250ºC). The influence of other parameters on the deposition rate has been widely described in the literature [Maissell et al., 1970].

In the case of heterojunction solar cells, changes induced by the ITO deposition process on the previously deposited a-Si:H layers are also relevant [Christensen et al., 2006]. Then, the optimization process should consider not only the properties of the ITO layer, but also of the complete heterojunction emitter.

The work function (WF) of the ITO layer is a particularly important parameter to take into account. The WF value changes with the oxygen concentration and the deposition temperature [Ulyashin et al., 2002]. Besides deposition conditions, post-treatments like ozone atmosphere cleaning (UVO) and post-annealing of the samples can shift the work function from around 4.2 eV up to 5.4 eV [Sugiyama et al., 2000], [Minami, 1999]. Since the a-Si:H layers are very thin, the ITO layer modifies the built in potential of the device. Lower WF values for (n)a-Si:H [Stangl et al., 2003] and higher ones for (p)a-Si:H are desired to obtain higher open circuit voltages in the device. For instance, a too low WF value of the ITO layer on (p)a-Si:H induces the formation of an inverted Schottky junction that can reduce or even cancel out the device performance [Centurioni et al., 2003].

2.5.2 Active Area Definition

The active area of the solar cell can be defined either by a lithographic process or, more simply, by using a shadow mask during the deposition of the ITO layer. In any case, the surrounding highly doped a-Si:H layer must be etched to isolate the device. Otherwise, leakage currents reduce the parallel resistance (R_p) of the solar cell leading to degraded fill factor and open-circuit voltage values [Puigdollers, 1995]. In this thesis two different etching procedures have been investigated:

a) Wet-etching based on tetramethylammonium hydroxide (TMAH)

b) Dry-etching based on a RF plasma of carbon tetrafluoride (CF_4)

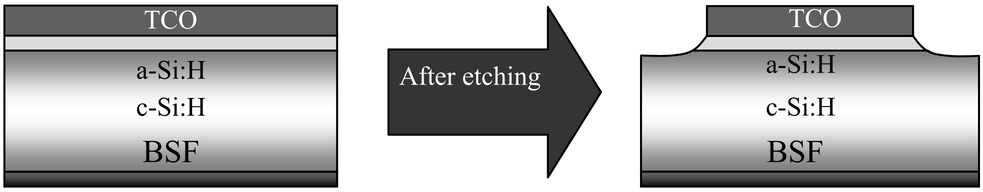

Figure 2.13: Device active area definition and etching of the doped a-Si:H emitter to avoid lateral leakage currents.

2.5.3. Evaporation of the metallic contacts

The final step to complete the fabrication of the solar cell is the deposition of the metallic front contact. This electrode consists in a metallic grid deposited by electron beam evaporation using a shadow mask positioned on the active area of the device. The thickness and deposition rate of the metallic grid is accurately monitored by means of a quartz crystal oscillator [Orhing, 1992]. The grid pattern must be designed to reduce the shadowed area maintaining a low series resistance in the device [Burgers, 1999], [Altermatt, 1998]. In fact, the thickness and doping level of the emitter together with the sheet resistance of the TCO layer also change the optimum grid design [Cuevas, 2002]. In figure 2.14 there is a picture of one of the shadow masks used to evaporate the grid contact and an example of two different patterns used in 1 cm^2 solar cells.

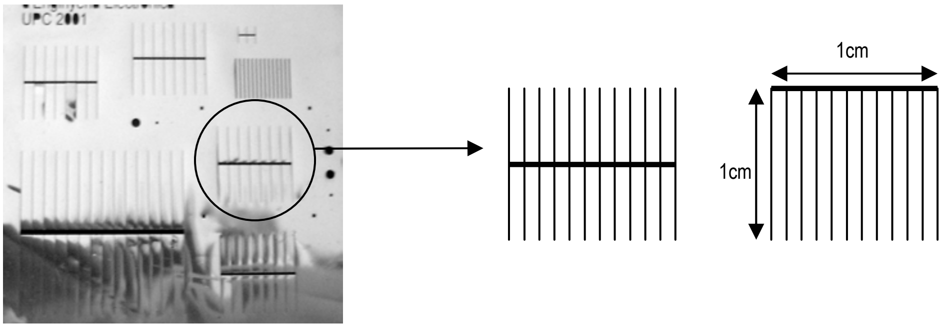

Figure 2.14: picture of one of the metallic masks used to evaporate the grid contact and example of two different patterns for 1 cm^2 solar cells.

In the case of using a low temperature deposited (p^+)a-Si:H layer to replace traditional Al-BSF contacts, also a continuous metallic layer must be deposited at the back side. In this case a TCO layer is also usually intercalated between the (p^+)a-Si:H layer and the back metallic electrode to reduce the contact resistance and improve the internal back reflection. In this work different metals have been evaporated in order to evaluate the contact resistance and adherence with the TCO layer. In the case of ITO, silver seemed to be the best option.

Chapter 3: Characterization tools

"Demuestra lo que dices y dí lo que demuestras"
(Anónimo)

3.1 Material Characterization tools

In the following sections we summarize the structural and compositional characterisation tools used in this work to determine the properties of a-Si:H layers. The electrical and optical characterizations are also considered for films and complete devices. Here we will briefly describe the experimental set-up, whereas more details on the results are presented in next chapters.

3.1.1 Structural and compositional characterization

The first measurement carried out for each deposited layer is the measurement of its thickness by means of a Dektak 3030 stylus profilometer. Then, the growth rate (r_d) can be evaluated considering the deposition time.

a) Raman spectroscopy

Raman spectroscopy is used to evaluate the crystalline fraction (X_c') of the samples. The spectrometer was a Jobin-Yvon T64000 with a laser beam at a wavelength of 514 cm^{-1}. The characteristic peak corresponding to the transverse optical (TO) mode of crystalline silicon can be found at 520 cm^{-1}, whereas the amorphous band appears around 480 cm^{-1}. The X_c' can be determined by deconvoluting the amorphous and microcrystalline contributions using the formula [Tsu et al., 1982]:

$$X'_c = \frac{I_c}{I_c + \sigma I_a} \tag{3.1}$$

where I_c corresponds to the microcrystalline and I_a to the amorphous intensity contributions. The parameter σ is the cross section ratio for the Raman effect in a-Si:H and μc-Si:H and strongly depends on the crystallite size [Bustarret et al., 1988]. Different groups [Han et al., 2003], [Van Veen, 2003] consider additional peaks centred between 500 and 510 cm^{-1}, mainly attributed to small grain and boundaries effects.

In our case, instead of using the crystalline fraction, we use the crystalline ratio or integrated crystalline fraction X_c defined as:

$$X_c = \frac{I_{520}}{I_{520} + I_{480}} \tag{3.2}$$

where I_{520} and I_{480} are the intensities of the peaks located at 520 cm^{-1} and 480 cm^{-1}, respectively. This simplified parameter is commonly used as an estimation of the real crystallinity. In order to facilitate comprehension, in next chapters we will refer to X_c as crystalline fraction.

b) Fourier Transform Infrared (FTIR) Spectroscopy

Fourier Transform Infra-Red Transmittance of silicon thin layers was measured by means of a Nicolet 5ZDX FTIR spectrometer. This measurement gives us information related to the concentration of bonded hydrogen atoms and their bonding configuration in the layer. The infrared wavelength is absorbed in a resonant way by the vibration modes of the molecules in the layer. The frequency of this vibration allows us to know the current absorber molecule. The hydrogen can be presented in different configurations: located interstitially, molecular and forming aggregations, as it is shown in figure 3.1 [Kail, 2005].

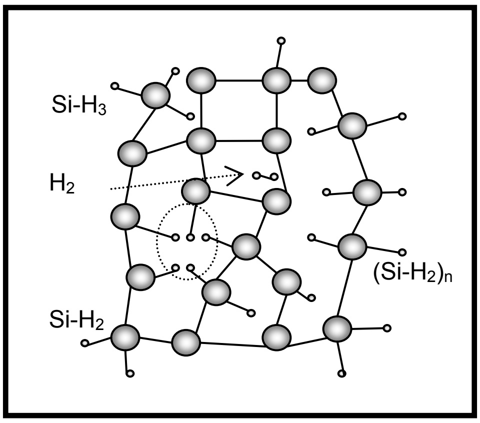

Figure 3.1: Possible structural configurations of Hydrogen in the a-Si:H.

Many theoretical and experimental studies have been reported to gain knowledge into the microstructure of the material and the hydrogen-bonding configuration [Brodsky, 1977). An important absorption band centred at 2000 cm^{-1} corresponding to hydrogen in monohydride bonds (Si-H) can be typically observed in device-quality a-Si:H, whereas hydrogen bonded in either multihydrides (Si-H_2 or Si-H_3) or internal voids gives rise to a contribution around 2100 cm^{-1} [Lukovsky et al., 1979]. Therefore, low signals around 2100 cm^{-1} are required to ensure compactness of the growing material. A quantitative approach is then given by the microstructure factor (R^*):

$$R^* = \frac{I_{2100}}{I_{2100} + I_{2000}} \tag{3.3}$$

where I_k represents the integrated absorption of the corresponding bands. As previously stated, a dominant absorption band around 2000 cm^{-1} is desirable and, consequently, low R^* values ($R^* < 0.1$) are required.

Finally, the hydrogen density (N_H) can be evaluated from the absorption band at 630 cm^{-1}:

$$N_H = AI_{630} \tag{3.4}$$

where $A = 2.1\times10^{19}$ cm^{-3} [Langford et al., 1992] and I_{630} is the integrated absorption of the corresponding band. The peak around 630 cm^{-1} includes the rocking modes of bonded hydrogen in every possible configuration, so the totality of bonded hydrogen atoms is taken into account. In order to obtain the hydrogen content (C_H), a value of 5×10^{22} cm^{-3} for the silicon density (N_{Si}) has been commonly accepted, so C_H results in:

$$C_H = \frac{N_H}{N_H + N_{Si}} \times 100 \qquad at\ \% \tag{3.5}$$

Additionally, the incorporation of oxygen in silicon thin films can be detected by the presence of an absorption band around 1100 cm^{-1} associated to Si-O bonds [Curtins et al., 1986].

c) Secondary Ion Mass Spectroscopy (SIMS)

Secondary Ion Mass Spectroscopy is used to analyze the composition of the samples. Depth profiles of silicon, doping atoms and contaminants have been obtained with an ATOMIKA 3000-30 ion microprobe system. This destructive technique is based in the extraction of the material by sputtering the samples with Ar or O ions and the analysis of the positive secondary ions collected with a mass spectrometer. Thereby, the concentration profiles of the elements constituting the layer are obtained with a detection level in parts per million.

3.1.2 Optical and electrical characterization

a) Transmittance / Reflectance

Transmittance measurements of a-Si:H layers deposited on glass were done with an EPP2000 Spectrometer in the visible and near-infrared wavelength range (λ = 400 - 1200 nm). The measured spectrum indicates the fraction of light transmitted by the sample. The analysis of transmittance curves allows determining the optical gap (E_g) according to Tauc's law [Tauc, 1974] and the thickness of the sample considering the interference pattern [Swanepoel, 1983].

Moreover, the reflectance of ITO layers was measured with the same set-up using an optic fibre in T-configuration. Reflectance spectra before and after depositing the front metallic grid evaluate losses due to shadowing by the front contact.

b) Photothermal Deflection Spectroscopy (PDS)

The optical absorption of a-Si:H layers was measured using the Photothermal Deflection Spectroscopy (PDS) technique. The basic phenomenon studied in the PDS technique is the deflection of a light beam when it travels through a medium with an induced gradient in its refractive index [Boccara et al., 1979]. In our case, the layer under study is submerged into a liquid (Fluorinert FC72^{TM} by 3M in our set-up), whose refractive index exhibits a clear thermal dependence. A monochromator is used to select the wavelength of the radiation reaching the sample, which absorbs a fraction of the incident light. The absorbed light induces a heating of the sample by non - radiative recombination. The increasing temperature of the layer causes a temperature gradient in the liquid, so the refractive index also experiences a variation. This gradient leads to the deflection of a laser beam which can be quantified by means of the corresponding detector. A detailed description of the experimental set-up and the calculation of the optical absorption coefficient (α) can be obtained from [Voz, 2000].

The most relevant characteristic of PDS is its high sensitivity allowing the detection of very low optical absorption levels ($\alpha d < 10^{-5}$). Then, PDS complements standard transmission measurements to obtain the optical absorption spectrum in the whole visible and near infrared range. Typical spectra for c-Si, μc-Si:H and a-Si:H samples are described in [Voz, 2000]. Parameters as the optical band gap and the subgap defect density can be obtained from the treatment of the optical absorption spectra [Soler, 2004].

3.2 Characterization of solar cell precursors

3.2.1 Spectroscopic Phase Modulated Ellipsometry in the UV-visible

Ellipsometry is a sensitive technique used to determine optical properties of surfaces and thin films. In an ellipsometry measurement we analyze the change in the polarization of monochromatic light after being reflected on the polished surface of the sample. Two main properties make this technique very useful in different areas (thin films, interface properties, roughness analysis…): data are easily obtained and it is a non-destructive technique [Kail, 2005]. Figure 3.2 shows a picture of the Jovin Yvon UVISEL set-up used in this thesis.

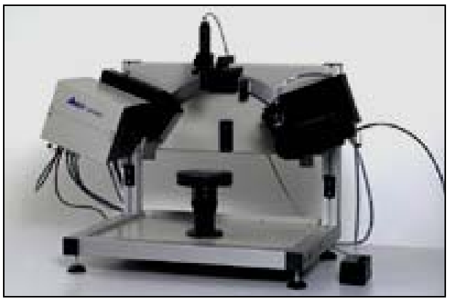

Figure3.2: Picture of the Jovin Yvon UVISEL set-up located at the LPICM in Paris.

A schematic of the different parts in the Jovin Yvon UVISEL set-up is shown in figure 3.3. The right branch is the excitation one containing a Xenon lamp (125 W) and a polariser-photoelastic modulator. The left one is the analysis branch, containing an analyzer and a detector (monochromator-photomultiplier).

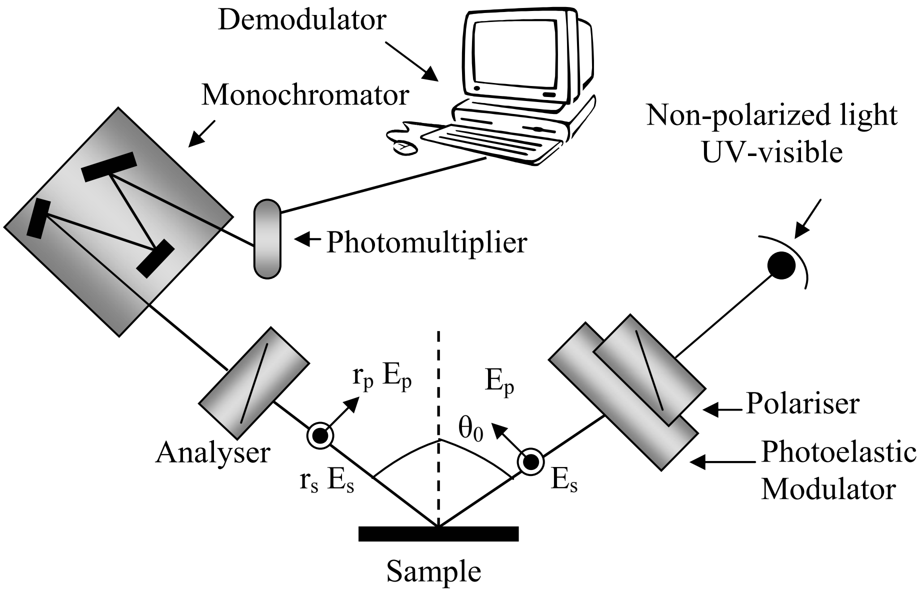

Figure 3.3: Schematic of the Spectroscopic Phase Modulated Ellipsometry measurement in the UV-visible.

The focalised beam of the lamp is captured by an optic fibre before entering the polariser. The angle between the polarizer and the modulator is 45º, while the angle at which the light reaches the surface of the sample is $\theta_0 = 70º$. The role of the photoelastic modulator is to change the polarization state while introducing a time lag between E_p and E_s. To achieve this, a silica bar (with high refraction index) with a piezoelectric crystal is placed in the modulator. The modulation frequency is 50 kHz, the same as the silica bar resonance frequency. After the reflexion in the sample, the polarization state of the beam is analysed by another polarizer similar to the first one. Therefore, the coefficients r_p and r_s are obtained. After the analyser, the light is guided through an optic fibre to the monochromator (filter) and then detected by the photomultiplier. The entire left branch is equipped with stepping motors controlled by the computer [Kahl, 2005]. The change in the polarization state of the incident and reflected beams is determined by two angles named Δ and Ψ. These angles can be related to all the physical parameters of the sample (thickness, refraction index, absorption coefficient, roughness…).

a) The Models

Ellipsometry is based on the measurement of the pseudo-dielectric function <ε> of the material. In the case of semi-infinite materials (thick enough to allow photon absorption before arriving to the substrate) with a polished surface, <ε> is given by:

$$\langle \varepsilon(\omega) \rangle = \sin^2\theta_0 \left(1 + \left(\frac{1-\rho}{1+\rho} \right)^2 \tan^2\theta_0 \right) = \langle \varepsilon_1(\omega) \rangle + i \langle \varepsilon_2(\omega) \rangle \qquad (3.6)$$

where ρ is obtained from the measurement of the reflection coefficients r_p and r_s, which are related to the angles Δ and Ψ as:

$$\rho = \frac{r_p}{r_s} = \tan(\Psi)\exp(i\Delta) \qquad (3.7)$$

It is especially interesting to analyse the imaginary part of the dielectric function $<\varepsilon_2>$ because in absence of phonons only transitions between the valence and the conduction band affect this term [Van Hove, 1974]. Figure 3.4 shows the imaginary part of the pseudo-dielectric function for c-Si, a-Si:H and μc-Si:H samples [Aspnes et al., 1984], [Jellison et al., 1993].

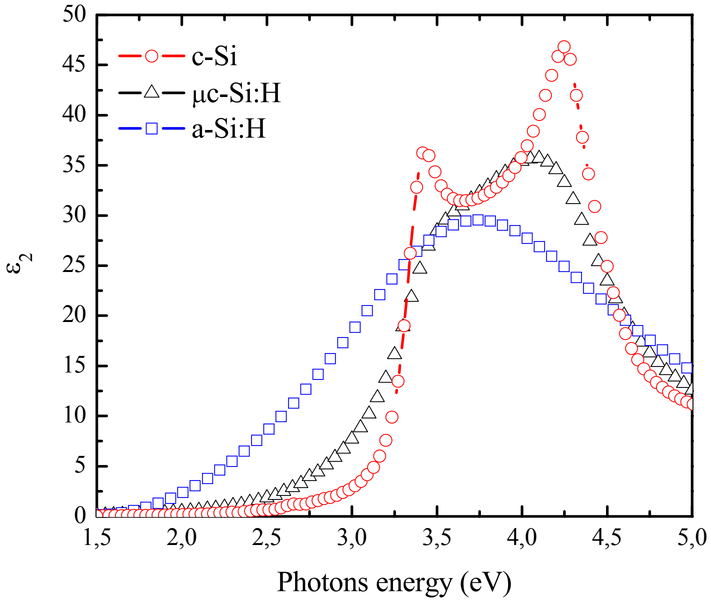

Figure 3.4: Imaginary part of the pseudo-dielectric function of c-Si, a-Si:H and μc-Si:H samples.

The a-Si:H spectrum shows a peak centred around 3.5 eV, while the c-Si spectrum has two peaks centred in 3.4 eV and 4.2 eV. As expected, the μc-Si:H sample has an intermediate spectrum with a soft peak at about 4.2 eV. The characterization of the samples in terms of film thickness and microstructure has been done fitting the experimental data to optical models.

b) The Tauc-Lorentz Model

The interpretation of the ellipsometric measurements in a-Si:H thin films requires basically the parametrization of the optical properties as a function of the photon energy. Jellison and Modine [Jellison et al., 1994] have developed a model to define the dielectric function of amorphous materials. In the visible and near infrared range, the pseudo-dielectric function of an amorphous semiconductor can be described as a dispersion law based on the Lorentz oscillator and the Tauc's joint density of states [Jellison et al., 1996]. This model describes the energy dependence of the imaginary part of the dielectric function ε_2 as follows:

$$\varepsilon_2(E) = \frac{A\, E_0\, C\left(E - E_g\right)^2}{\left(E^2 - E_0^2\right)^2 + C^2E^2} \cdot \frac{1}{E}, \qquad E > E_g \tag{3.8}$$

The four parameters of this law offer valuable information about the structure of the material: the optical gap E_g (eV), the factor A (eV) related to the density of the material, the position of the peak in the spectrum defined by E_0 (eV) and, finally, the disorder factor C (eV).

c) Effective medium theory

We have used the effective medium theory to model stacks of several layers and also in the case of heterogeneous layers. In this case, the effective medium theory is only applicable if the dimension of the crystallites into the amorphous phase is smaller than the wavelength used in the analysis. Otherwise, for bigger dimensions the model cannot be used because diffusion and diffraction phenomena of the incident light should be taken into account.

The effective medium theory is based on the addition of the polarization effects. Then, the effective pseudo-dielectric function of the sample $<\varepsilon_{eff}>$ is obtained from the pseudo-dielectric functions $<\varepsilon_i>$ of the constituent materials and their volumetric fractions, f_i [Ayral et al., 2006]:

$$\frac{\varepsilon_{eff} - \varepsilon_a}{\varepsilon_{eff} - p\varepsilon_a} = \sum_i f_i \frac{\varepsilon_i - \varepsilon_a}{\varepsilon_i - p\varepsilon_a} \tag{3.9}$$

where $<\varepsilon_a>$ is the pseudo-dielectric function of the amorphous phase and p is a coefficient that depends on the geometry of the inclusions (p = 2 if we consider them spherical). In particular, the Bruggemann's approximation [Bruggemann, 1935] considers symmetrical the amorphous phase and the inclusions, so equation (3.9) can be rewritten as:

$$\sum_i f_i \frac{\varepsilon_i - \varepsilon_{eff}}{\varepsilon_i - 2\varepsilon_{eff}} = 0 \tag{3.10}$$

A good example of the application of this model are μc-Si:H layers [Fontcuberta, 2004]. The effective pseudo-dielectric function is then an adjusted linear combination of an amorphous phase $<\varepsilon_a>$ obtained with the Tauc-Lorenz model, microcrystalline phases $<\varepsilon_{lg}>$ (little grain) and $<\varepsilon_{bg}>$ (big grain) obtained from the Jellison models [Jellison, 1993] and a void fraction $<\varepsilon_v>$. Pseudo-dielectric functions for other materials can be obtained from [Palik, 1991].

3.2.2 The QSSPC technique

The Quasi-Steady State Photoconductance Technique (QSSPC) is probably the most common technique to measure the passivating properties of thin films deposited on crystalline silicon. In heterojunction solar cells both bulk and surface recombination mechanisms must be considered. While bulk recombination directly depends on the quality of the c-Si substrate, surface recombination is determined by the passivation quality at the interfaces in the device. Any recombination process U can be associated to its characteristic lifetime:

$$\tau = \frac{\Delta n}{U} \tag{3.11}$$

where $\Delta n = n - n_o$ is the excess minority carrier density (n_o is the carrier density under thermodynamical equilibrium).

a) <u>Bulk recombination in c-Si</u>

In the bulk of c-Si wafers, the lifetime is given by the effect of three main recombination processes: radiative, Auger and *Shockley-Read-Hall* recombination:

$$U = U_{Rad} + U_{Aug} + U_{SRH} = \frac{\Delta n}{\tau_{Rad}} + \frac{\Delta n}{\tau_{Aug}} + \frac{\Delta n}{\tau_{SRH}} = \frac{\Delta n}{\tau_b} \tag{3.12}$$

In *radiative recombination* an electron of the conduction band neutralises a hole in the valence band emitting a photon whose energy corresponds to the semiconductor band gap [Green, 1982]. Since silicon has an indirect band gap, this process is almost negligible compared to the other ones.

In the case of *Auger recombination* the energy excess of a band-to-band recombination process is given to a third carrier, either a hole or an electron. This recombination mechanism can be especially important at high injection levels or in highly doped wafers.

Finally, *Shockley-Read-Hall recombination* [Shockley et al., 1952], [Hall, 1952] takes place through a defect in the band gap and the energy excess is delivered in the form of phonons. This recombination process via defects is not intrinsic to the semiconductor and it could be totally removed by producing a perfect crystal. However, since most of the c-Si used for photovoltaic applications is low-quality recombination via defects is dominant in commercial c-Si solar cells. This effect is especially relevant at low injection levels [Martin, 2004].

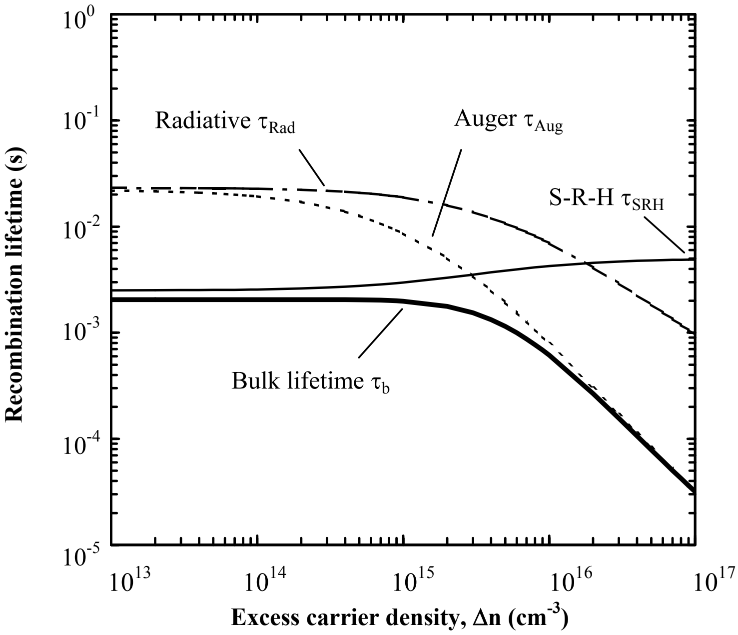

Figure 3.5: Dependence of τ_b on Δn with a base doping $N_A = 4.3\times10^{15}$ cm^{-3}, $\tau_{n0} = \tau_{p0} = 2.5$ ms. At low-injection, τ_b is mainly determined by τ_{SRH}. On the other hand, at high-injection τ_b is dominated by Auger recombination [Martin, 2004].

Figure 3.5 shows the influence on the bulk lifetime of the three recombination mechanisms. As it can be observed, SRH recombination limits the τ_b value at low injection levels, while Auger recombination becomes the main factor at high injection levels. From now on, we will consider high-injection when $\Delta n > 10\times N_{dop}$ and low injection when $10\times n_i < \Delta n < 10\times N_{dop}$, where N_{dop} is the base doping of the wafer and n_i is the intrinsic carrier density.

b) Surface recombination

A high defect density is expected at the semiconductor surface, since the crystalline network is completely lost. The defect density is mainly due to dangling bonds, but additional defects can be created either chemically or mechanically during the fabrication process of the device. Considering that the units of surface recombination are ($cm^{-2}\times s^{-1}$), it is more easily described by an effective recombination velocity measured in ($cm\times s^{-1}$) than by a lifetime. Then, the effective surface recombination velocity S_{eff} can be defined as [Kim et al., 1980]:

$$U_s = S_{eff} \cdot \Delta n \tag{3.13}$$

where Δn is the excess minority carrier density at the limit of the space charge region created at the c-Si surface.

c) Characterization of the recombination mechanisms

The QSSPC Technique was designed and implemented firstly by R.A. Sinton and A. Cuevas [Sinton, 1996]. This technique allows the contactless characterization of solar cell precursors. The system is based on a RF bridge with an inductive coil that generates electromagnetic fields within the wafer. Variations in the conductivity of the wafer modify these fields leading to a variation of the effective inductive value, thus changing the output voltage of the bridge. More details on this technique can be found in [Martin, 2004], [Ferré, 2008].

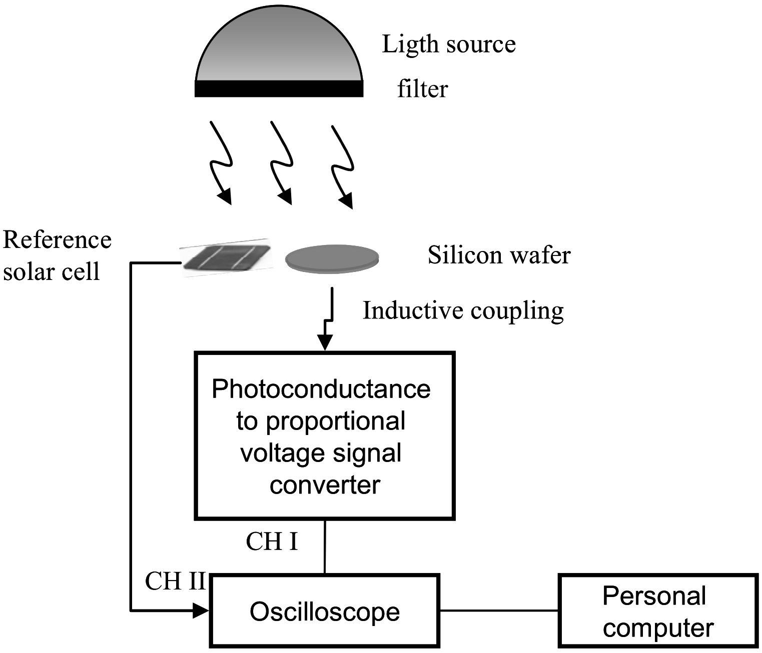

Figure 3.6: Block diagram of the QSSPC set-up.

The instrument used in this thesis to measure the effective lifetime τ_{eff} as a function of the injection level Δn was the WCT-100 provided by Sinton Consulting [Sinton, 1999]. Figure 3.6 shows a block diagram of the system that also includes a calibrated solar cell to measure the light intensity, a digital oscilloscope (Tektronix TDS210) and a flash lamp (Quantum Qflash model X2). Two magnitudes are measured by this system:

- *Photoconductance of the sample $\Delta\sigma$*: a voltage signal proportional to this magnitude is measured at CH I in the oscilloscope. From this, Δn_{av} can be estimated by applying the following equation:

  $$\Delta\sigma = w \cdot q \cdot (\mu_n + \mu_p) \Delta n_{av} \tag{3.14}$$

  where *w* is the wafer thickness, q is the elementary charge and μ_n (μ_p) is the mobility of electrons (holes). This magnitude is measured in Siemens (S).

- *The light intensity*: a voltage signal proportional to the short-circuit current of the calibrated solar cell placed next to the c-Si wafer is measured at CH II. From this magnitude, the electron-hole pair photogeneration within the wafer G_{ext} (t) can be estimated. To accurately determine $G_{ext}(t)$, it is also necessary to consider an *"effective optical transmission factor"* f_{opt} which takes into account the reflection losses of the sample.

Once these two magnitudes are known, the effective lifetime τ_{eff} can be calculated with the following equation:

$$\tau_{eff} = \frac{w\Delta n_{av}(t)}{G_{ext}(t)} \tag{3.15}$$

In the case of a symmetric structure (the same layer deposited on both sides), we can obtain the effective surface recombination velocity S_{eff} applying:

$$\frac{1}{\tau_{eff}} = \frac{1}{\tau_b} + 2\frac{S_{eff}}{w} \quad \Longrightarrow \quad S_{eff} \leq \frac{w}{2\tau_{eff}} \tag{3.16}$$

where τ_b is the recombination lifetime in the bulk.

A typical τ_{eff} vs. Δn_{av} curve measured by QSSPC is shown in figure 3.7. One important advantage of this technique compared to other alternatives is the wide irradiance range (10^{13} cm^{-3} - 10^{17} cm^{-3}) that can be characterized only by changing the filter in the flash lamp. If high quality c-Si substrates (FZ wafers) are used, the effective lifetime is actually limited by surface recombination ($\tau_b >> \tau_{eff}$). Hence, we usually obtain a good approximation to the upper limit of the effective surface recombination velocity S_{eff}. Furthermore, this technique allows the estimation of the implicit open-circuit voltage V_{oc} of the solar cell precursor:

$$V_{oc} = \frac{kT}{q}\ln\left[\frac{\Delta n\left(N_A + \Delta p\right)}{n_i^2} + 1\right] \tag{3.18}$$

For high injection levels ($\Delta p = \Delta n$), the excess carrier densities can be considered equal to the average excess carrier density measured by QSSPC.

The error in the calculation of τ_{eff} by this technique can be considered lower than 15% taking into account non linearities between photoconductance and the output signal, maladjustments in the optical factor (f_{opt}) or variations in the flash spectrum, among other factors [Martin, 2004].

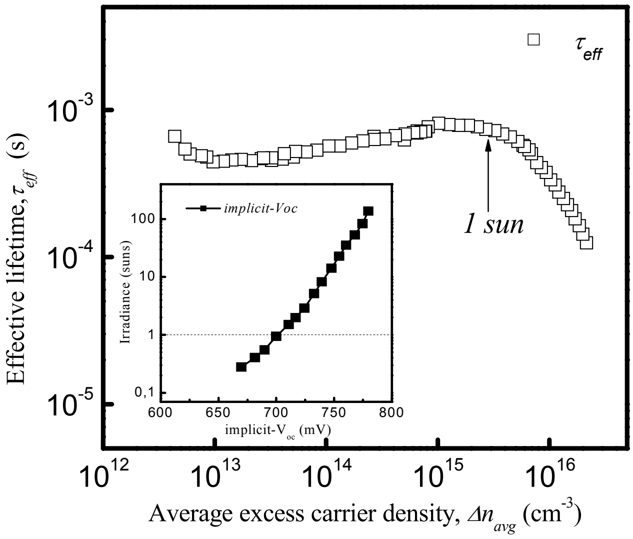

Figure 3.7: Effective lifetime vs. average excess carrier density measured by the QSSPC technique. The arrow points the effective lifetime at 1 sun irradiance. In the inset, implicit-V_{oc} vs irradiance for the same sample.

3.3 Characterization of complete solar cells

3.3.1. Current – Voltage characteristics

The most significant electrical characteristic of a solar cell is the dependence of the current density on the applied voltage (JV curve). The current density is defined as the current divided by the total area of the device. The JV curve can be measured in the dark or under illumination.

It is very important to use a 4-probe system to measure only the actual series resistance of the device avoiding parasitic effects related to the experimental set-up (long cables, etc.) Figure 3.8 shows the JV curve in dark for the same device but measured with 2 probes (one at each side), 3 (one at the emitter, 2 at the back side) and 4 probes (2 at each side). As it can be observed, the series resistance can be overestimated if only 2 or 3 probes are used.

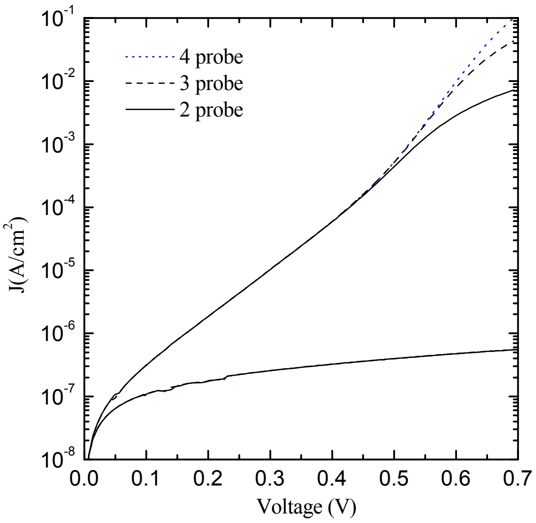

Figure 3.8: Dark JV curves of a solar cell measured with 2, 3 and 4 probes.

The current–voltage characteristics of solar cells based on c-Si can be usually described by a simple two diode-model [Green, 1981]:

$$J = J_{01}\left(\exp\left(\frac{V-R_sJ}{n_1kT}\right)-1\right)+J_{02}\left(\exp\left(\frac{V-R_sJ}{n_2kT}\right)-1\right)+\frac{V-R_sJ}{R_p}-J_{ph} \tag{3.19}$$

where J_{01}/J_{02} are the saturation current densities for each diode and n_1/n_2 are the corresponding ideality factors. In addition, R_s and R_p are the parasitic series and parallel resistances. Usually, we can consider an ideal diode ($n = 1$) while the second one is the recombination diode ($n \approx 2$). The photogenerated current J_{ph} term must be considered under illumination. The standard AM1.5 illumination conditions are summarized in the following table:

Irradiance	1000 W/m^2
Spectral distribution	AM1.5
Incidence	normal
Temperature	25ºC

Table 3.1: Summary of AM1.5 conditions.

A typical JV curve measured under standard AM1.5 irradiance by means of a solar simulator is shown in figure 3.9.

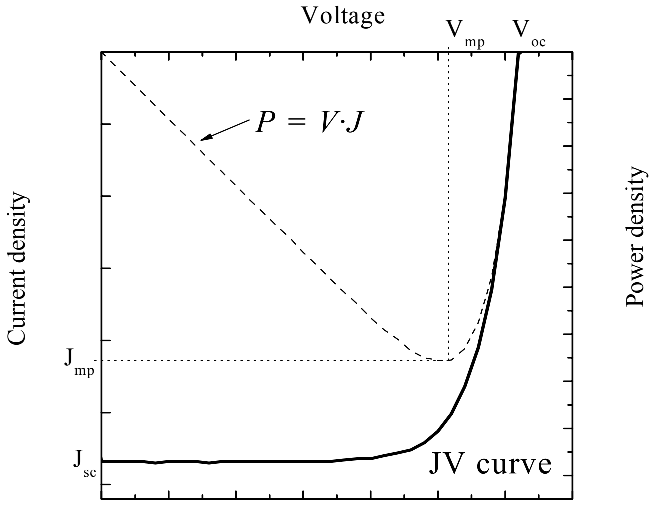

Figure 3.9: Typical JV curve of a solar cell measured under standard AM1.5 irradiance.

The most characteristic parameters of the JV curve under illumination are:

- The open-circuit voltage V_{oc}, which is the voltage between the terminals of the device when the current is zero.
- The short- circuit current J_{sc}, which is the current flowing through the device when the voltage is zero.
- The Fill Factor FF, which is the ratio between the maximum power that the solar cell can generate, divided by the J_{sc} V_{oc} product.

$$FF = \frac{J_{mp} \times V_{mp}}{J_{sc} \times V_{oc}} \tag{3.20}$$

- The conversion efficiency of the device η, which is the ratio of the electrical power density at the maximum power point to the incident power density.

$$\eta = \frac{J_{mp} \times V_{mp}}{P_{ligth}} = \frac{FF(J_{sc} \times V_{oc})}{P_{ligth}} \tag{3.21}$$

From equation 3.21 we deduce that to increase the efficiency of the device it is necessary to have high values of FF, J_{sc} and V_{oc}.

It is important to remark that the temperature should be kept constant at the standard value (25ºC) during the measurement, since the V_{oc} is particularly sensitive to this parameter. The thermal dependence of the V_{oc} supposing that J_{sc} has a little variation can be written as follows [Green, 1998].

$$\frac{dV_{oc}}{dT} = -\frac{V_{go} - V_{oc} + \gamma(kT/q)}{T} \tag{3.22}$$

where V_{go} is the bandgap (~1.2 eV for c-Si) and γ is a coefficient with value ranging from 1 to 4. Considering T =300 K with a usual V_{oc} of 0.6 V and γ~3, we obtain:

$$\frac{dV_{oc}}{dT} = -2.3\, mV/{}^{o}C \tag{3.23}$$

which represents a decrease in the V_{oc} of 0.4% per ºC for diffused c-Si solar cells. In the particular case of heterojunction solar cells the thermal dependence of the V_{oc} is slightly lower (~ -2 mV/ºC).

3.3.2. Spectral Response

Spectral response (SR) measurements have been performed to get detailed information about the current generation process in the solar cell. The spectral response is defined as the amount of current collected J_{ph} by the device per watt of incident light of a given wavelength (λ) for an external voltage applied V.

$$SR(V,\lambda) = \frac{J_{ph}}{P(V,\lambda)} \tag{3.24}$$

The spectral response measurements were performed with a set-up formed by a Xenon gas lamp followed by a monochromator and also a lock-in amplifier. In order to measure the spectral power density P (V,λ) reaching the solar cell for each wavelength we used a calibrated silicon photodetector as a reference.

The External Quantum Efficiency (EQE) can be calculated from the spectral response of the device offering a more physical meaning. The EQE is defined as the fraction of incident photons at a wavelength λ transformed into an electron-hole pair collected at the contacts of the device. The relation between SR and EQE is simply given by:

$$EQE(V,\lambda) = SR(V,\lambda) \times \frac{1241}{\lambda} \tag{3.25}$$

This measurement is basic for a good optimization of the device, since it can distinguish the effect of different layers of the device. For short wavelengths the EQE curve is affected by the front contact and the quality of the emitter, whereas for longer wavelengths the curve is dominated by the quality of the back contact. Furthermore, the Internal Quantum Efficiency can be calculated if the reflectance R(λ) of the front contact is known:

$$IQE(V,\lambda) = \frac{EQE(V,\lambda)}{(1-R(\lambda))} \tag{3.26}$$

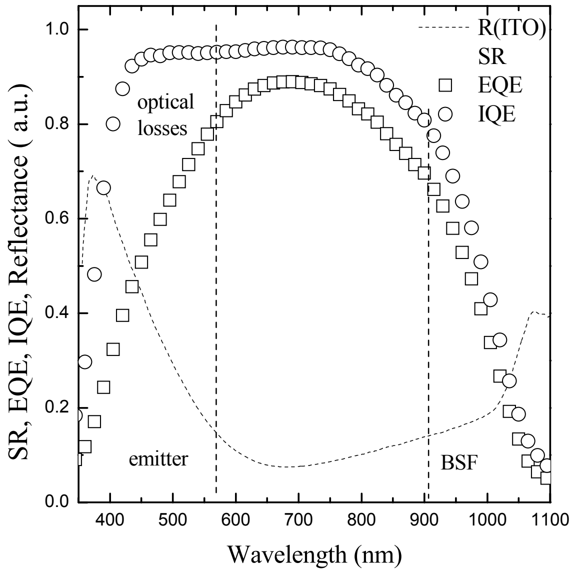

Figure 3.10: Comparison of the SR, EQE, IQE and R curves measured for the same heterojunction solar cell.

The IQE curve does not consider photons reflected at the front contact but only those that are actually absorbed within the device. Thereby, we can obtain valuable information about the heterojunction quality without influence of technological issues such as the optimization of the antireflection coating or the metallic front grid. A comparison of the different SR, EQE, IQE and reflectance curves is shown in figure 3.10.

Chapter 4: Amorphous and microcrystalline silicon deposited by HWCVD

"La mejor estructura no garantizará los
resultados ni el rendimiento. Pero la estructura
equivocada es una garantía de fracaso"
P. Drucker

In this chapter, the different materials used in this thesis to fabricate heterojunction silicon solar cells are briefly described. On the one hand, the main properties of thin silicon films grown by HWCVD are reviewed. On the other hand, the criteria used to select which materials are better for our devices are discussed. Both the intrinsic material used in the buffer layer and the doped layers for the emitter and back contact are considered.

4.1 Between a-Si:H and μc-Si:H

Amorphous silicon (a-Si) is the non-crystalline form of silicon. In its crystalline form, each silicon atom is bonded to four neighbouring silicon atoms forming a tetrahedron. Although this is also the case in a-Si, it does not actually form a continuous crystalline lattice. In amorphous silicon some atoms may have dangling bonds, which occur when those atoms are not bonded to four neighbouring atoms. These dangling bonds are defects in the continuous random network, and can be partially *passivated* by introducing hydrogen atoms in the material. Then this material becomes hydrogenated amorphous silicon (a-Si:H), which is actually the form used in electronic applications. Hydrogenated amorphous silicon is usually referred as amorphous silicon to simplify, but it must be clear that there must be significant hydrogen content to obtain acceptable electronic properties.

The beneficial role of hydrogen dilution in PECVD deposited a-Si:H has been widely accepted since observations of improved stability were first reported [Guha et al., 1981]. Moderate hydrogen dilutions (lower than those used in PECVD) have also led to reduced defect metastability in a-Si:H obtained by Hot-Wire CVD [Bauer et al., 1998].

Hydrogenated nanocrystalline silicon (nc-Si:H) or **microcrystyalline silicon** (µc-Si:H) are allotropic forms of silicon where an amorphous phase coexists with embedded small grains of crystalline silicon. The difference between nc-Si:H and µc-Si:H comes solely from the grain size of the crystallites, as is shown in table 4.1. These small-grain materials can be grown at moderate substrate temperatures [Bergmann, 1999]. By contrast, **polycrystalline silicon** (poly-Si) consists only of crystalline silicon grains separated by grain boundaries. This type of material is usually fabricated at high substrate temperatures without requirement of added hydrogen.

Symbol	Description	Feature size
a-Si:H	single phase amorphous	none
nc-Si:H	two phase amorphous and crystalline	<20nm
µc-Si:H	two phase amorphous and crystalline	<1µm
poly-Si	single phase with grain boundaries	>1µm

Table 4.1: Definitions of various morphologies of thin silicon films.

Anyway, the classification attending to the grain size is still controversial and the terms µc-Si:H and poly-Si:H can be often found in the literature referring to nc-Si:H films. Furthermore, a variety of thin film silicon materials produced near the onset of crystallisation, which exhibit very promising properties, have gained interest during the last years. Thus, polymorphous silicon (pm-Si:H) [Roca i Cabarrocas et al., 1998] or protocrystalline silicon (pc-Si:H) [Koh et al., 1999], [Fontcuberta i Morral et al., 2001] are new terms that have been recently introduced into the terminology of thin film silicon technology.

A possible advantage of nc-Si:H and μc-Si:H over a-Si:H is that higher mobilities can be usually achieved due to the presence of crystallites. They also show an increased absorption in the red and infrared wavelength range, which is really relevant in thin film silicon solar cells. Besides, in part as a consequence of their lower hydrogen content, these materials are also more stable than a-Si:H. Here we are referring to the stability against the so called Staebler-Wronski effect [Staebler et al., 1977], because the chemical stability against oxidation is better in a-Si:H material.

Therefore, the need to control the crystallinity of the layers obtained by Hot-Wire CVD is clear. For that purpose, we can basically change the hydrogen dilution (C_H) and the substrate temperature (T_s) [Tsu et al., 1997], [Mahan et al., 2000], [Han et al., 2003]. Other technological parameters such as the filament temperature (T_f) or the process pressure (P) [Soler, 2004] in our HWCVD reactor have also a significant influence in the crystallinity of the films.

A description of the optoelectronic properties that the different materials used in heterojunction silicon solar cells should fulfil is presented next. We will use the term *device-quality* material to summarize all the basic properties required for the different layers. Obviously, these properties are different depending on the function of the layer in the device. We will discuss the intrinsic and doped material separately.

4.2 *Device-quality* intrinsic amorphous silicon deposited by HWCVD

The interest for good intrinsic amorphous silicon in heterojunction solar cells lies basically in obtaining a non defective layer with good passivation properties. In addition, this intrinsic material must allow the current flow through the thin buffer layer without blocking the electric field. These two premises have been considered for the optimization of the intrinsic a-Si:H deposited by HWCVD.

In this work, we have considered four main parameters to determine the quality of the intrinsic a-Si:H buffer layers for the emitter (or low temperature BSF) of heterojunction solar cells: the dark conductivity σ_d, the photoconductivity $\sigma_{ph},$ the absorption coefficient α and the optical bandgap E_g.

Low σ_d values ($\sigma_d < 1\times10^{-10}\ \Omega^{-1}cm^{-1}$) are desired as an indication of the absence of electronically active impurities [Torres et al., 1996]. On the other hand, σ_{ph} is expected to reach high values (above $10^{-5}\ \Omega^{-1}cm^{-1}$) indicating a reasonably low recombination of the photogenerated carriers. Nevertheless, it is the ratio $S = \sigma_{ph}/\sigma_d$ the most important parameter to consider. S accounts for the electrical behaviour of the material both under illumination and in dark conditions, being values above 10^5 desirable for the application of the material in solar cells [Schroop et al., 1994]. Concerning the optical properties, α is expected to be above 2×10^4 cm^{-1} at 600 nm, whereas E_g in the range of 1.6 - 1.8 eV (depending mainly on the hydrogen content and microstructural properties) is expected for a-Si:H layers. All the above-mentioned properties are the optimal values for the active layer of a thin film solar cell, although solar cells with reasonable performance can be also obtained with active layers not completely fulfilling all the requirements.

As a starting point, we have considered the previous studies for the fabrication of thin film solar cells with the HWCVD system at the UB [Fonrodona, 2003], [Soler, 2004]. This experience on a-Si:H and μc-Si:H deposition has been very useful to readily obtain good quality layers. In a first approximation, we have optimised the layers deposited on glass substrates in terms of the four mentioned parameters. However these results are only reference values, since the growing mechanisms could differ significantly on c-Si wafers.

Name	I_f **(A)**	T_s **(ºC)**	***P*** **(mbar)**	SiH_4 **(sccm)**	H_2 **(sccm)**	C_H **(%)**	r_d **(A/s)**
Hp	12.9	200	1×10^{-2}	2	0	0	3.89
Mp	12.9	200	3.5×10^{-3}	2	0	0	3.85
Lp	12.9	200	1.5×10^{-3}	2	0	0	3.00
VLp	12.9	200	4.0×10^{-4}	2	0	0	1.17

Table 4.2: Deposition conditions studied for the intrinsic layers. The temperature of the tantalum wire is 1650ºC in all cases.

In table 4.2 there is a summary of the deposition conditions studied for the intrinsic layers. It is important to remark the absence of added hydrogen ($C_H = 0$) in all cases, as this is one of the most critical parameters to determine the amorphous or microcrystalline growth [Soler, 2004]. It is widely believed [Mahan et al., 1991] that the abundance of atomic hydrogen on or near the growing surface in HWCVD leads to the deposition of μc-Si:H films rather than a-Si:H ones. Mahan *et al.* proposed that the interaction of atomic hydrogen with the growing surface, either by breaking or inserting into the weak Si-Si bonds, leads to the deposition of an ordered Si film. Heintze *et al.* [Heintze et al., 1996] speculated that the surface reaction rate of adsorbed H-atoms has to be faster than the inflow of growth precursors (growth rate) to avoid trapping H-atoms in voids, which is detrimental for the film quality.

Instead of the hydrogen flow, in this study we have varied the process pressure, which is also a critical deposition parameter. The process pressure *P* was varied according to the aperture of the butterfly valve of the reactor, while the rest of the deposition conditions were kept constant. In particular, the distance between the wires and the substrate was also constant, since it significantly influences the microstructure of the layers.

A higher deposition rate, leading to disordered and porous material, is expected as P increases, although also an abrupt transition to μc-Si:H material is desired. In fact, we have observed by Raman spectroscopy that over 1×10^{-2} mbar the layer starts to grow microcrystalline, while below this pressure all the samples were amorphous (figure 4.1). These results were confirmed by Ellipsometry measurements that evidenced a band gap close to 1.7 eV in all cases.

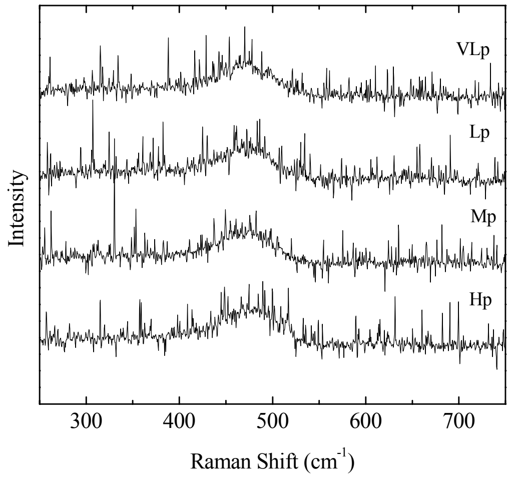

Figure 4.1: Raman spectra for the samples deposited at different process pressures (see table 4.2).

On the other hand, FTIR measurements in the range 2200 - 1900 cm^{-1} (figure 4.2a) also show a clear transition in the microstructure of the samples. A dominant contribution around 2000 cm^{-1} was observed at higher pressures, which indicates an important fraction of monohydride bonds (Si-H) surrounded by a dense network. An increasing contribution around 2100 cm^{-1} was obtained for samples grown at lower pressures. This feature indicates the presence of either multihydride ($Si\text{-}H_2$ or $Si\text{-}H_3$) or monohydride bonds in a porous structure. The important contribution around 2100 cm^{-1} has been commonly associated to low-quality a-Si:H material. From FTIR measurements, we can also extract the C_H in our layers by analyzing the behaviour around 630 cm^{-1} (not shown). This analysis evidences an increase in the C_H from 5% (sample Hp) to 11% (VLp). In layers deposited by PECVD a C_H of 12% is usually required for good quality layers, but it has been demonstrated that device-quality layers can be obtained by HWCVD having much lower C_H values [Mahan et al., 1991]. As a conclusion of this study, it seems that higher pressures (Mp, Hp) lead to improved structural properties.

However, information about the oxygen content can be also obtained by FTIR measurements from the band around 1100 cm^{-1} that corresponds to the Si-O bond (figure 4.2b). In this case the Hp sample shows an important signal that evidences post-oxidation, which is usually an indication of porosity and lower density of the film.

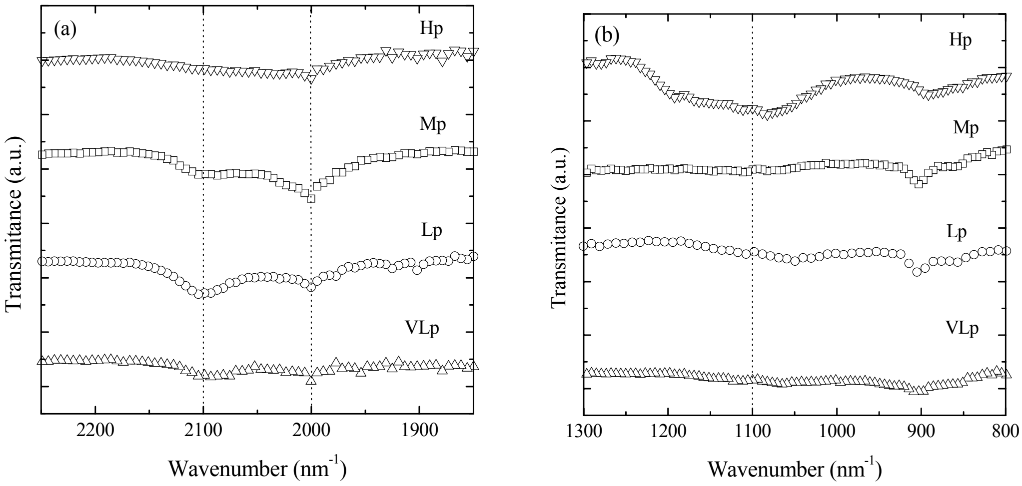

Figure 4.2: FTIR measurements for the samples deposited at different process pressures (see table 4.2).

Afterwards, the dark conductivity and photoconductivity of these layers were measured. The results are shown in figure 4.3.

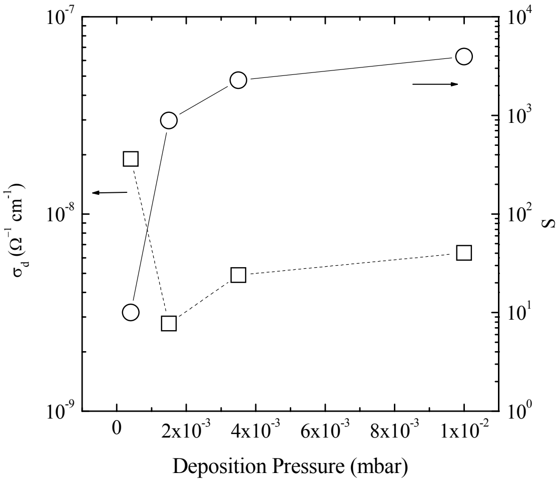

Figure 4.3: Values of σ_d and S for the samples deposited at different process pressures (see table 4.2).

The minimum dark conductivity is obtained at 1.5×10^{-3} mbar, although the samples deposited at higher pressures maintain also a similar value below 10^{-8} Ω^{-1}cm^{-1}. This dark conductivity is not as low as desired ($< 10^{-10}$ Ω^{-1}cm^{-1}) for high quality intrinsic films. This could be due to the presence of unintentional doping in the layer, mainly contamination with oxygen coming from the chamber, wire aging, or the residual pressure achieved in the system [Fonrodona, 2001]. Regarding the $S = \sigma_{ph}/\sigma_d$ ratio, it clearly increases with the process pressure, though in conclusion the samples Lp, Mp, and Hp are of similar quality. On the other hand, the sample at the lowest pressure VLp is remarkably worse in terms of electrical properties.

Finally, the absorption coefficient α was measured for all the samples in the pressure series. In figure 4.4, the absorption coefficient of the Mp sample is shown compared to a reference a-Si:H layer obtained by PECVD. In the visible region (hν > 1.8eV), the α of the Mp sample is slightly lower compared to the a-Si:H model. In fact, at 600nm the value of α is just around 10^{-4} cm^{-1}, while the initial target was 2×10^{-4} cm^{-1}. By contrast, the absorption in the low energy range, related to the concentration of deep states in the gap [Voz, 2001] is higher for the Hp sample. The value in the range of 10 cm^{-1} corresponds to a defect density close to 10^{16} cm^{-1}. These defects act as recombination centres reducing the photoconductivity.

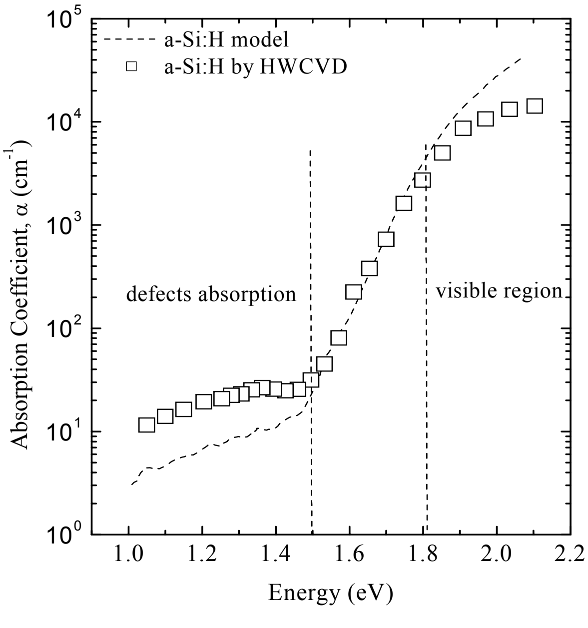

Figure 4.4: Optical absorption coefficient of a reference a-Si:H layer deposited by PECVD compared to the Mp sample. The absorption coefficient was measured by PDS.

Finally, we have reduced the substrate temperature T_s to investigate its influence on the properties of the material. It is known that dense high quality a-Si:H films can be deposited by HWCVD at higher substrate temperatures, but low T_s values usually lead to more stable films [Seitz et al., 2001]. We have deposited intrinsic layers at temperatures close to 100ºC observing that they were quite similar to those obtained at 200ºC. In our HWCVD system the heating due to the wire is relevant at low substrate temperatures (T_s<200ºC). Hence, the actual temperature could be around 150ºC though we fixed the substrate heater to only 100ºC. We have also observed that the passivation quality of the buffer layer is even better when it is deposited at T_s=100ºC and annealed at 200ºC during the deposition of the doped layer.

In the particular case of heterojunction solar cells, we have to consider also the differences in the growing process on c-Si substrates. We have observed that the desired abrupt heterojunction onto the c-Si surface is obtained with the material deposited at only 3.5×10^{-3} mbar. Then, better materials in terms of conductivity result in total or partial epitaxy on c-Si (for instance Hp) and they are absolutely discarded for our application. Moreover, the properties measured in 1 μm-thick a-Si:H layers deposited on glass (like the ones presented above) are quite difficult to compare with extremely thin (5 nm) a-Si:H layers on c-Si. For instance, in our case the properties of the buffer layer can be strongly affected by the deposition of the following doped layer (see chapter 5). As a conclusion, we can consider that even though our layers do not fulfill all the device-quality established properties in terms of material, they certainly achieve all the requirements in terms of passivation and microstructure demanded by heterojunction devices. This will be evident in the analysis of the solar cell precursors during the next chapter.

4.3 Doped amorphous & microcrystalline silicon deposited by HWCVD

In this section we study the optical and electrical properties of both n- and p-type thin silicon films for heterojunction solar cells. Doping of a-Si:H was first demonstrated by Spear and LeComber [Spear and LeComber, 1975], who showed the capability to obtain both p- and n-type material by PECVD. Suitable amounts of either diborane (B_2H_6) for p-type material or phosphine (PH_3) for n-type layers were added to the gas mixture in the reactor. This result demonstrated the enormous potential of a-Si:H. The disordered structure of a-Si:H was supposed to allow the incorporation of dopant atoms into the amorphous network, thus impeding the doping of the material. Later on, the doping mechanism of a-Si:H was further clarified by Street [Street, 1991]. Nevertheless, the doping efficiency of a-Si:H (< 1%) as a disordered material is much lower than in crystalline silicon [Winer et al., 1990].

The HWCVD technique has shown the capability to obtain good quality doped layers in a satisfactory way, comparable to the PECVD ones [Matsumura, 1986], [Mahan et al., 1991] and use them in different device configurations [Mahan, 2006]. The group at UB has demonstrated that state-of-the-art material can be achieved with the HWCVD system for thin film solar cells [Voz, 2001], [Fonrodona, 2003]. In the following section, an analysis of the doped layers, both n-type and p-type, for heterojunction devices is done.

a) <u>n-type material</u>

The most important function of the n-type layers for heterojunction solar cells is to provide the *built-in* voltage and a good electrical contact with the electrodes either for a heterojunction emitter (p-type wafers) or the BSF contact (n-type wafers) of the device. For that purpose, high conductive ($\sigma_d > 20\ \Omega^{-1}\text{cm}^{-1}$) layers are required. Although we will also look for other properties in terms of density and transmittance, the conductivity of the layer will be our main objective.

Name	I (A)	T_s (ºC)	P (mbar)	SiH_4 (sccm)	H_2 (sccm)	PH_3 (sccm)	C_H (%)	r_d (A/s)	σ (Ω^{-1} cm $^{-1}$)
Si1	12.9	200	8×10^2	1	14	0.4	93.3	2.04	22.3
Si2	12.9	200	8×10^2	2	28	0.8	93.3	3.7	62.7
Si3	12.9	200	8×10^2	3	42	1.2	93.3	4.81	39.6
Si4	12.9	200	8×10^2	4	56	1.6	93.3	5.56	14.4

Table 4.3: Deposition conditions and conductivities for the n-doped layers. The tantalum wire temperature was 1650ºC in all cases.

The n-type samples were obtained adding PH_3 to the gas mixture. The deposition conditions used in the studied series of samples are summarized in table 4.3. A high pressure and hydrogen dilution were used in order to induce the formation of microcrystalline layers. The thickness was around 1 μm and the wire temperature was 1650ºC in all cases. Finally, a [P]/[Si] gas phase ratio of 2% was selected, which might differ from the solid phase ratio of the sample. In this case, we have studied the influence of the silane flow in the properties of the layers.

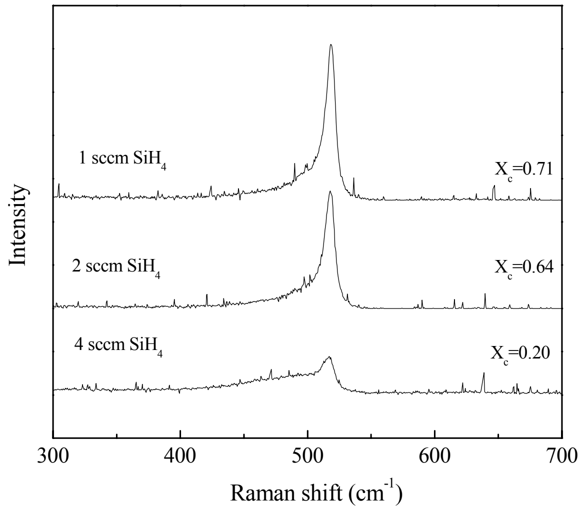

Figure 4.5: Raman spectra for the series of samples in table 4.3.

The dark conductivity was measured first for all the layers in table 4.3. The relatively high σ_d values obtained indicate a microcrystalline structure, also confirmed by the Raman spectroscopy measurements shown in figure 4.5. The microcrystalline structure was especially evident for lower silane flows.

Moreover, a dense structure was evidenced by FTIR spectroscopy measurements. In particular, no contribution around 1100 cm^{-1} corresponding to oxygen incorporation could be observed. The concentration of defect states deduced from the subgap optical absorption was close to 10^{18} cm^{-1}, a relatively high value. In fact, an increase of the defect density after the incorporation of dopant atoms is always expected [Brogueira et al., 1997].

It is important to remark that higher conductivity values were obtained for the more microcrystalline layers (Si1, Si2 and Si3). However, in these layers the optical gap diminishes to values similar to the c-Si value. Hence, if we desire an abrupt heterojunction it is essential to introduce the intrinsic a-Si:H buffer layer. Moreover, the growing mechanisms of the layers deposited on glass, a c-Si wafer, or a previously deposited a-Si:H layer are completely different. The deposition of the same layer onto c-

Si is expected to be more microcrystalline, even producing in some cases an epitaxial growth. By contrast, on the a-Si:H buffer layer a disordered phase of a few nanometres is obtained, appearing later the first grains.

Besides, as it happened with the intrinsic buffer, the doped layers used for heterojunction devices are actually 50-100 times thinner than the samples studied here. This fact means that although we observe a high crystalline fraction on glass, this value is expected to be much lower for the thinner films on first stages of grain nucleation used in solar cells. As we will discuss in the next chapter, only Ellipsometry measurements performed on the solar cell precursors offer confident information about the real structure of the layers. Obviously, the conductivity will be also affected by decreasing the film thickness. Therefore, we have selected only as a starting point the best n-doped microcrystalline layer (Si2) that will be further optimized in final devices.

Nevertheless, microstructural, optical and electrical requirements for device quality n-type layers [Schropp et al., 1998] were achieved by our optimized HWCVD layers.

b) ***p-type material***

The electrical properties are again of critical importance to evaluate the suitability of p-doped layers for heterojunction solar cells. A high conductivity is required to obtain acceptable built-in voltages and also to assure a good contact at the p/TCO or p/metal interfaces. On the other hand, as commented in chapter 2, a small valence band discontinuity is preferred on p-type wafers for a better collection of the photogenerated current. Moreover, a compact material with a low defect density is also required to passivate the back contact of the device. Finally, non-aggressive deposition conditions are desired to prevent the degradation or etching of the intrinsic buffer layer and to maintain an abrupt heterojunction with good passivation properties.

The deposition of thin film p-doped a-Si:H or μc-Si:H by HWCVD is not a simple process [Alpuim et al., 2001]. Actually, it is rather difficult to obtain σ_d values comparable to those reported for state-of-the-art PECVD samples.

On the one hand, p-type doping of silicon thin films is achieved by adding gases with boron content into the deposition chamber. Diborane (B_2H_6) is the most widely employed dopant gas, although some difficulties arise from its use due to its thermal instability [Collins, 1988], [Roca i Cabarrocas et al., 1989]. Alternative more stable gases, such as trimethylboron ($B(CH_3)_3$, TMB), have also allowed the obtention of p-type layers with suitable properties [Brogueira et al., 1997], [Jadkar et al., 2000].

On the other hand, the high hydrogen content favoured by the HWCVD process enhances the formation of boron-hydrogen complexes at low substrate temperatures [Pankove et al., 1985], [Alpuim et al., 2001]. Boron atoms forming these complexes are neutralized by atomic hydrogen and do not effectively contribute to the doping of the material, as they bond with their optimal valence (three-fold coordination). Therefore the doping efficiency is still lower than for n-doped layers. In addition, technological aspects have to be considered in order to prevent cross-contamination in our HWCVD system as the same chamber is shared for both n- and p-doping processes.

Once all the problems associated to p-doped layers are known, special attention has been paid to the optimization of p-type layers in our HWCVD system [Soler, 2004]. However, this is still probably the bottleneck to increase the efficiency of our devices.

The ability to grow p-doped a-Si:H and μc-Si:H layers by Hot-Wire CVD has been demonstrated in previous works [Soler, 2004], [Fonrodona, 2003], [Villar, 2008] for thin film solar cell applications. Whereas μc-Si:H samples showed electrical properties fully comparable to those typically achieved by PECVD, poorer values were obtained for a-Si:H layers. Maximum dark conductivity values of 1×10^{-6} $\Omega^{-1}cm^{-1}$ have been achieved [Soler, 2004], while PECVD samples are usually above 1×10^{-5} $\Omega^{-1}cm^{-1}$ [Street, 1991]. Moderately high substrate temperatures [Brogueira et al., 1997] or post-annealing treatments [Alpuim et al., 2001], which also showed its potential for PECVD layers [Roca i Cabarrocas, 1994], have been proposed as different strategies to overcome that difficulty. By that way, the conductivity of p-doped a-Si:H layers could be increased up to 1×10^{-5} $\Omega^{-1}cm^{-1}$. Nevertheless, higher values would be desirable for heterojunction solar cells.

From the above-mentioned comments it seems clear that we should move in the a-Si:H/µc-Si:H frontier, as it was also the case for n-type layers. However, epitaxy must be prevented and the control of the crystallinity becomes one of the most critical parameters.

As demonstrated by Villar [Villar, 2008] in a complete set of experiments, the crystallinity of the layers strongly depends on all the deposition parameters. In figure 4.6, the influence of filament temperature, process pressure, hydrogen dilution and total flow on the crystallinity of the layers is presented for intrinsic thin layers. In particular, for heterojunction devices, the interest lies on moderate µc-Si:H layers. On the one hand, they have to be microcrystalline enough to collect the current, that is, values near $1\Omega^{-1}cm^{-1}$ have to be achieved. But on the other hand, if the crystalline fraction is very high, the high presence of hydrogen is translated in a higher defect density at the interface, high porosity, possibility of etching of the intrinsic thin layer and risk of epitaxial growth. Therefore, a moderate crystalline fraction is highly recommended.

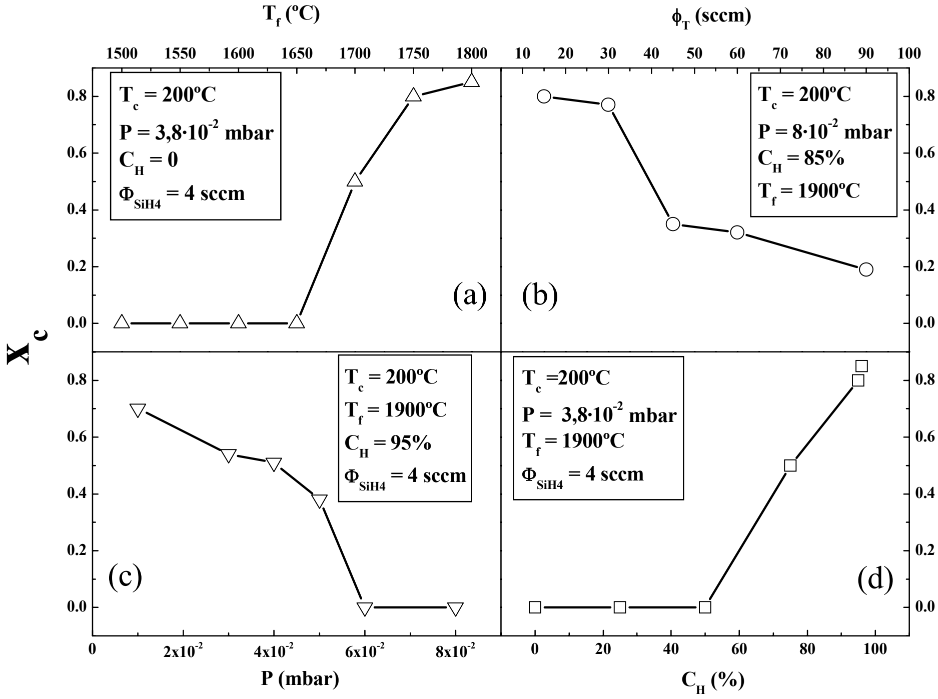

Figure 4.6: Dependence of crystallinity with all the other deposition parameters for intrinsic layers [Villar, 2008].

A first step was made where similar conditions to those leading to our state-of-the-art intrinsic μc-Si:H were used. Nevertheless, T_s was lowered to 125ºC to prevent damaging effects arising from the well-known thermal instability of B_2H_6 [Collins, 1988], [Roca i Cabarrocas et al., 1989], [Peiró et al., 1998], [Voz et al., 2000b]. We have maintained the process pressure in low values ($P = 10^{-2}$ mbar) to assure compact layers and we have worked with no hydrogen dilution (except the one coming with the diborane, 95% diluted into hydrogen) and low silane flows. Hence, our variable parameters have been the filament temperature and the diborane flow.

A series of samples was grown at T_f ranging from 1600ºC to 1750ºC (T_s = 125ºC, C_H = 0%, Φ_{SiH4} = 1.5 sccm, $P = 10^{-2}$ mbar, Φ_{B2H6} = 0.6 sccm). The T_f range was selected after taking into account not only the apparent transition showed in figure 4.6a, but also limitations linked to the Ta filament properties. The use of too low T_f values (below 1400ºC) results in the breakage of the filament due to the formation of silicides, while a higher T_f leads to the desorption of Si atoms returning the metallic wire to its original state [Matsumura et al., 2004]. On the other hand, a too high T_f (above 2000ºC) can cause the incorporation of impurities in the sample [Horbach et al., 1991], [Zedlitz et al., 1993] and the deformation of the wire due to thermal dilatation.

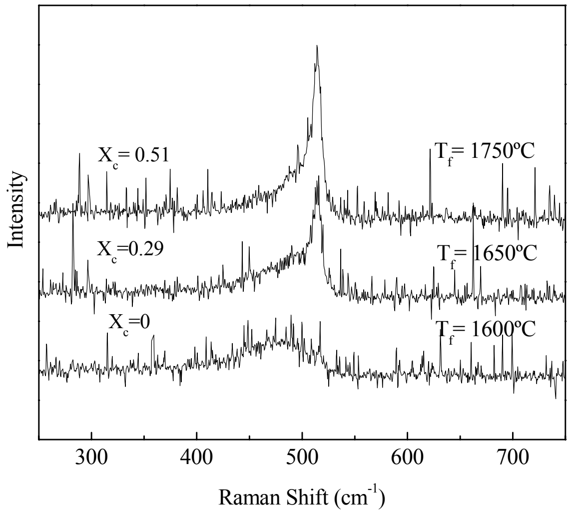

Figure 4.7: Raman measurements for the samples obtained varying the T_f.

In figure 4.7, the Raman measurements of the samples obtained at different filament temperatures are shown. As expected, the crystalline fraction increases with temperature from a totally amorphous structure to X_c higher than 50%. This is also observed in the conductivity measurements where an improvement from values down to 10^{-5} to 10^{-1} Ω^{-1} cm^{-1} for the higher T_f sample is seen.

Subsequently, we have also studied p-doped layers with increased dopant concentration. It is important to remark that two contrary effects are present: the higher hydrogen dilution due to the increased diborane flow (95% diluted in hydrogen) that promotes crystalline growth and the amorphisation produced by greater concentrations of diborane [Voz et al., 2000].

After technological optimization, different p-type materials with an X_c value in the range of 20-50% and good electrical conductivity have been obtained. It is important to remark that all the p-type layers studied were quite thick (≈1 µm), while much thinner layers are used in heterojunction devices. Furthermore, we have to take also into account that the incubation phase and posterior growth strongly depend on the substrate used in each case. The above-mentioned experiments were performed on glass while in heterojunction solar cells the p-layer is grown either on an (i) a-Si:H buffer layer or directly on the c-Si wafer. Consequently, the main analysis and discussion related to p-doped layers was done directly on c-Si wafers. These studies are presented in the next chapter.

Chapter 5: Precursor fabrication & characterization

"Sembremos la llanura antes de arar la loma"
Pablo Neruda

In this chapter, a further step in the characterization of solar cell precursors is presented. Optimized a-Si:H films deposited by HWCVD on Corning glass are the starting point, as it has been discussed in the previous chapter. Then, a-Si:H thin films have been deposited onto c-Si wafers for the fabrication of heterojunction solar cells. The characterization of the solar cell precursor determines the influence of the different substrate in the growing process of a-Si:H films. Besides, a precise determination of the film thickness is also important since this parameter strongly influences the device performance.

In this chapter mainly two powerful techniques have been used to characterize solar cell precursors: the Spectroscopic Ellipsometry and the Quasy-Steady-State Photoconductance technique (QSSPC). In the case of QSSPC measurements, bifacial precursors or alternatively back-passivated structures are required (see figure 5.1). For back passivation usually dielectric hydrogenated a-SiC$_x$ films deposited by PECVD have been used. Since these films allow excellent $\tau_{eff} > 500$ µs values ($S_{eff} < 25$ cm·s^{-1}) [Ferre et al., 2006], QSSPC data determine the passivation quality of the a-Si:H films deposited by HWCVD.

In the first part of this chapter, we will focus on the optimization of heterojunction emitters. As we have basically used p-type wafers, the heterojunction emitter consists in an n-doped layer and, in some cases, an intrinsic buffer layer. Next, the study of low-temperature deposited BSF contacts is considered. This low-temperature BSF is formed by a p-doped layer with again the possibility of inserting a thin intrinsic buffer layer. Finally, some preliminary studies of the symmetric structures on n-type wafers are presented.

Figure 5.1: Diagram of the two precursors used in this work: with a back a-SiC$_x$ passivating layer deposited by PECVD (left) and bifacial precursor with the same layer on both sides (right).

5.1 Characterization of HWCVD heterojunction emitters on p-type wafers

The a-Si:H/c-Si structure has been widely studied for its application in heterojunction solar cells. The complementary properties of each material can lead to the fabrication of high efficiency solar cells: a high short-circuit current can be obtained with the c-Si substrate, while optimized a-Si:H emitters promote high open-circuit voltages. Different emitter configurations considering also the introduction of an intrinsic buffer and the effect of pre- and post-treatments will be studied.

5.1.1 Band diagram of the heterojunction emitter

First, the band diagram of the a-Si:H/c-Si heterojunction emitter is analyzed in detail for a better optimization of the device. As it is shown in figure 5.2, the a-Si:H band gap ($E_{g(a\text{-}Si:H)} \sim 1.8$ eV) is larger compared to the c-Si one ($E_{g(c\text{-}Si)} = 1.12$ eV), while the electron affinity is higher for c-Si.

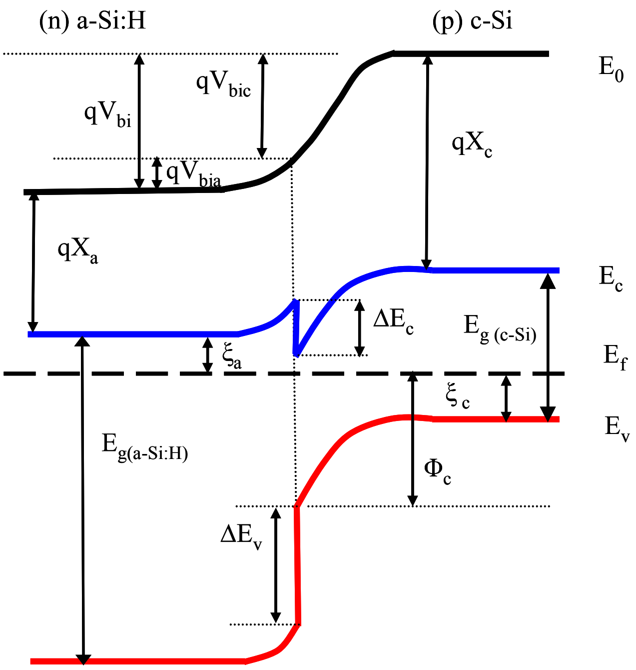

Figure 5.2 Band diagram for a (n)a-Si:H/(p)c-Si heterojunction emitter.

According to the Anderson's law [Anderson, 1962], the discontinuity in the conduction band ΔE_c is defined by:

$$\Delta E_c = q\chi_a - q\chi_c \tag{5.1}$$

where $q\chi_a$ and $q\chi_c$ are the electron affinities of a-Si:H and c-Si, respectively. Then, the discontinuity in the valence band ΔE_v can be calculated:

$$\Delta E_v = E_{g(a-Si:H)} - E_{g(c-Si:H)} - \Delta E_c \tag{5.2}$$

and we define the built-in potential qV_{bi} as:

$$qV_{bi} = q\chi_a + \xi_a - q\chi_c - \xi_c \tag{5.3}$$

where ξ_a and ξ_c are the distances between the Fermi level and the nearest band for the amorphous and crystalline materials. The built-in voltage can be also defined in terms of the intra-band parameters:

$$qV_{bi} = E_{g(a-Si:H)} - \xi_a - \xi_c - \Delta E_v \quad \text{or}$$

$$qV_{bi} = E_{g(c-Si)} - \xi_a - \xi_c + \Delta E_c \tag{5.4}$$

Therefore, there are several ways to increase the qV_{bi} value: increase the band gap of the amorphous material, increase the doping levels of both materials or adjust the band discontinuities. This last option is also related to the difference in the band gap of the materials (Eq. 5.2).

Anyhow, although this ideal approach gives useful information in relative terms for the devices optimization, the Anderson's law is not generally accepted for heterojunction devices due to the strain effects in the bands because of the lattice change [Van der Walle et al., 1997].

Then, an empirical approach generally accepted by the community considers that the band discontinuity can be distributed simply as [Damon-Lacoste, 2007]:

$$\Delta E_c = {}^{1}\!/_{3}(E_{g(a-Si:H)} - E_{g(c-Si)}) \text{ and } \Delta E_v = {}^{2}\!/_{3}(E_{g(a-Si:H)} - E_{g(c-Si)}) \qquad 5.5$$

So in order to increase the built-in voltage of the emitter higher a-Si:H band gap is desired.

5.1.2 Limits to the open-circuit voltage

The interest for a higher built-in voltage lies in its direct relation with the open-circuit voltage of the device. In a very simplified view, the open-circuit voltage is given by:

$$V_{oc} = \text{BUILT-IN VOLTAGE} - \text{RECOMBINATION INFLUENCE} \qquad 5.6$$

Thus, the built-in voltage affects positively the V_{oc} value while recombination losses act as a limiting factor. An analysis by Jensen [Jensen, 2000] of the recombination mechanisms limiting the final V_{oc} of the device considers three main contributions to the saturation current density of the diode, j_0.

$$j_0 = j_{0,bulk} + j_{0,SCR} + j_{0,\text{int}} \qquad 5.7$$

Since in our case we use FZ wafers with a high diffusion length L_{eff}, the term $j_{0,SCR}$ related to recombination within the space charge region can be disregarded [Jensen, 2000]. Concerning the bulk saturation current density $j_{0,bulk}$, it can be calculated as:

$$j_{0,bulk} = \frac{qDn_i^2}{N_A L_{eff}} \qquad 5.8$$

Here q denotes the elementary charge, D is the diffusion constant of the minority carriers, n_i is the intrinsic carrier density, and N_A is the doping density of the absorber layer. If we consider a L_{eff} value of 1000 μm and D = 25 cm/s for FZ p-type wafers with $N_A = 10^{16}$ cm^{-3}, then $j_0 = 45$ fA/cm^2. This value would allow a $V_{oc,bulk}$ value up to:

$$V_{oc,bulk} = \frac{kT}{q}\ln(\frac{j_{sc}}{j_{0,bulk}}) = 700mV \qquad 5.9$$

where we have considered an ideal diode with j_{sc}= 30 mA/cm^2 at one-sun. This high value of $V_{oc,bulk}$ indicates that in most cases the V_{oc} of heterojunction solar cells is limited by interface recombination $j_{0,int}$. Thus, we can consider that:

$$j_0 \approx j_{0,\text{int}} = qS_{it}p_{it} = qS_{it}N_v e^{-\Phi_c/kT} \qquad 5.10$$

where *kT* is the thermal energy, S_{it} the interface recombination velocity, p_{it} the hole concentration at the interface, N_v the effective density of states in the valence band and Φ_c is the effective barrier height in the c-Si (see Fig. 5.2):

$$\Phi_c = qV_{bic} + \xi_c \qquad 5.11$$

Then, considering that mainly interface recombination determines the j_0 value:

$$V_{oc} = 1/q\left\{\Phi_c - AkT\ln\left(\frac{qN_vS_{it}}{j_{sc}}\right)\right\} \qquad 5.12$$

Figure 5.3 shows the expected V_{oc} as a function of S_{it} (Eq. 5.12) considering kT/q = 0.025 eV, J_{sc} = 30 mA/cm^2 and N_v = 1.83×10^{19} cm^{-3} (FZ p-type wafer). The Φ_c value has been approximated by data referenced in the literature considering V_{bi}= 0.75 eV and ξ_c= 0.2 eV [Jensen, 2002]. Alternatively it can be also obtained from Capacitance-Voltage measurements [Gudovskikh et al., 2007]. As it can be observed, especially for higher S_{it} values, the ideality factor also plays an important role. For typical A values (≥ 1.25) the $V_{oc,bulk}$ limit can be only achieved with an excellent interface passivation quality (S_{int} < 100 cm/s).

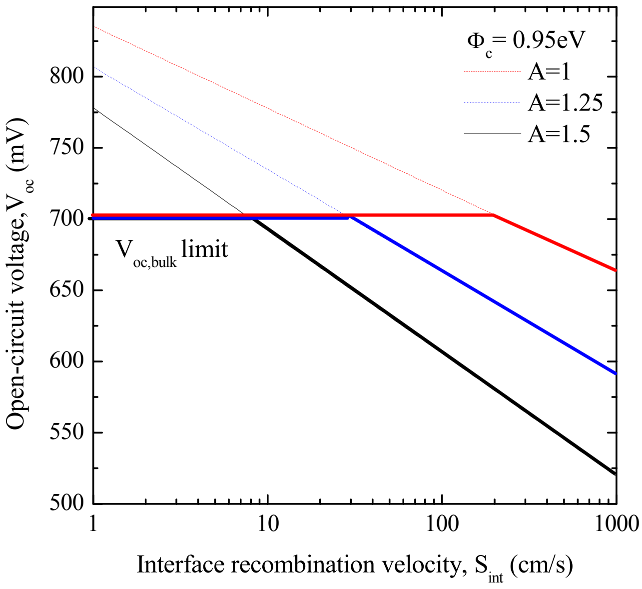

.

Figure 5.3: Calculated V_{oc} (considering a FZ p-type wafer) according to equation 5.11 as a function of S_{it}. The value of Φ_c is considered 0.95 eV in all cases. Different diode ideality factors were also considered to study their influence.

As a conclusion, these are desirable characteristics for the heterojunction emitter:

1. High doping level of the c-Si wafer
2. High doping level of the a-Si:H material
3. High band gap of the a-Si:H material
4. Diode ideality factor close to 1
5. Low interface recombination velocity

Concerning the first point, we have used 0.8 Ωcm wafers for all the studied precursors. It must be considered that a high doping level in the c-Si wafer increases the built-in voltage, but it also degrades the minority carrier diffusion length. The doping level and band gap of the a-Si:H layer are related to the deposition technique, which in our case is HWCVD. The last points 4 and 5 require a clean interface with a non-porous deposited layer to reduce the density of recombination centers. Ellipsometry measurements offer valuable information about the porosity of the deposited layer.

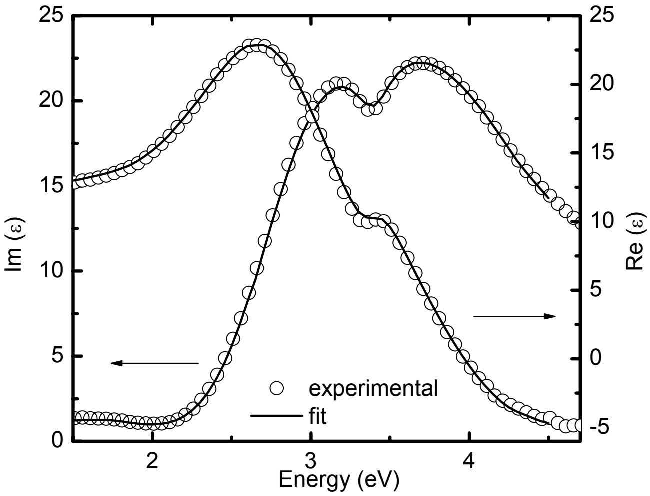

MODEL	thickness (nm)	Xa	Xc	Xv
roughness	3	78	6	16
layer	14.5	100	0	0
substrate	c-Si			

Figure 5.4 Ellipsometry data (symbols) and fitting curves (lines) for an optimized a-Si:H/c-Si heterojunction emitter. On the right, model deduced from the effective media approximation.

As an example, figure 5.4 shows the pseudodielectric function (ε) for an emitter with structure (n)a-Si:H/(i)a-Si:H/(p)c-Si. On the right, the model deduced by fitting the data to an effective media approximation is shown. The model evidences a non-porous layer (void fraction, Xv = 0) of thickness 14.5 nm with a basically amorphous microstructure (amorphous fraction Xa = 100%). The model also indicates a thin superficial layer as a roughness of 3 nm with some crystalline (Xc = 6%) and void fractions (Xv = 16%). The band gap used for the a-Si:H material to fit the layer is 1.8 eV.

This structure was also studied by QSSPC to estimate its potential for heterojunction solar cells. The effective lifetime curve as a function of the minority carrier density is plotted in figure 5.5. Excellent implicit V_{oc} values exceeding 700 mV were obtained with S_{eff} lower than 30 cm·s^{-1} [Muñoz et al., 2007].

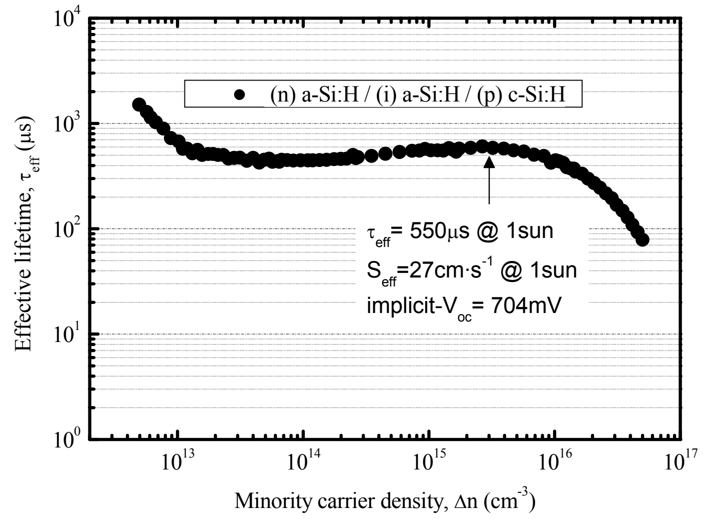

Figure 5.5 Effective lifetime (τ_{eff}) as a function of the excess minority carrier density for an heterojunction emitter (n)a-Si:H/(i)a-Si:H/(p)c-Si . The arrow points the most significant values at one-sun.

5.1.3 Influence of the intrinsic buffer layer

Sanyo has reported an increase of 120 mV in the V_{oc} of heterojunction solar cells when a very thin intrinsic a-Si:H buffer is intercalated between the doped layer and the c-Si substrate [Taguchi et al., 2005]. Hence, these devices are usually referred as HIT solar cells (Heterojunction with Intrinsic Thin layer). It has been proposed that the intrinsic buffer layer drastically reduces interface recombination. It is generally accepted that doped a-Si:H layers present a high defect density in the band gap. These layers directly attached to the c-Si surface seem to deteriorate the properties of the heterojunction. Therefore, the intrinsic buffer layer is expected to improve the interface quality for a better surface passivation, whenever the surface is clean and no damage is created during the deposition process. Nevertheless, other groups have shown that it is also possible to achieve good results without intrinsic buffer layer [Maydell et al., 2006]. Then, the cleaning procedure of the c-Si surface together with the deposition conditions take special relevance in order to reduce the interface defect density [Schmidt et al., 2007]. Also partially epitaxial buffer layers [Centurioni et al., 2004] and different materials as polymorphous silicon have been proposed in the literature [Damon-Lacoste, 2007] with outstanding success.

In order to investigate the influence of the intrinsic buffer layer, we have compared the emitters formed by the same 20 nm (n)a-Si:H layer onto a (p)c-Si wafer with and without an intrinsic buffer layer of 5 nm. The deposition conditions of these layers are summarized in table 5.1.

Type	T_s (ºC)	H_2 (sccm)	SiH_4 (sccm)	PH_3 (sccm)	P (mbar)
intrinsic	100	-	2	-	3.5×10^{-3}
n-doped	200	28	2	0.04	8×10^{-2}

Table 5.1 Deposition conditions of the optimized films used in the heterojunction emitters. The wire temperature is 1600ºC in all cases.

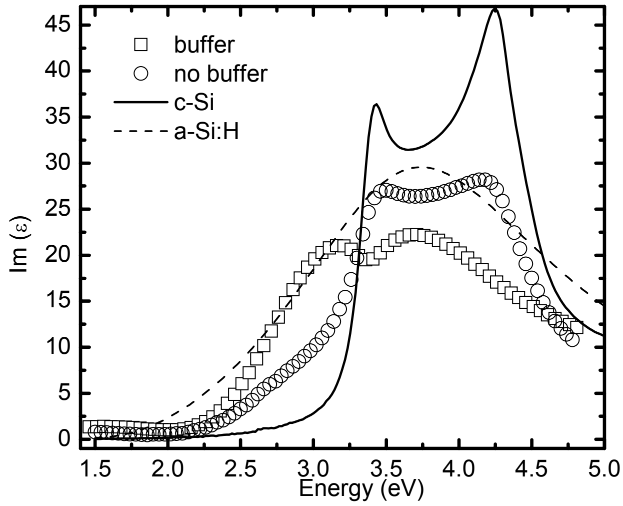

Figure 5.6: Comparison between the Im(ε) of the same (n)a-Si:H layer deposited onto a c-Si wafer with and without an a-Si:H buffer layer. The model of the c-Si and a-Si:H are also shown for comparison.

The corresponding ellipsometry measurements are shown in figure 5.6. Although the difference was only an extremely thin buffer layer, the curves were significantly different. The two crystalline features observed when the n-layer is deposited directly onto the crystalline wafer indicate partial epitaxy. By contrast, the introduction of the thin (i)a-Si:H buffer completely changes the microstructure leading to a basically amorphous layer.

These different microstructures have direct influence in the passivation properties. The epitaxial emitter reaches a V_{oc} of only 610 mV, while the amorphous one including the buffer layer achieves an excellent V_{oc} exceeding 680 mV (see Table 5.2). In the same sense, the NREL group has also reported that an abrupt heterojunction is preferred to a low temperature (thus partial and defective) epitaxial growth without significant increase in the band gap [Wang et al., 2006]. Figure 5.7 is a high resolution TEM image of an abrupt a-Si:H/c-Si heterojunction reported by the NREL group [Mahan, 2006]. In conclusion, results indicate that the beneficial effect of the buffer layer is twofold: a reduced interface defect density but also the promotion of a sharp heterojunction.

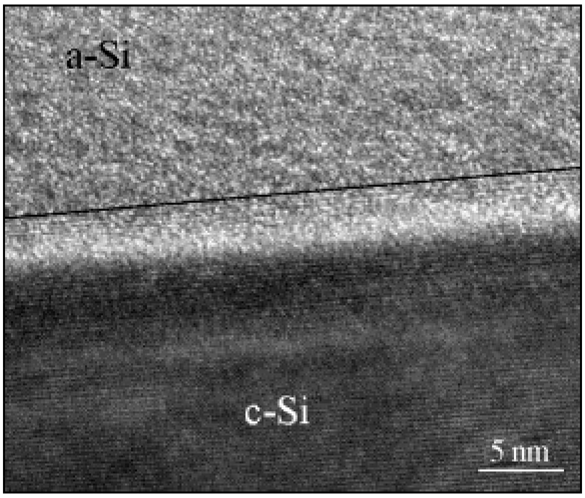

Figure 5.7: High resolution TEM image of the sharp NREL amorphous/crystalline interface. The line indicates the interface [Mahan, 2006].

Furthermore, the microstructure of the thin intrinsic layer also defines its passivation quality. The deposition conditions and, in particular, the thickness of the intrinsic layer are critical parameters [Veschetti et al., 2006]. A too thick buffer layer would increase the series resistance reducing drastically the final device performance. Since the deposition rate by HWCVD is relatively high in our case (3 Å/s), the deposition time (t_d) in the range of tens of seconds must be accurately controlled. In addition, the substrate temperature is also one of the most critical deposition parameters. As it is shown in table 5.2, a maximum in the τ_{eff} value (minimum S_{eff}) is obtained for T_s = 100ºC. The layers grown at room temperature (RT) showed no effect in the surface passivation which was even slightly worse than in the absence of buffer. Actually, the layer grown at room temperature evidenced a very high porosity at the interface. These results are similar at those obtained by [Wang et al., 2006].

Intrinsic layer	T_s (ºC)	SiH_4 (sccm)	P (mbar)	t_d (s)	Thickness (nm)	implicit-V_{oc} (V)	τ_{eff} (μs)
-	-	-	-	-	-	600	17
IRT	RT	2	3.5×10^{-3}	15	5	596	11
I100	100	2	3.5×10^{-3}	15	5	670	214
I200	200	2	3.5×10^{-3}	15	5	638	66
Ithin	100	2	3.5×10^{-3}	10	3	621	33
Ithick	100	2	3.5×10^{-3}	30	10	680	273

Table 5.2: Different intrinsic a-Si:H thin layers used in the heterojunction emitter and passivation quality measured by QSSPC. The 20 nm n-doped layer was the same in all cases with the deposition parameters in table 5.1.

In order to study the microstructure of the intrinsic a-Si:H material, a single 5 nm a-Si:H layer was deposited on c-Si without subsequent n-doped emitter. Figure 5.8 shows the ellipsometry data fitted following the Tauc-Lorenz model. The c-Si surface was cleaned and dipped into HF in order to remove the native oxide and assure good interface properties. In this particular case, the cleaning process was very critical due to the strong influence of the interface in the fit. As it is shown in the inset of figure 5.8, the band of the a-Si:H material deposited by HWCVD is significantly lower than for the standard a-Si:H model. This result can be related to the porosity of the layer which leads to a lower compactness (A value) in the model. Other groups have also referenced a higher porosity in HWCVD a-Si:H films compared to other deposition techniques [Liu et al., 2002]. The rest of parameters are quite similar to the standard material and similar properties are expected. Actually, the ellipsometry curve could be also fitted quite well by the standard a-Si:H material if a void fraction of 30% is considered.

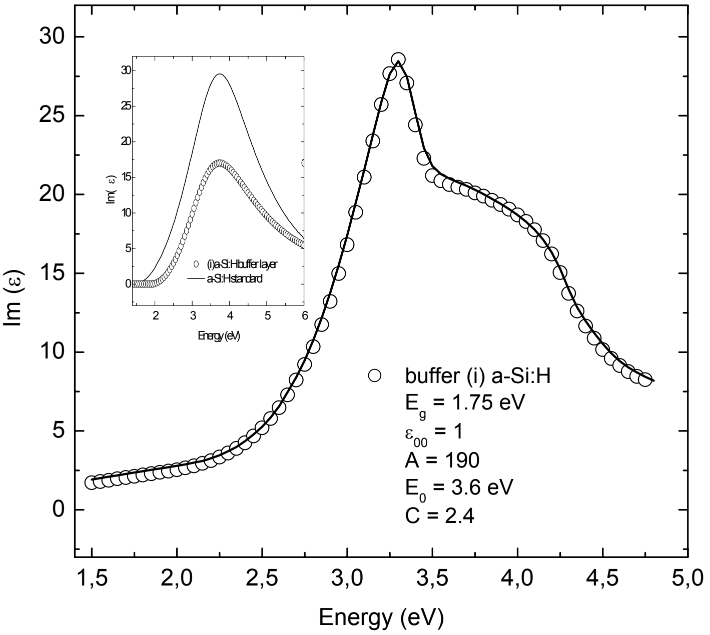

Figure 5.8: SE measurements (o) compared to the fitting (lines) of a 7 nm (i) a-Si:H. In the inset, the a-Si:H deposited by HWCVD used for the fitting compared to the standard a-Si:H. The parameters of the a-Si:H derived from the Tauc-Lorenz model are also shown.

5.1.4 Influence of pretreatments at the a-Si:H/c-Si interface

The interface optimization process also includes the possibility of surface pretreatments prior to the a-Si:H deposition, immediately after the standard wafer cleaning procedure. These treatments can be generally classified as chemical or physical. Among chemical treatments, buffered NH_4F [Froitzheim et al., 2002] and quinhydrone/methanol (QM) solutions [Page et al., 2003] result in hydrogen-terminated surfaces with good dangling bond passivation.

On the other hand, physical treatments depend on the specific technique used for a-Si:H deposition. For instance, PECVD treatments with CF_4 or SiF_4 plasmas in order to etch the c-Si surface have been reported with relative success [Losurdo et al., 2004, Tucci et al., 2002]. Also hydrogenation in a PECVD process has been demonstrated very effective to improve c-Si surface passivation [Martin et al., 2004], although the beneficial effect in a HWCVD process is less clear. The group at NREL has showed that H-treatments by HWCVD are beneficial only for very short times [Wang et al., 2006], while too long hydrogenation treatments decrease the passivation quality.

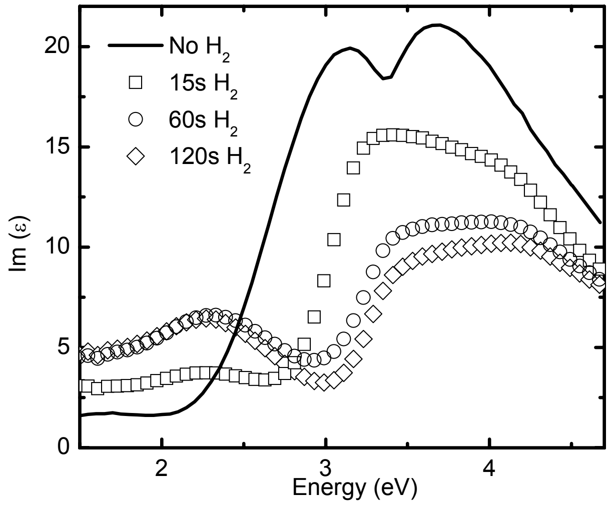

Figure 5.8: Imaginary part of the pseudodielectric function of four heteroemitter configuration with different HWCVD H-treatments before the a-Si:H layers deposition.

Figure 5.8 shows the SE measurements of four samples after different hydrogenation times. At first sight, clear changes are observed even with very short H-treatments compared to the untreated sample. The steady decrease in the measured Im(ε) value indicates a higher porosity in the layer. As it is shown in table 5.3, porosity increases at the interface and also in the main layer. In addition, differences in the microcrostructure of the layers are clearly observed. A microcrystalline fraction appears at the interface for H-treatments longer than 60 s, while it remains amorphous in the case of only 15 s.

SAMPLE	t_H	implicit-V_{oc}	τ_{eff}	interface			Layer		
				Xv	Xa	Xc	Xv	Xa	Xc
	s	mV	µs	%	%	%	%	%	%
noH	0	701	543	-	-	-	-	100	-
H15	15	590	10	-	100	-	25	63	12
H60	60	574	5	35	45	20	28	46	26
H120	120	572	4	40	42	18	30	45	25

Table 5.3: QSSPC and SE results obtained from the four samples with different H-treatment times.

The microcrystalline fraction at the interface and in the main layer due to H-treatments diminishes the band gap of the material. QSSPC data evidenced a lower passivation quality after H-treatments that can be related to the increasing porosity and band gap reduction. As a conclusion, we can affirm that H-treatments did not improve the final performance of our optimized heterojunction emitters.

5.1.5 Influence of post-treatments after a-Si:H deposition

Here we will consider treatments performed after deposition of the a-Si:H layers. We have studied two different possibilities: hydrogen-treatment inside the HWCVD chamber and thermal annealing in vacuum. Figure 5.9 shows the SE measurements comparing three different samples: the untreated heterojunction emitter, after 60 s of hydrogen-treatment and after thermal annealing for 30 min at 200ºC (the deposition temperature used for the doped layer). Very surprisingly a similar effect is observed for both treatments: a strong decrease in the Im(ε) value together with a change in the shape of the curve. The effective media model (table 5.4) reveals that the doped layer becomes highly porous with a void fraction over 80% whichever the applied post-treatment. By contrast, the thin buffer layer remains dense and amorphous in any case. The high increase in the porosity of the doped layer is combined with a clear degradation in the implicit V_{oc} of the device.

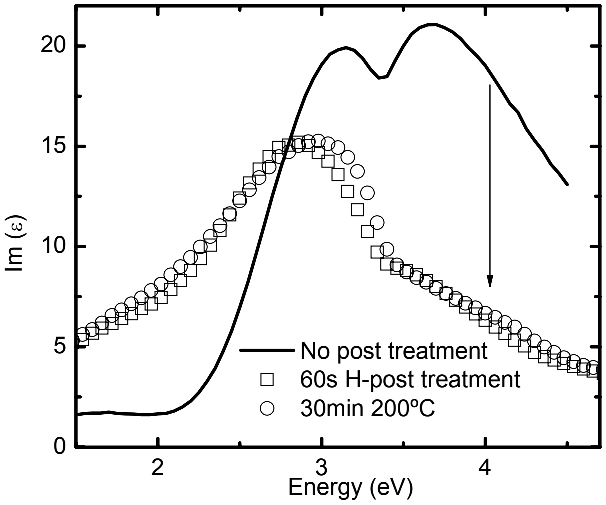

Figure 5.9: Imaginary part of the pseudodielectric function of the initial heterojunction emitter compared to different post -treatments: hydrogenation and thermal annealing.

Table 5.4 shows the models obtained by fitting the SE curves together with the QSSPC measurements for samples under study. As with the pre-treatments, we notice that post-treatments neither improved the quality of the emitter in our case.

					interface			layer		
	t_H	T	implicit-V_{oc}	τ_{eff}	Xv	Xa	Xc	Xv	Xa	Xc
SAMPLE	min	ºC	mV	µs	%	%	%	%	%	%
initial	0	-	701	543	-	-	-	-	100	-
H	1	-	585	8	-	100	-	80	15	5
anneal	30	200	571	4	-	100	-	90	5	5

Table 5.4: QSSPC and SE results obtained for the three samples under study.

5.1.6 Influence of the n-doped layer

In addition to the interface and intrinsic a-Si:H layer, the optimization of the heterojunction emitter requires also the study of the n-doped layer. After a comprehensive optimization of the deposition conditions (see chapter 4), the best performance in terms of implicit-V_{oc} was obtained with the conditions summarized in table 5.1. Then, the thickness of the n-doped layer was the last parameter to optimize.

Figure 5.10 shows the SE measurements of three heterojunction emitters with different n-doped layer thicknesses. The intrinsic a-Si:H buffer layer was 5nm thick in all cases. As it is shown in the enclosed table, differences in the microstructure can be clearly perceived. Porosity increases with the layer thickness together with the crystalline fraction of the surface (roughness). Both factors could cause the drop in the implicit V_{oc} value. Therefore, the best result was obtained for a thin 10 nm n-doped layer although usually better passivation is expected for thicker layers. Besides, the emitter thickness also affects the short-circuit current of the final device due to optical absorption in the n-doped layer. Internal Quantum Efficiency curves of complete solar cells with three different n-doped layer thicknesses are shown in figure 5.11. The lower response in the short wavelength range for thicker emitters reduces the solar cell performance in terms of J_{sc}.

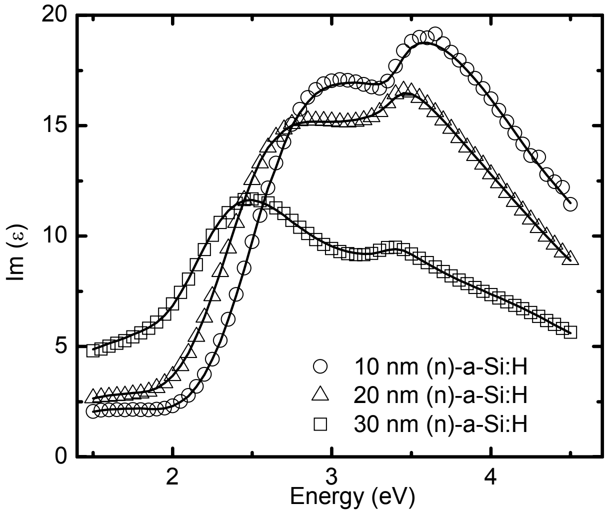

	10 nm				20nm				30nm			
model	thickness (nm)	Xa	Xc	Xv	thickness (nm)	Xa	Xc	Xv	thickness (nm)	Xa	Xc	Xv
roughness	3	78	6	16	5	24	25	51	12	18	26	56
layer	14.5	100	-	-	24	100	-		25.4	72	-	28
substrate	c-Si				c-Si				c-Si			
	implicit Voc = 704 mV				implicit Voc = 677 mV				implicit Voc = 663 mV			

Figure 5.10: Imaginary part of the pseudo dielectric function for three heterojunction emitters with different n-doped layer thicknesses. The lines correspond to fittings of the experimental data using the Bruggemann effective media approximation. The corresponding models are shown in the enclosed table.

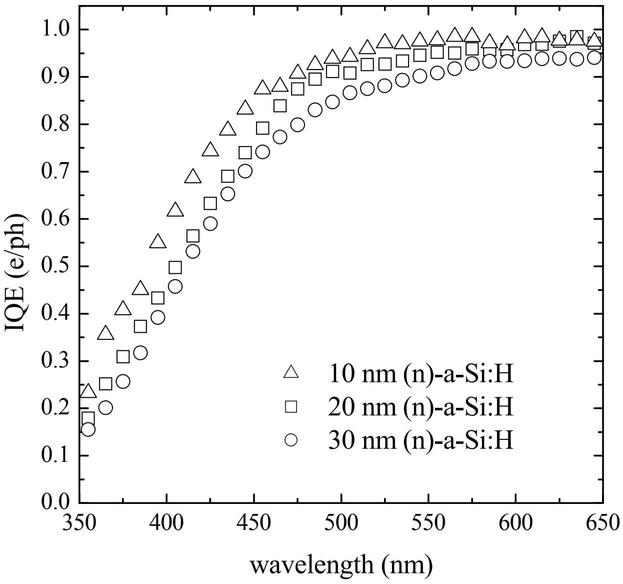

Figure 5.11 Internal Quantum Efficiency curves for solar cells fabricated with three different n-doped layer thicknesses.

5.2 Characterization of BSF contacts deposited by HWCVD on p-type wafers

The a-Si:H/c-Si heterojunction has been widely studied for a diode configuration (np or pn junction) but it is indeed difficult to find information concerning p^+p or n^+n junctions. These structures have gained much interest as low temperature back contacts alternative to the usual Al-BSF. In this work, we have centered the study in the p^+p configuration because the main objective was the fabrication of low temperature heterojunction solar cells on p-type wafers.

5.2.1 Band diagram of the (p^+)a-Si:H/(p)c-Si structure

The band diagram of the p^+p structure is shown in figure 5.12, considering either an a-Si:H (right) or a µc-Si:H BSF contact (left). A few differences can be mentioned between these two structures.

On the one hand, the higher band gap of a-Si:H with a larger conduction band offset (ΔE_C) results in a better mirror for the minority carrier (electrons). However, the valence band offset (ΔE_V) is also increased producing a large barrier for the majority carrier (holes) to flow through the back contact. In this case, the use of an intrinsic layer to improve interface passivation could limit the trap-assisted tunneling desired for a good conduction of majority carriers [Wang et al., 2004]. One possible approach to overcome this barrier can be the use of highly doped (p^+)a-Si:H layers with respect to the (p)c-Si wafer. Unfortunately, it is rather difficult to obtain good quality (p^+)a-Si:H layers with high doping levels by HWCVD [Soler, 2004]. Then, the wafer should not be too doped unless we can assure highly p-doped a-Si:H layers with good electronic properties.

On the other hand, the lower band gap of µc-Si:H layers ($E_g \approx 1.4$eV) results in a smaller ΔE_C and less effective electron mirror. However, the also smaller ΔE_V would favor the collection of holes at the back contact. Moreover, microcrystalline silicon is more easily doped to obtain higher conductivity values (see chapter 4). Then, µc-Si:H layers deserve special consideration for the optimization of low-temperature BSF contacts. Furthermore, interface passivation must be also taken into account whichever structure is used.

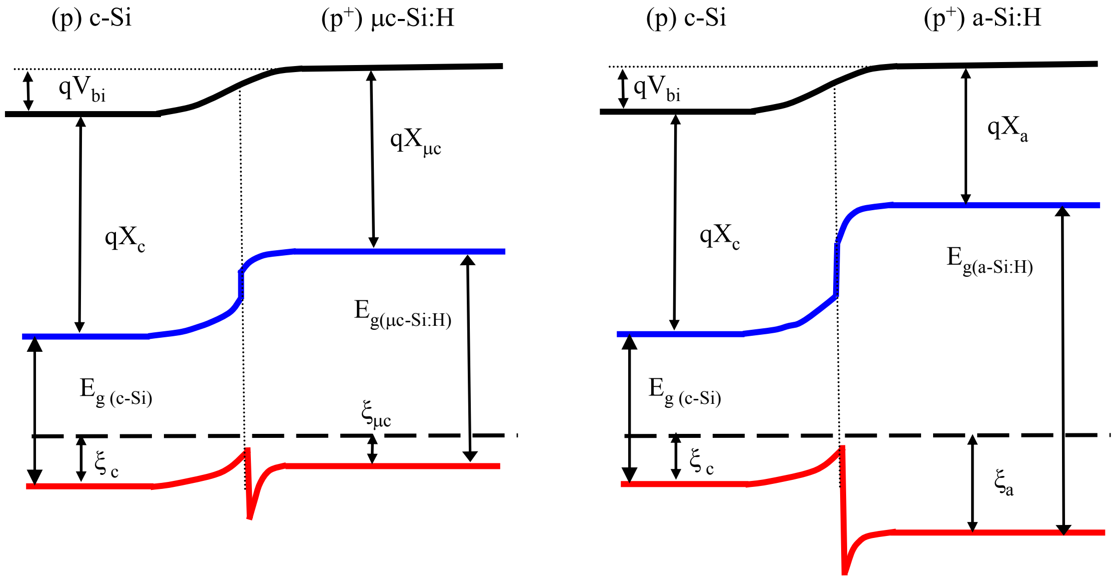

Figure 5.12: Band diagram of a (p$^+$)a-Si:H/(p)c-Si (right) and (p$^+$)μc-Si:H/(p)c-Si heterojunction (left).

The desired properties for the back contact can be summarized:

1. High doping level of the a-Si:H/μc-Si:H material
2. High doping level of the c-Si wafer (limited by the success in 1)
3. High band gap of the a-Si:H/μc-Si:H material
4. Low interface recombination velocity

In addition, these properties have to be compatible with technological aspects related to the deposition technique. In this work, the study of low temperature BSF contacts will be centered on the deposition of good quality p-doped layers by HWCVD. In order to achieve the desired microstructure and passivation properties we have comprehensively studied the influence of the deposition parameters. The effect of a thin intrinsic buffer layer is also carefully analyzed. However, it is important to remark that good precursors do not assure good BSF contacts, since carrier collection is actually not considered. The study of complete solar cells is part of the next chapter.

5.2.2 Optimization of the p-doped layer

As for the heterojunction emitter, we have considered the configuration with and without an intrinsic buffer layer. Firstly, we have studied the properties of p-doped layers deposited on c-Si substrates. Considering that it is much more difficult to achieve good electronic properties when doping with boron, the a-Si:H layers were extensively studied varying the different deposition parameters.

a) Influence of the diborane flow and filament temperature

One of the more critical parameters affecting the microstructure of the material is the diborane (B_2H_6) flow. On the one hand, it has been reported that diborane promotes amorphization of the layers [Voz et al., 2000]. The structural change due to boron incorporation is also accompanied by a change in the hydrogen bonding environment. It is also well known that the doping efficiency of boron in a-Si:H is quite low [Winer et al., 1990]. The doping efficiency is about 10% at low boron concentrations and falls off to only a fraction of percent as the boron concentration rises. Such a low doping efficiency is attributed to the belief that most boron atoms are incorporated into threefold coordinated sites where boron is inert or non-doping. This is in marked contrast to the situation for c-Si where all the incorporated boron atoms substitute for silicon atoms obtaining a virtually 100% doping efficiency. In addition, p-doping of a-Si:H layers is considerably less effective because of the filling of band tail and defect states.

On the other hand, the use of p^+p junctions for the back contact requires a low density of states at the interface, as well as an effective field-effect passivation. The band bending at the silicon surface caused by the electric field reduces the density of one carrier type at the interface (holes in this case), minimizing the recombination velocity. In such *high-low* junctions field effect passivation is achieved if we are able to deposit heavily p-doped a-Si:H layers, otherwise band bending would play a negative role in both carrier collection and interface passivation.

Type	T_s (ºC)	T_f (ºC)	H_2 (sccm)	SiH_4 (sccm)	B_2H_6 (sccm)	Pressure (mbar)
Plow	100	1600	2	1.5	variable	1×10^{-2}
Phigh	100	1750	2	1.5	variable	1×10^{-2}

Table 5.5: Deposition parameters of the p-doped a-Si:H films. We have considered separately two wire temperatures.

In Table 5.5 the deposition parameters of two series of p-doped films using different filament temperatures are shown. The filament temperature is a critical parameter because of its influence on the microstructure of the films. Many efforts have been done to control the filament temperature and to avoid eventual contamination of the films with Ta (or W) atoms [Villar, 2008]. The filament temperature can change the properties of the film either directly, by radiative heating of the growing surface (substrate temperature), or indirectly, by changing the radical composition in the gas phase. Higher filament temperatures enhance the generation of atomic hydrogen [Doyle et al., 1988], thus increasing the H flow to the film surface. Consequently, the increased surface concentration of hydrogen atoms enhances the surface rearrangement rate and improves the crystallinity of the film.

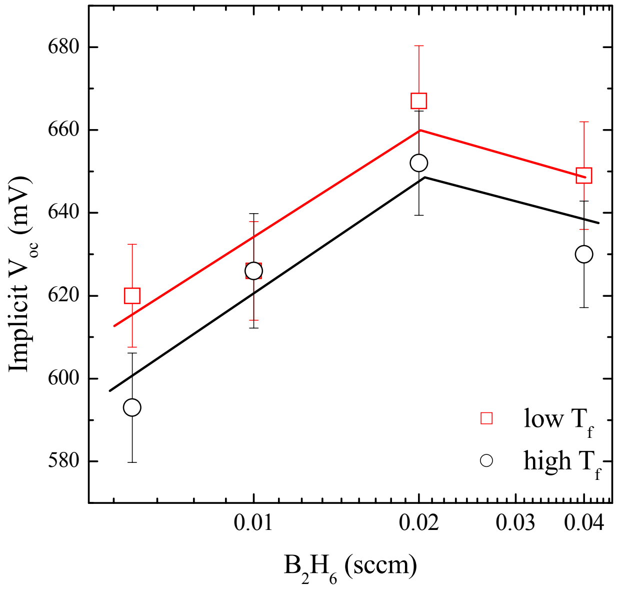

Figure 5.13: Implicit-V_{oc} values obtained by QSSPC as a function of the diborane flow for the two filament temperatures considered.

Figure 5.13 shows the implicit-V_{oc} values measured by QSSPC as a function of the diborane flow for the two filament temperatures considered. The maximum V_{oc} is obtained for a diborane flow of 0.02 sccm, which corresponds to a 1% dilution in silane. The behavior is similar for both series of films, increasing for lower boron concentrations and decreasing after an optimum value. In all cases, the best results were obtained for the lower filament temperature.

High Tf																				
MODEL		P0.6	Xa	Xc	Xv		P1	Xa	Xc	Xv		P2	Xa	Xc	Xv		P4	Xa	Xc	Xv
roughness		5nm	11	30	59		4nm	24	14	62		4nm	46	24	30		3nm	65	-	35
layer		21nm	78	22	-		33nm	95	5	-		36nm	100	-	-		33nm	100	-	-
interface		7nm	75	-	25		7nm	67	-	33		13nm	86	-	14		10nm	70	-	30
c-Si		c-Si					c-Si					c-Si					c-Si			
Low Tf																				
MODEL		P0.6	Xa	Xc	Xv		P1	Xa	Xc	Xv		P2	Xa	Xc	Xv		P4	Xa	Xc	Xv
roughness		5nm	48	12	40		6nm	48	10	42		4nm	58	-	42		5nm	60	-	40
layer		23nm	86	14	-		25nm	97	3	-		38nm	100	-	-		40nm	100	-	-
interface		6nm	55	-	45		7nm	89	-	11		17nm	91	-	9		16nm	90	-	10
c-Si		c-Si					c-Si					c-Si					c-Si			

Table 5.6: Effective media models deduced from ellipsometry measurements for all the samples shown in figure 5.13.

The effective media models deduced from ellipsometry measurements are shown for all the samples under study in table 5.6. Regarding to the microstructure of the films, higher crystalline fractions were obtained in the high T_f series. Thus, better passivation was obtained for the more amorphous layers of the low T_f series. It is also observed that the crystallinity is reduced when increasing the doping concentration, whichever the filament temperature. Moreover, in both cases the interface porosity decreases to its minimum value when doping with 1% concentration. In particular, the void fraction is below 10% at the interface for the low filament temperature. The worse passivation of the most doped layers also agrees with the increased interface porosity.

Besides, the microstructure of the layers, field-effect passivation must be also considered to explain the behavior of the implicit-V_{oc}. Since field-effect passivation should increase with the doping level, better results are expected for the more doped layers. However, diborane also promotes amorphisation of the layers and a consequent reduction in the doping efficiency. This effect explains the lower V_{oc} of the most doped layer in figure 5.12. Hence, three main factors affect the implicit-V_{oc} obtained by QSSPC:

1. Surface passivation related to the interface porosity
2. Band configuration related to the crystalline fraction
3. Field-effect passivation related to the doping level

b) *Influence of the silane flow*

In the HWCVD technique the SiH_4 flow has an important effect on the deposition rate and also the microstructure of the layers. If the silane flow is too low, the close environment of the filament will become depleted of silane. In this case the dissociation process is limited by the supply of silane to the filament and thus the deposition rate increases with the silane flow. Above a certain gas flow the dissociation rate at the filament surface will become the limiting factor and the deposition rate will not increase anymore [Feenstra et al., 1999]. Table 5.7 summarizes the deposition conditions of two pairs of layers with different silane flows and doping levels.

Type	Ts (ºC)	Tf (ºC)	H_2 (sccm)	SiH_4 (sccm)	B_2H_6 (sccm)	Press (mbar)
P2A	100	1750	2	2	0.02	2×10^{-2}
P2B	100	1750	4	2	0.04	2×10^{-2}
P1.5A	100	1750	2	1.5	0.02	2×10^{-2}
P1.5B	100	1750	4	1.5	0.04	2×10^{-2}

Table 5.7: Deposition conditions for the p-doped layers under study.

The SE measurements of these samples are shown in figure 5.14. The samples deposited with 1.5 sccm of SiH_4 evidenced an amorphous microstructure, while those with 2 sccm of SiH_4 showed the presence of a crystalline fraction. Table 5.8 summarizes the models deduced by fitting the SE curves and the implicit-V_{oc} values measured by QSSPC for the samples under study. It has been reported for films deposited by HWCVD that the hydrogen bonding configuration shifts from mono- to di-hydrogen when the silane flow is increased. The di-hydrogen configuration is usually related to a higher density of voids and also bigger void sizes [Mahan et al., 1991]. In this sense, the interface porosities were higher for the samples with 2 sccm of silane. Therefore, the implicit-V_{oc} values were quite lower for the samples with a higher silane flow. In addition, the significant crystalline fractions in the main layer (> 60%) point to a lower band gap for these samples. No epitaxy is observed probably because the porous interface blocks the crystalline growth. Thus, the crystalline fraction corresponds to small grains into the a-Si:H matrix. The doping level did not evidence an important effect neither on the microstructure nor on the passivation properties. On the other hand, the samples deposited with 1.5 sccm of silane were denser and basically amorphous. These samples evidenced much better passivation properties compared to the ones deposited with higher silane flow. In this case, the variation in the V_{oc} values with the doping level could be attributed to the different interface porosities.

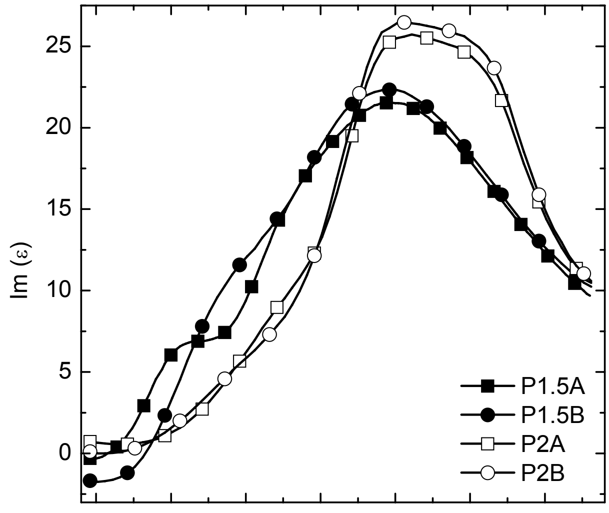

Figure 5.14: SE Measurements of the p-doped layers under study.

MODEL	P1.5A	Xa	Xc	Xv	P1.5B	Xa	Xc	Xv	P2A	Xa	Xc	Xv	P2A	Xa	Xc	Xv
roughness	4nm	46	24	30	3nm	65	-	35	4nm	25	48	26	3nm	32	43	25
layer	36nm	100	-	-	33nm	100	-	-	31nm	35	65	-	36nm	34	66	-
interface	13nm	86	-	14	10nm	70	-	30	3nm	65	-	35	4nm	60	-	40
SUBSTRATE	c-Si				c-Si				c-Si				c-Si			
implicit-V_{oc}	667 mV				649 mV				615 mV				612 mV			

Table 5.8: Fittings from the ellipsometry measurements for all the samples plotted in 5.14.

c) Influence of H_2 dilution

The microcrystalline films previously studied showed only fair passivation properties with implicit-V_{oc} values only slightly over 610 mV. Although amorphous layers allowed much better results, the carrier collection in complete solar cells has to be confirmed (next chapter). Therefore, in this section we study different deposition conditions in order to obtain highly conductive microcrystalline p-doped layers with better passivation quality. Now, the H-dilution is considered since it is well known that this parameter plays an important role in the microstructure of the film [Niikura et al., 2000]. Table 5.9 shows the deposition conditions of a film grown with a high hydrogen dilution.

Type	T_s	T_f	H_2	SiH_4	B_2H_6	Press
	(ºC)	(ºC)	(sccm)	(sccm)	(sccm)	(mbar)
PH	100	1750	100	4	0.02	3×10^{-2}

Table 5.9: Deposition conditions for a film grown with a high H-dilution.

In this case, the SE measurement of the layer evidenced a clearly crystalline microstructure (figure 5.15). In particular, the imaginary part of the pseudo dielectric function resembles the model of a big grain μc-Si:H material. The effective media model deduced by fitting the SE curve is shown in table 5.10.

The lower Im<ε> value of the sample PH compared to the models can be attributed to the high void fraction on the surface (roughness), which strongly diminishes the high energy peak. Since the crystalline fraction is actually formed by a mixture of small and big grain materials, the shape of the curve is also relatively smoothed. The implicit – Voc measured was lower than 600 mV. This low value is due to the bad interface between the c-Si and the layer created by a bad quality epitaxial growth.

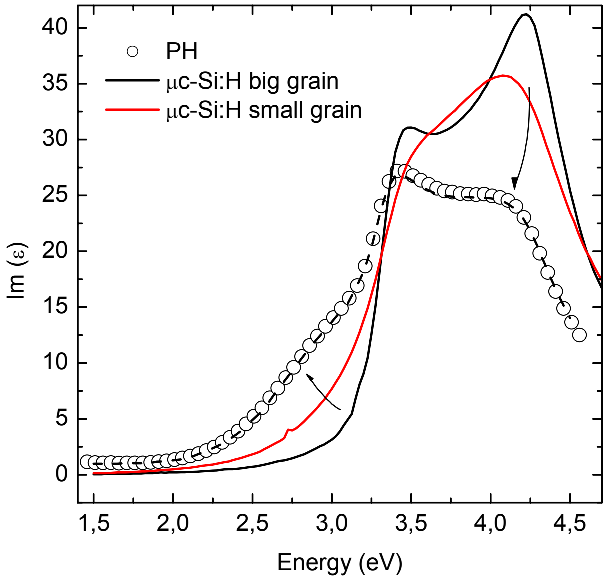

Figure 5.15: SE Measurements of the sample compared with the μc-Si:H models. The dashed line corresponds to the fitting of the experimental curve.

MODEL	P2	Xa	Xc	Xv
roughness	4nm	-	58	42
layer	24nm	-	100	-
interface	22nm	-	96	4
SUBSTRATE	c-Si			

Table 5.10: Fitting of the sample PH following the standard model.

5.2.3 Influence of the intrinsic buffer layer on the band diagram

As discussed in section 5.1.3 for heterojunction emitters, an effective way for obtaining abrupt heterojunctions is the intercalation of a thin intrinsic amorphous layer. Then, the back contact will consist in the stack of the buffer followed by the p-doped layer. Here, we comprehensively study the influence of the intrinsic buffer on the microstructure and properties of the deposited back contact. First, we will discuss the effect of the buffer layer on the band diagram.

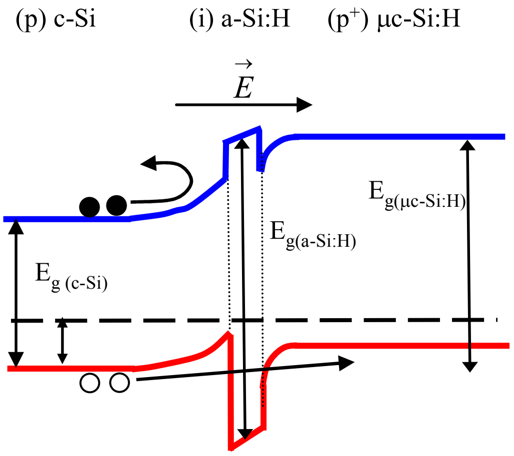

Figure 5.16: Band diagram of a (p)μc-Si:H/(i)a-Si:H/(p)c-Si back contact. The structure for an a-Si:H p-layer would be similar to the one showed in figure 5.12.

Figure 5.16 shows the band diagram of a (p)μc-Si:H/(i)a-Si:H/(p)c-Si structure. The wider band gap of the buffer layer creates a discontinuity in the conduction band (ΔE_c) acting as a barrier that prevents photogenerated electrons from diffusing into the (p)μc-Si:H. This barrier is stronger than in the simple μc-Si:H/c-Si heterojunction configuration. As a result, recombination losses in the (p)μc-Si:H layer are strongly reduced which leads to a higher V_{oc} value. The discontinuity at the valence band should not limit the carrier collection at the (p)μc-Si:H contact since holes can traverse the barrier by tunneling. Obviously, we should also consider the defect density at the a-Si:H/c-Si that has a strong effect on the recombination velocity. In the case of an a-Si:H instead of μc-Si:H p-layer, the band diagram remains basically unchanged with the introduction of the intrinsic a-Si:H buffer [Van Cleef et al., 1997]. However, hole collection at the back contact could limit the performance of complete solar cells if the doping level of the (p)a-Si:H is not high enough.

5.2.4 Optimization of the (p)a-Si:H/(i)a-Si:H stack on (p)c-Si

The intrinsic a-Si:H buffer and the p-doped layer are deposited in different chambers of the HWCVD set-up. The substrate is introduced into the chamber devoted to intrinsic material where the thin (i)a-SiH buffer is grown. Then, the sample is moved into the chamber for doped material where the p-layer is deposited without breaking the vacuum. The deposition conditions of the different layers were summarized in table 5.1 (intrinsic) and table 5.5 (p-doped layers).

a) Influence of the diborane flow and filament temperature

All the (p)a-Si:H/(i)a-Si:H/(p)c-Si stacks were deposited after their corresponding (p)a-Si:H/(p)c-Si simple heterojunctions to avoid mismatches in the diborane flow or variations in the wire that could lead to misinterpretation of the results.

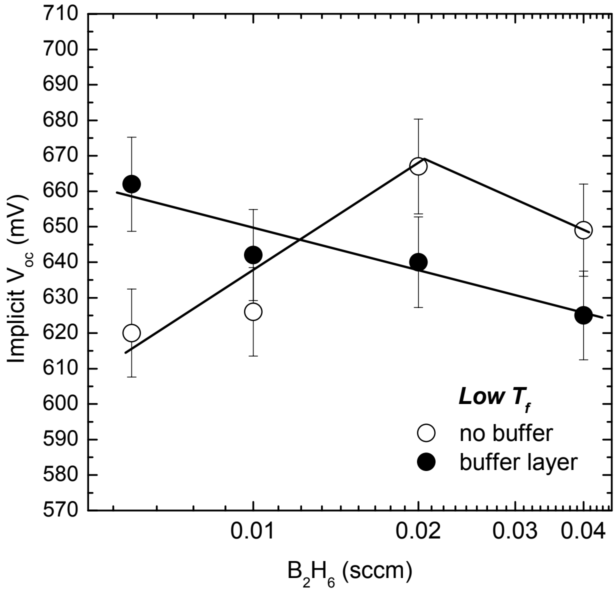

Figure 5.17: Implicit-Voc values measured by QSSPC for a series of diborane concentrations at low filament temperature. The results obtained with buffer layer (●) are compared to those obtained for simple heterojunctions (○).

Figure 5.17 shows the implicit-V_{oc} values for a doping series of samples deposited at low filament temperature. Significant differences arise from the comparison of the samples with or without buffer layer. The optimum diborane flow around 0.02 sccm for simple heterojunctions was already discussed in section 5.2.2. By contrast, a steady decrease of V_{oc} with the doping level is observed for the samples with buffer layer. The effective media models for the samples in the extremes of the doping series are summarized in table 5.11. The buffer layer is not considered individually in the fitting procedure but included in the interface layer. In the series with buffer layer we observe that the thickness and porosity of the interface increase with the doping level, which accounts for the progressively lower V_{oc}. All the layers deposited with buffer are basically amorphous with only a little crystalline fraction near the surface (roughness).

Concerning the layers obtained without buffer layer, the crystalline fraction observed at low doping levels disappears for higher diborane flows. Then, the higher band gap and less porous interface improve the passivation quality and allow higher V_{oc} values. An important conclusion is that for high doping levels abrupt heterojunctions can be obtained without buffer layer. This result is due to the amorphisation effect of high diborane flows on the growing layer.

On the other hand, QSSPC results for a high filament temperature are shown in figure 5.18. The performance was better with buffer layer in the whole doping range, with an implicit-V_{oc} close to 690 mV for a 0.01 sccm diborane flow. This is the best result we have ever obtained for BSF contacts obtained by HWCVD. The buffer layer seems to promote an amorphous and less porous interface followed by a layer of high crystalline fraction (see Table 5.12). This structure is similar to the band diagram of the ideal case presented in figure 5.16, combining an abrupt heterojunction of good passivation quality with the higher doping efficiency of microcrystalline layers. The behavior is similar for higher doping levels, when the amorphization effect of diborane makes not necessary the buffer layer.

MODEL
Roughness
Layer
Interface
SUBSTRATE

IP0.6	Xa	Xc	Xv
6nm	54	17	29
40nm	100	-	-
16nm	87	-	13
c-Si			

P0.6	Xa	Xc	Xv
5nm	48	12	40
23nm	86	14	-
6nm	55	-	45
c-Si			

MODEL
Roughness
Layer
Interface
SUBSTRATE

IP4	Xa	Xc	Xv
7nm	65	10	25
21nm	100	-	-
35nm	83	-	17
c-Si			

P4	Xa	Xc	Xv
5nm	60	-	40
40nm	100	-	-
16nm	90	-	10
c-Si			

Table 5.11: Effective media models for the first and last samples (least and most doped, respectively) of the doping series in figure 5.17.

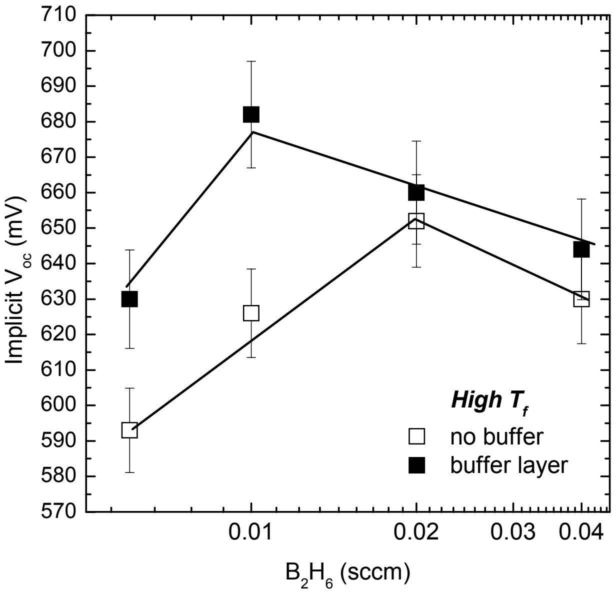

Figure 5.18: Implicit-V_{oc} values measured by QSSPC for a doping series obtained at high filament temperature. The results obtained with (■) and without buffer layer (□) are compared.

The best V_{oc} values obtained for BSF contacts are still lower that those obtained for optimized heterojunction emitters (section 5.1). Hence, the back contact would in principle limit the V_{oc} of bifacial heterojunctions. It is difficult to obtain compact p-doped layers by HWCVD as boron-hydrogen complexes create a heterogeneous interface. Even when we introduce the buffer layer, there is a residual porosity in the interface due to hydrogen diffusion and chemical etching during the growth of the p-doped layer. Nevertheless, encouraging results with implicit-V_{oc} values exceeding 680 mV were achieved. This would surpass standard high temperature Al-BSF contacts in a fully low temperature process. However, it is necessary to assure that carrier collection is good also at the back contact in complete solar cells.

MODEL	IP1	Xa	Xc	Xv	P1	Xa	Xc	Xv
roughness	27nm	31	36	33	4nm	24	14	62
layer	11nm	25	75	-	33nm	95	5	-
interface	35nm	90	-	10	7nm	67	-	33
SUBSTRATE	c-Si				c-Si			

Table 5.12: Effective media models deduced from SE measurements for the structures obtained with a diborane flow of 1 sccm.

Chapter 6: Fabrication technologies of heterojunction solar cells

Desde que el hombre existe ha habido música, pero también
los animales, los átomos y las estrellas hacen música.
K. Stockhausen
¿porqué no las HIT?

This chapter deals with the technological issues related to the fabrication of complete heterojunction solar cells. Aspects such as the optimization of the antireflection coating, active area definition and the metallic grid electrode are reviewed in detail. The characteristics of the best heterojunction solar cells fabricated during this thesis will be also presented and discussed.

6.1. Optimization of the front TCO

Transparent conductive oxide (TCO) layers, which are both transparent in the visible range and electrically conducting, have been widely studied for over 25 years [Nath et al., 1980], [Ray et al., 1983]. Such particular properties have led to extensive applications in optoelectronic devices. Among other alternatives, tin-doped indium oxide, generally referred as indium-tin-oxide (ITO), and aluminium-doped zinc oxide (AZO) are usual TCO layers. The high n-type conductivity of these films (> 10^3 Ω^{-1}

cm^{-1}) results from a stoichiometric deviation (oxygen vacancies) and doping with excess metal ions [Chen et al., 2000]. Although for thin film solar cells AZO is a very common TCO, in a-Si:H/c-Si heterojunction solar cells most groups use ITO for the front electrode. The reasons are the good properties in terms of conductivity and transmittance, together with its adequate work function [Centurioni et al., 2003], as we will discuss later.

In this work, we have optimized ITO layers obtained by RF sputtering magnetron in a system with base pressure of 10^{-5} mbar. These layers are deposited on the emitter and also on the BSF contact of bifacial solar cells. The substrate is located at a distance of 5 cm from the sintered target, which has an In_2O_3:SnO_2 composition of 90:10wt.%. An Argon flow of 10 sccm was used for the sputtering process at a pressure of 0.5 Pa. Slight differences in the properties of the films were observed in the range 0.4-0.7 Pa.

6.1.1 Influence of the RF power

A series of samples varying the RF power from 30 to 150 W have been obtained at room temperature. In figure 6.1, the resistivity and refraction index measured for these samples are presented. As it is clearly observed, the resistivity of the films decreases for high power values, whereas the refraction index behaves in the opposite direction. The optimal values (of $\rho \approx 4\times10^{-4}$ Ωcm) are obtained for high power values, but the optimum refraction index $n \approx 2$ is obtained in the 50 - 100 W range. Hence, the optimum power considering both the resistivity and refraction index was 100 W which is the value used from now in all the studied samples.

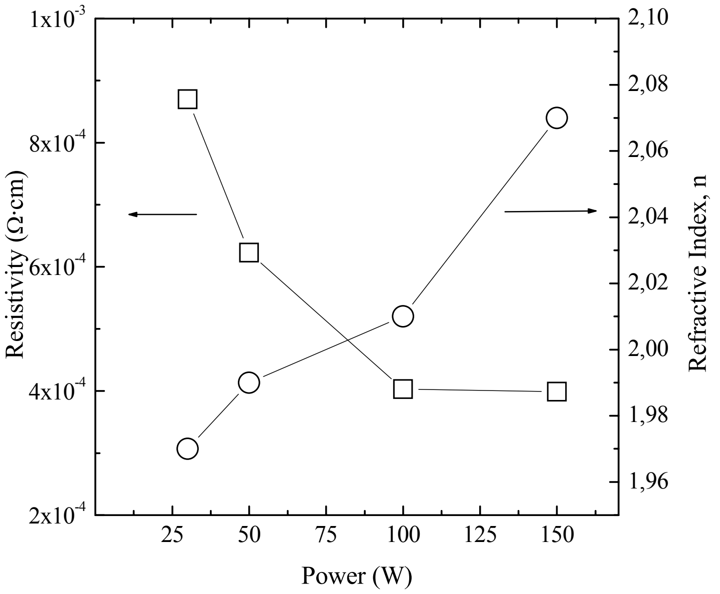

Figure 6.1: Resistivity measured by four-probes and refraction index measured by ellipsometry for samples deposited by sputtering with different RF power.

6.1.2 Optimum film thickness

In order to assure the maximum quantity of photons arriving to the active layer, one critical parameter to optimize is the thickness of the ITO layer. The minimum in the reflectance spectrum should be located in the region of maximum solar irradiance (500 - 650 nm). We have measured the reflectance spectra for layers of different thicknesses deposited using the optimized conditions described before. These measurements are shown in figure 6.2, where we can observe that thinner layers adequate better to the solar spectra. However, it must be also considered that too thin layers would also increase the series resistance of the device. Hence, layers around 80 nm could be the best choice to fulfill both optical and electrical requirements with a sheet resistance around 50 **Ω**.

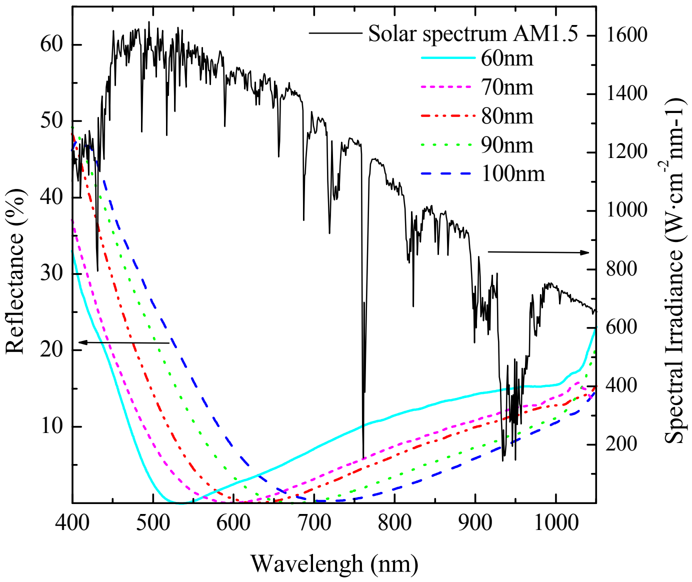

Figure 6.2: Reflectance of ITO layers of different thickness deposited on c-Si compared with the AM1.5 Solar Spectrum.

6.1.3 The substrate temperature

We have also deposited ITO layers increasing the substrate temperature to 260ºC, which is over the reported crystallization temperature (250ºC). In table 6.1 the electrical and optical properties of ITO layers deposited at room temperature (RT) and 260ºC are compared. All the studied layers were 80 nm thick except for transmittance measurements where we used 500 nm layers to obtain interference fringes [Swanepoel, 1983]. The refractive indexes measured by optical transmittance were slightly lower than those obtained by ellipsometry. There are also small differences in the resistivity values measured either with four probes or by the Hall Effect. However, there is good correlation and the RT sample showed better electrical properties with higher free carrier concentration and mobility. In a degenerated semiconductor as ITO the Fermi level is above the bottom of the conduction band. Hence, the apparent band gap increases with the carrier concentration, which is known as the Burstein –Moss effect [Burstein, 1954].

	four points		ellipsometry	Hall			transmittance	
	ρ	R_s	n	ρ	n_d	μ	n	E_g
	Ωcm	$\Omega_\square$		Ωcm	cm^{-3}	$cm^2\,V^{-1}\,s^{-1}$		eV
RT	4.30×10^{-4}	53.75	2.01	5.1×10^{-4}	4.17×10^{20}	29.1	1.98	3.52
260ºC	6×10^{-4}	75	1.92	6.7×10^{-4}	3.65×10^{20}	25.4	1.86	3.47

Table 6.1: Summary of electrical and optical properties of ITO. The two samples studied were deposited at room temperature and at 260ºC. The measurement methods are: (i) four points, (ii) ellipsometry, (iii) Hall, (iv) transmittance. Layers' thicknesses: 80 nm, except for the transmittance measurements (500 nm).

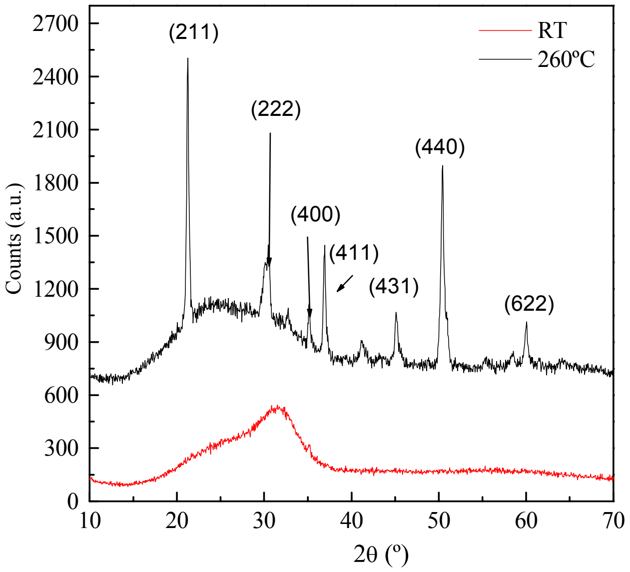

Figure 6.3: XRD Measurements for the ITO samples deposited at room temperature and at 260ºC.

Concerning microstructural properties, figure 6.3 compares the X-ray diffraction patterns of ITO layers deposited at room temperature and 260ºC. The layer deposited at room temperature was amorphous with no representative crystalline peaks. The feature observed near 30º can be attributed to a broadened SnO_2 peak (111) occurring at 31.452º [El Akkad et al., 2000]. The noticeable Sn content is directly related to the concentration of donor impurities. A donor centre in ITO can be produced by oxygen vacancies [Karasawa et al., 1993] or by Sn atoms incorporated as Sn^{4+} in substitutional sites for In, leading to the creation of Sn_{In} centres [Terzini et al., 2000]. Then, the high free carrier concentration in the RT layer (table 6.1) agrees with the presence of Sn_{In} revealed by the XRD spectrum.

On the other hand, the ITO layer deposited at 260ºC presents an evident crystalline microstructure with the main peaks at 211, 222, 400, 411, 440, and 622 [Terzini et al., 2000]. A significant parameter is the ratio between the I(222) and I(400) peak intensities, which determines the orientation of the grains. In our case, preferential orientation (222) leads to a good crystalline structure with satisfactory optical and electrical properties. In this case, no evidence of any SnO_2 peak was observed. The lower Sn content of these samples eliminates part of the Sn_{In} centres formed at room temperature, resulting in a slightly reduced free carrier density (table 6.1).

As a conclusion, the growing process over the crystallization temperature leads to a totally different microstructure. However, the optical and electrical properties were similar. There is no improvement by increasing the substrate temperature. Considering that a-Si:H layers are typically deposited below the 200ºC threshold, processes below 200ºC are desirable. Therefore, all the ITO layers for heterojunction solar cells were deposited at room temperature. Post-deposition annealing of ITO layers has been proposed with good results [Damon Lacoste, 2007], but in our case the restriction of 200ºC for not degrading a-Si:H layers did not allow any beneficial effect. It has been shown [Morikawa et al., 2000] that the ITO resistivity increases with temperature for values below 120ºC, little changes are observed between 120 and 180ºC. Finally, fast crystallization of the material is observed over 250ºC.

6.1.4 The oxygen partial pressure

Among different proposals found in the literature to improve the quality of ITO layers, many of them are focused on varying the oxygen content. Oxidizing or reducing atmospheres during deposition are expected to change the concentration of oxygen vacancies and consequently the carrier density. Thus, this parameter strongly influences the optical and electrical properties of the material [Zebaze Kana et al., 2006], [Nisha et al., 2005], [Cruz et al., 2004]. The oxygen content can be modified by introducing oxygen into the chamber during the sputtering process. Figure 6.4 shows a series of ITO layers deposited varying the oxygen partial pressure. As it can be observed, there is a dramatic increase in the resistivity for pressures over 2×10^{-5} mbar together with a significant variation of the refractive index. A similar behaviour has been reported in the literature [Boycheva et al., 2007].

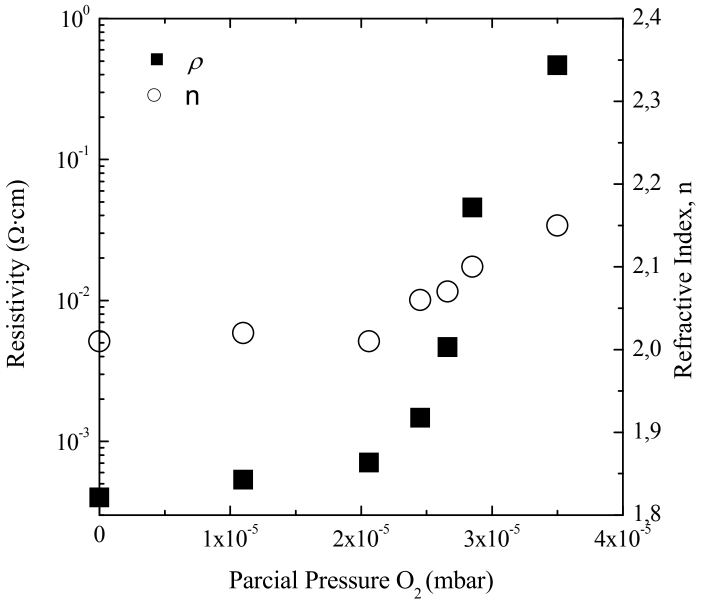

Figure 6.4: Resistivity and refraction index measured by four points and ellipsometry respectively for different oxygen partial pressures.

Furthermore, the oxygen content has also an important influence in the work function of the material. It has been proposed that in heterojunction solar cells the built-in potential cannot be merely defined by Fermi levels at the emitter and base, but it is also influenced by the work function of the TCO [Centurioni et al., 2003]. In the literature the reported ITO work function varies from 4.3 to 5.1 eV depending on the stoichiometry [Sugiyama et al., 2000], [Kim et al., 2000]. In principle, a high work function is preferred for p-doped a-Si:H layers (emitter on n-type c-Si) and a low value for n-doped layers (on p-type c-Si). The determination of the work function is not simple, the relatively complex Ultraviolet Photoemission Spectroscopy (UPS) and Kelvin Probe techniques have been used in the literature [Kim et al., 2000], [Tadayyon et al., 2004], [Schlaf et al., 2001]. However, it is also possible to obtain information from the built-in potential (V_{bi}) of the rectifying junctions formed by depositing ITO layers on n-type c-Si substrates. As it is shown in the band diagram of figure 6.5, the ITO work function can be calculated according to:

$$\Phi_{ITO} = \chi_{c-Si} + qV_{bi} + E_c - E_F \qquad 6.1$$

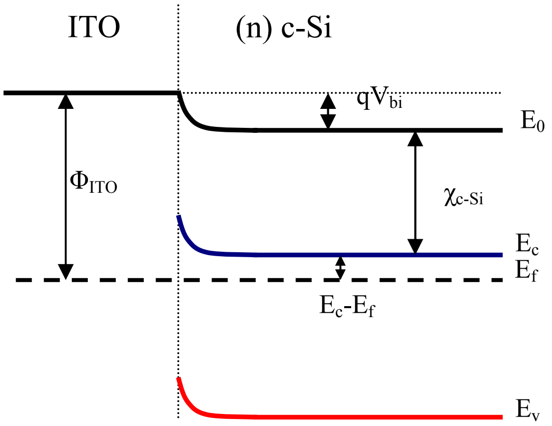

Figure 6.5: Band diagram of the ITO/(n)c-Si Schottky diodes.

where χ_{c-Si} is the electron affinity of c-Si (4.03 eV), the distance E_c-E_f is determined by the wafer doping and V_{bi} can be obtained from capacitance-voltage measurements [Kobayashi et al., 1991]. At high sweeping frequencies and in reverse polarization the measured capacity is dominated by the transition capacity (C_T), which is given by the following equation:

$$C_T = \frac{\varepsilon A}{\sqrt{\frac{2\varepsilon}{qN_D}(-V_{bi}+V+kT/q)}} \qquad 6.2$$

where N_D is the donor concentration of the wafer, A the area of the device and ε the dielectric constant of silicon. As it is well known, the $1/C^2$ vs. V plot gives a linear behaviour where the intercept at the voltage axis gives the V_{bi} value.

$$1/C^2 = \frac{2}{qN_D\varepsilon A^2}(-V_{bi}+V+kT/q) \qquad 6.3$$

Then, the work function of the ITO layer can be finally calculated using equation 6.1. Figure 6.6 shows the Φ_{ITO} values obtained for a series of ITO layers deposited with a different oxygen partial pressure. The same values were obtained within a 1% error for n-type c-Si wafers of different doping levels, which assures the validity of this method.

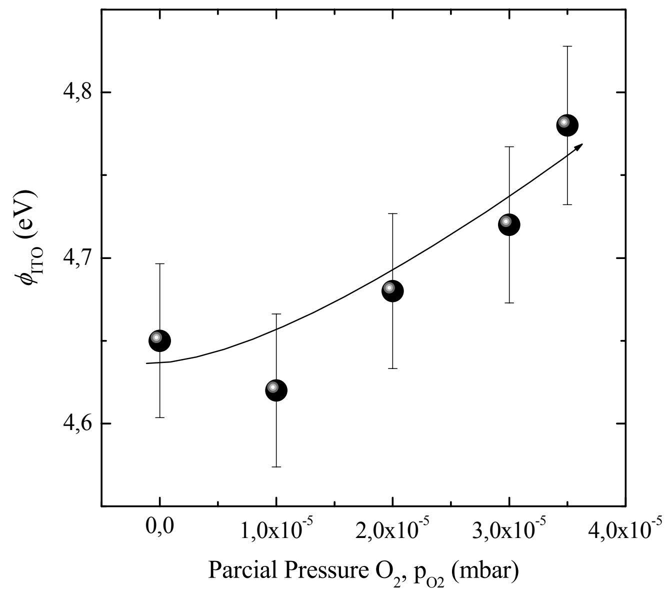

Figure 6.6: ITO work function vs. Oxygen partial pressure.

As it can be observed, the ITO work function increases with the oxygen content in the chamber. A similar result was also obtained for ITO samples deposited at 260ºC. The ITO work function around 4.65 eV at low P_{O2} values could be adequate for n-doped a-Si:H layers, but higher values would be desirable for p-doped layers. Although increasing the oxygen content indeed leads to higher Φ_{ITO} values, the higher resistivity of these layers (figure 6.4) is an important drawback for their incorporation in solar cells. An interesting alternative proposed in the literature [Tucci et al., 2004] considers the introduction of an extremely thin metallic film between the a-Si:H and ITO layers with an adequate work function to reduce or eliminate the Schottky barrier.

6.2 Final technological steps

In this section we will discuss final technological steps. The following steps: (i) active area definition, (ii) isolation and (iii) metallization; are of critical importance to the final performance of the solar cell. The contact quality between the metallic grid and the TCO, series and parallel parasitic resistances and perimeter recombination can drastically reduce the conversion efficiency of the device. Optical losses due to shadowing by the metallic grid must be also taken into account.

6.2.1 Active Area Definition

Perimeter losses are mainly due to recombination at the non-passivated cut edges of solar cell. These losses affect directly the open-circuit voltage, though the short-circuit current and fill factor can be also reduced. Perimeter recombination also degrades the efficiency of solar cells embedded in the wafer. This is due to the diffusion of minority carriers into the non-illuminated wafer regions outside the cell area [Schumacher, 2000].

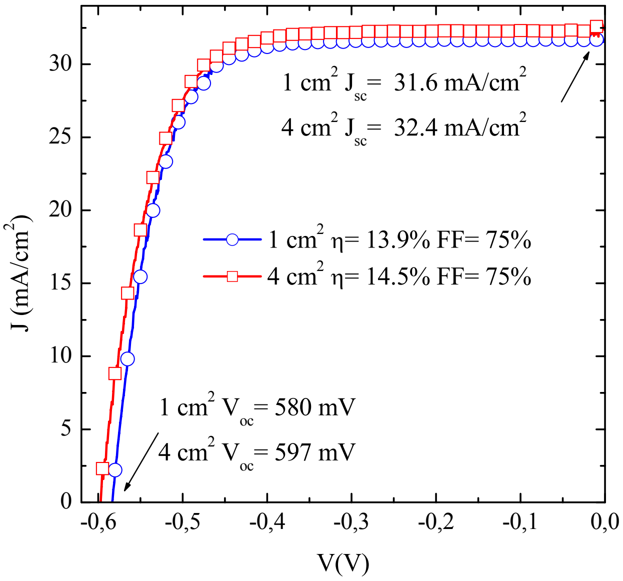

Figure 6.7: JV measurements at AM1.5 irradiance for two solar cells with different active area.

The area/perimeter ratio should be as high as possible to reduce the influence of the perimeter in the solar cell efficiency [Hermle et al., 2003]. In figure 6.7, the JV curves measured at AM1.5 for two solar cells of different active areas are shown. Although the FF is the same for both devices, the J_{sc} and V_{oc} values decrease for the smaller device. Consequently, the final conversion efficiency is also reduced 0.6%.

However, several technological problems arise when increasing the area of the device. First, it is more complicated to obtain thin and uniform a-Si:H layers, especially in laboratory deposition systems. This was the situation for the HWCVD system used in this thesis with a maximum deposition area of 4×4 cm^2. Second, only one big solar cell can be obtained in each deposit, whereas several smaller devices could be distributed in the same substrate to compare other technological factors. Considering this technological limitations, most of the studied devices were of 1 cm^2 although better results could be obtained for 4 cm^2.

6.2.2 Dry-etching optimization

Isolation of the solar cell directly reduces lateral leakage currents and the parasitic parallel resistance. After comparing wet-chemical and dry-plasma etchings, we have found the second one cleaner and much easier to control. The optimized etching parameters are summarized in table 6.2.

	Pressure (mbar)	CF_4/O_2 flow (sccm)	RF Power (W)	RF Power density (mW/cm^2)	Rate (nm/s)
dry-etching	400	20	90	186	1.75

Table 6.2: Parameters of the dry-etching process used to isolate the fabricated solar cells. The etching gas CF_4 is diluted into O_2 (20%).

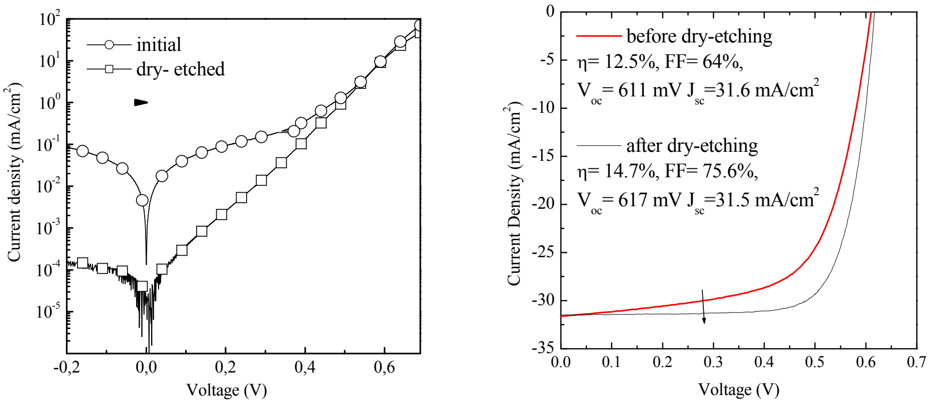

Figure 6.8: Initial and after dry-etching JV characteristics of a solar cell measured in dark (a) and illuminated under AM1.5 conditions (b). The lateral leakage current is reduced in about three orders of magnitude with a consequent FF increase in more than 10%.

Usually, 30-45 seconds are enough to completely etch the a-Si:H emitter. Figure 6.8 compares the dark and AM1.5 electrical characteristics of a solar cell measured before and after the dry-etching process. The lateral leakage current is reduced in about three orders of magnitude, which leads to a FF value more than 10% higher. Then, the final conversion efficiency was increased in more than 2% just insulating the device.

6.2.3 Metallization and grid optimization

The metallic grid is also of critical importance, since it can strongly affect the final solar cell efficiency. A non-optimal finger layout or an excessive shadowing can cause important optical and electrical losses. The basic metallization design follows an H-grid pattern, although artistic designs have been also proposed to convert the busbar into an eye-catching module feature [Radike et al., 1999]. Nevertheless, mathematical calculation and simulation [Burgers, 1999], [Antonini et al., 2003] are generally used to optimize the grid design for optimum carrier collection with as low as possible shadowing. The length of the bus bar, the distance between the fingers and their geometric distribution in the solar cell area are of critical importance. We can distinguish three different power loss effects related to the metallic top contact: the contact resistance between the metal and the ITO layer, the resistance of the metallic fingers and, finally, the shadowed area [Cuevas et al., 2000]. These effects can be quantified as relative power losses with respect to the maximum power point, that is, $p=P_{loss}/P_{mp}$.

a) *losses due to the contact resistance between the metal and the ITO layer*

This power loss can be expressed as:

$$p_c = \rho_c \frac{J_{mp}}{V_{mp}} \frac{S}{W_f} \qquad 6.4$$

where J_{mp} and V_{mp} are the current density and voltage values at the maximum power point, S is the distance between fingers, W_f is the width of the fingers and ρ_c is the specific contact resistance. The J_{mp}/V_{mp} ratio can be approximated by J_{sc}/V_{oc}, which is typically in the 0.055 - 0.06 Ωcm^{-2} range [Cuevas et al., 2000]. In this point we focus on lowering the contact resistance between the metal and the ITO layer, while the S/W_f

ratio will be considered later. We have deposited different metallic contacts (Ag, Au, Ti, Cr, Al) on ITO layers to measure their corresponding contact resistances.

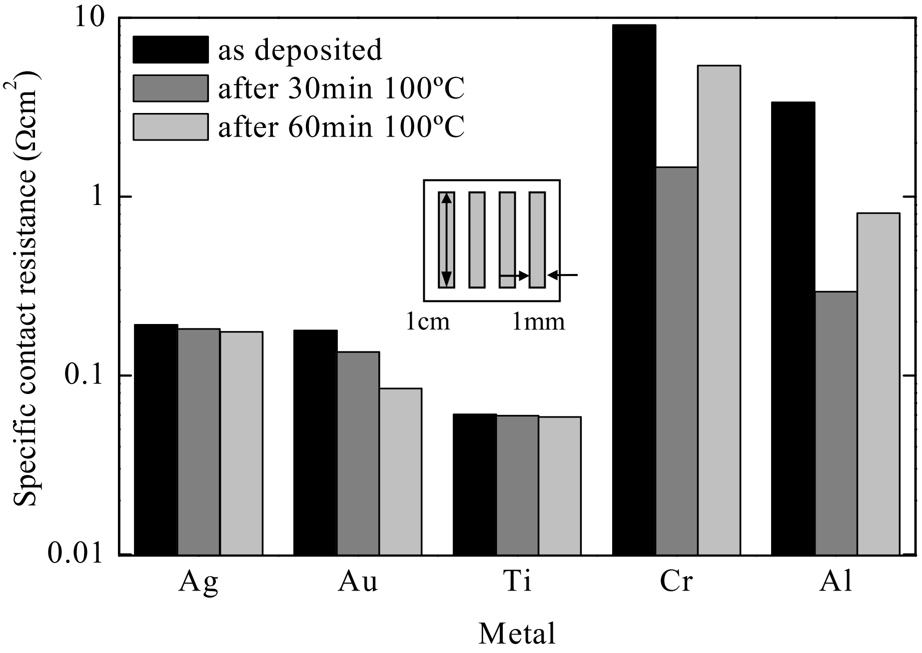

Figure 6.9: Specific contact resistance of different metallic contacts evaporated on ITO layers. The inset shows the mask used for the evaporation process.

These results are shown in figure 6.9, together with the effect of post annealing at 100ºC for different times. At first sight, chromium and aluminium evidenced a higher contact resistance on ITO compared to silver, gold or titanium contacts. Among these, the lowest contact resistance was obtained with titanium. Actually, an usual metallic contact for crystalline silicon solar cells consists of three layers Ti/Pd/Ag consecutively evaporated to obtain good adherence and low series resistance. However, titanium is rather expensive and it always requires the evaporation of additional palladium/silver or at least silver layers. By contrast, either silver or gold directly evaporated on ITO allow quite satisfactory contact resistances of only 0.2 Ωcm^2. In the case of gold, annealing at 100ºC even reduces the contact resistance below 0.1 Ωcm^2. Nevertheless, the higher cost of gold and the inconvenience of additional annealing steps make this option less interesting. Therefore, silver can be considered a good choice in terms of the cost and simplicity of the process.

b) losses due to the resistance of the metallic fingers

This term can be expressed as:

$$p_m = \frac{1}{3} B^2 R_m \frac{J_{mp}}{V_{mp}} \frac{S}{W_f} \qquad 6.5$$

where B is the finger length and R_m the sheet resistance of the metal calculated as:

$$R_m = \frac{\rho}{t_f} \qquad 6.6$$

where ρ is the resistivity of the metal and t_f the finger thickness. Figure 6.10 compares the JV characteristics of two solar cells with silver fingers 0.1 and 1µm thick. As expected, a clear improvement in the FF value is observed for the solar cell with thicker metallic contact. Around open-circuit conditions the parasitic series resistance R_s can be calculated supposing $V \approx IR_s$. Considering that the wafers were 300 µm thick with a resistivity of 14 Ωcm, the bulk contribution of the c-Si substrate to the series resistance is 0.42 Ωcm^2. Then, taken into account that the ITO/Ag contact resistance is around 0.2 Ωcm^2 (figure 6.9), the contribution of the fingers to the series resistance can be finally calculated. These values are shown in table 6.3. We have neglected the contributions to the series resistance related to the Al-BSF and ITO/a-Si:H contact which are, in principle, much smaller.

t_f nm	$R_{s\,(total)}$ Ωcm^2	$R_{s\,(wafer)}$ Ωcm^2	$R_{s\,(TCO\text{-}Ag)}$ Ωcm^2	$R_{s\,(finger)}$ Ωcm^2	FF %	η %
1000	1,5	0,42	0,2	0,88	74,5	14,6
100	2,9	0,42	0,2	2,28	68,4	13,2

Table 6.3: Summary of the resistive losses of solar cells fabricated using Al-BSF contacts. We have neglected the Rs contribution due to the ITO/a-Si:H and Al-BSF contacts.

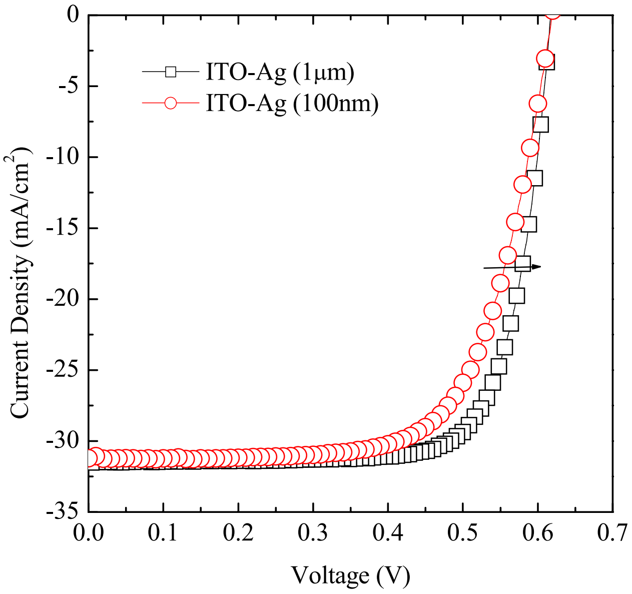

Figure 6.10: JV characteristics measured in AM1.5 conditions for two heterojunction solar cell s on Al-BSF with different Ag grid thicknesses.

Hence, the contribution of the fingers to the series resistance steadily decreases with the thickness of evaporated silver. However, there are technological limitations related to the adherence of silver on ITO layers. In addition, thicker metallic fingers become also wider increasing shadowing losses.

c) <u>losses due to shadowing by the metallic grid</u>

Once the metal and its thickness have been chosen, the design of the metallic grid basically consists in finding the optimum width and separation between fingers to obtain the best compromise between resistive losses and optical shadowing. In particular, the factor to take in consideration is:

$$p_s = \frac{W_f}{S} \qquad 6.7$$

which unfortunately appears inverted in the electrical factors p_c and p_m (equations 6.4-6.6). Therefore, the optical p_s factor should not be reduced below values that would cause higher electrical losses. We have optimized the design of the metallic grid considering all these factors and a set of masks for silver evaporation were fabricated with a theoretically shadowed area of 6.2%. The reflectance spectra of the front ITO layer before and after evaporating the silver grid are compared in figure 6.11. The measurement with the light spot over the fingers is very close to the theoretical value. Anyway, this measurement strongly depends on the position of the light spot. For example, the reflectance increases up to 12% if the spot is over the busbar.

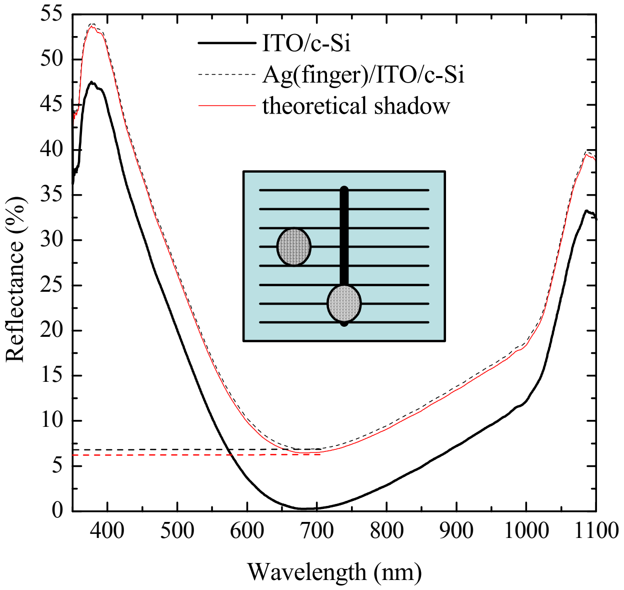

Figure 6.11: Reflectance spectra of the front ITO layer before and after evaporating the 1 μm thick silver grid. The curve with the light spot over the fingers is very close to the theoretical value.

In double-side heterojunction solar cells, a similar ITO/Ag stack was used on the a-Si:H back contact. In this case, the ITO and Ag layers can be deposited over the whole area or, alternatively, bifacial solar cells can be fabricated with the same process optimized for the emitter.

6.3 Heterojunction Solar cells

This section presents a brief summary of the best heterojunction solar cells fabricated during this thesis. These results are organized in three different sections. First, heterojunction solar cells fabricated on c-Si wafers with Al-BSF contacts. Second, optimization of low-temperature deposited back contacts and fabrication of double-side heterojunction solar cells. Finally, comprehensive electrical characterization and equivalent circuit for heterojunction solar cells.

6.3.1 Solar cells fabricated on c-Si wafers with Al-BSF contacts

Different heterojunction emitters have been deposited on CZ (p)c-Si wafers with an Al-BSF contact at the rear side. The resistivity of the wafers was 14 Ωcm. The deposition conditions for the different layers were summarized in table 5.1 (previous chapter). The heterojunction emitter A without intrinsic buffer layer is compared to emitters B1 and B2 that incorporate the same buffer layer but different (n) layer thicknesses. As it was discussed in 5.1, the microstructure of the (n) layer completely changes from basically a-Si:H to partially epitaxial μc-Si:H with the suppression of the buffer layer. Complete solar cells were fabricated using the same front contact. Figure 6.12 shows the JV characteristics measured under AM1.5 illumination (100 mW·cm^{-2}) for the three heterojunction solar cells. The photovoltaic parameters of the electrical characteristics are summarized in table 6.4.

SAMPLE	(i) nm	(n) nm	V_{oc} (mV)	J_{sc} (mA/cm^2)	FF (%)	η (%)
A	-	20 (μc-Si:H)	546	30.8	71.4	12.0
B1	5	10 (a-Si:H)	622	32.7	75.7	15.4
B2	5	20 (a-Si:H)	616	31.4	75.5	14.6

Table 6.4: Photovoltaic parameters of the J-V curves measured under AM1.5 irradiance for the fabricated heterojunction solar cells.

Let's note the most significant difference here: is that the open-circuit voltage plummets around 70mV in the solar cell without buffer layer. This dramatic reduction can be explained considering the partially epitaxial microstructure of this emitter. The absence of heterojunction reduces the built-in voltage and, hence, also the V_{oc} value. Besides, the passivation quality is also degraded due to the increased interface porosity, as it was deduced from ellipsometry measurements (section 5.1.3).

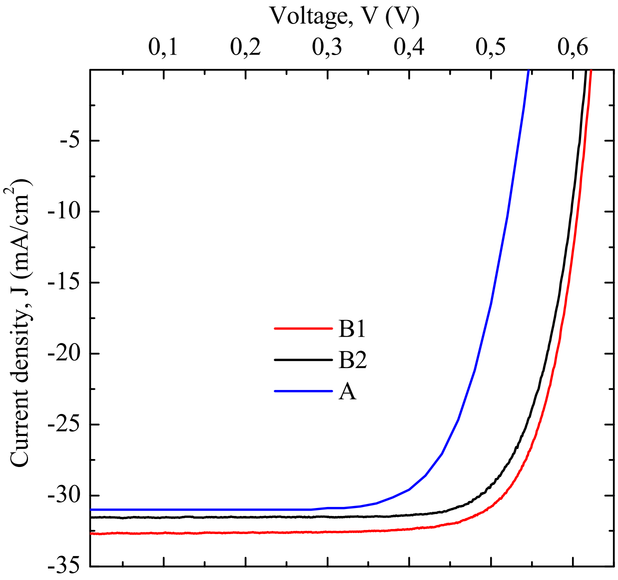

Fig. 6.12: JV electrical characteristics measured under AM1.5 illumination (100 mW·cm^{-2}) for the fabricated heterojunction solar cells.

On the other hand, especially remarkable are the relatively high V_{oc} values of the solar cells B1 and B2. In fact, since implicit-V_{oc} values measured by QSS-PC were close to 700 mV for these emitters (see section 5.1); we expect actual values of around 620 mV to be limited by the quality of the Al-BSF rear contact. It is important to point out that the n-doped layer could be thinned to only 10 nm without any loss in V_{oc}.

Figure 6.13 shows the External Quantum Efficiency (EQE) curves of the solar cells under study. As expected, if we compare the solar cells B1 and B2 with amorphous emitters, the thinner one leads to higher EQE values in the short wavelength range ($\lambda <$ 600 nm). This was the reason for the higher J_{sc} value of the solar cell B1 compared to B2 (table 6.4). The solar cell with microcrystalline emitter (A) has the lowest J_{sc} values, even though the absorption in the emitter should be lower than in amorphous layers. However, the strong front interface recombination deduced from the fast decrease at short wavelengths seems to reduce the J_{sc} value. The EQE curves come together for longer wavelengths, since identical Al-BSF contacts were used in all cases.

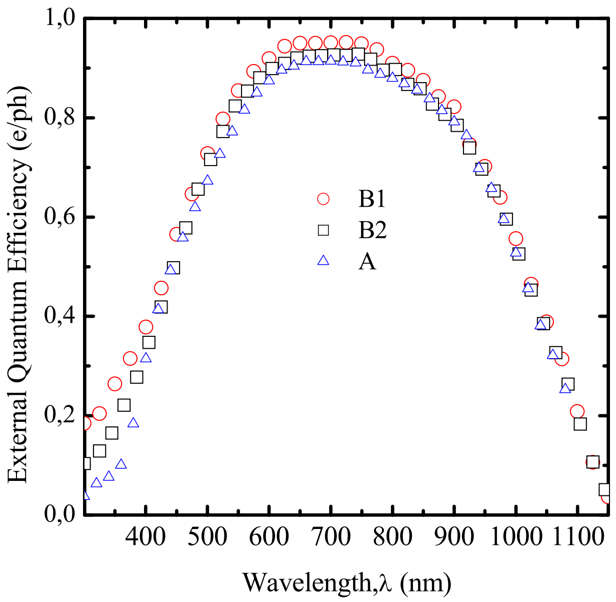

Fig. 6.13: EQE curves of the fabricated heterojunction solar cells. The emitter thickness and microstructure clearly influenced the response at shorter wavelengths.

6.3.2 Bifacial solar cells

The main limitation in terms of V_{oc} for the previously studied devices could be attributed to the Al-BSF contact, since the implicit-V_{oc} values were as high as 700 mV for emitters with intrinsic buffer layer. Moreover, the fabrication of Al-BSF contacts involves a high temperature step of less technological interest. Then, we have fabricated bifacial heterojunction solar cells in a fully low-temperature process. The scheme of these devices is shown in figure 6.14.

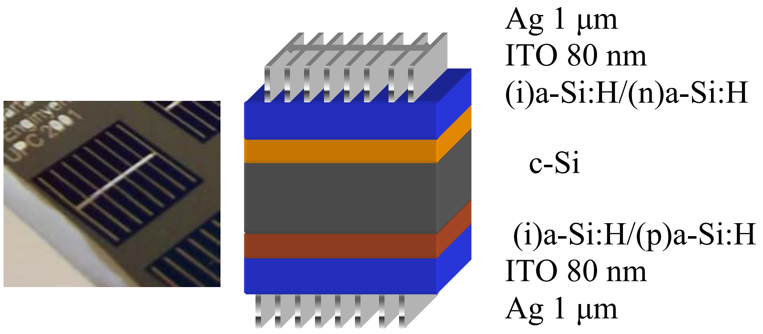

Figure 6.14: Picture and scheme of the fabricated bifacial heterojunction solar cells.

The deposition conditions of the different layers used in these devices are summarized in table 6.5. Attending to the microstructure and passivation quality, we have selected four back contact configurations with either intrinsic buffer layer or not and two different p-type doping levels. These structures have been descriptively labelled P, IP, P^+ and IP^+. The emitter was the same in all cases.

film	T_s (ºC)	H_2 (sccm)	SiH_4 (sccm)	Doping (sccm)	Pressure (mbar)
i	100	-	2	-	3.5×10^{-3}
n	200	28	2	0.04	8×10^{-2}
p	100	2	1.5	0.02	1×10^{-2}
p^+	100	4	2	0.04	2×10^{-2}

Table 6.5: Deposition conditions used to grow the silicon films of the bifacial heterojunction solar cells. The wire temperature was 1600ºC for intrinsic a-Si:H and n-doped films, but 1750 ºC for p-doped films. The doping precursors were phosphine and diborane for n- and p-type films, respectively.

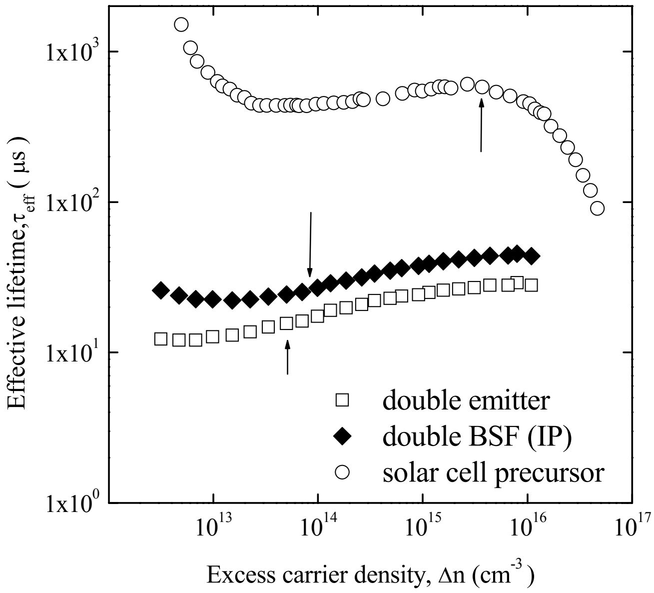

Figure 6.15: QSSPC data for the symmetric emitter and symmetric BSF structures compared to the solar cell precursor. The arrows point the values at 1 sun irradiance.

Figure 6.15 compares QSS-PC data of the solar cell precursor with symmetric structures where either the emitter or the low temperature BSF contact (IP in this case) has been deposited on both sides. As it is clearly observed, the performance of the solar cell is limited by the low temperature BSF contact. Nevertheless, the implicit-V_{oc} values (section 5.2.4) exceeded the limit imposed by traditional Al-BSF contacts.

Complete heterojunction solar cells were fabricated incorporating the different back contact alternatives. The corresponding JV characteristics under AM1.5 illumination are shown in figure 6.16, whereas the relevant photovoltaic parameters are summarized in table 6.6. The P and IP low temperature BSF contacts allowed performances comparable to the one obtained with an Al-BSF. Especially remarkable are the V_{oc} values exceeding 610 mV in a fully low temperature process by HWCVD (< 200ºC). Unfortunately, the solar cells incorporating P^+ and IP^+ back contacts evidenced "S-shaped" JV curves. This effect has been previously reported by different groups, but concerning different heterojunction emitters with traditional back contacts, and it has been attributed to an unfavourable energy band configuration for carrier collection [Froitzheim et al., 2002], [Unold et al., 2000]. The highly doped P^+ and IP^+ back contacts present an essentially amorphous microstructure in contrast to the significant crystalline fraction present in the case of lower doping levels (P, IP), as deduced from ellipsometry measurements in section 5.2.4. This variation should lead to higher band discontinuities that seem to degrade the carrier collection at the back contact. As it was commented previously in section 6.1, the work function of the ITO layer could not be high enough and an undesired inverted Schottky barrier would be created in the interface between the ITO and the (p^+) a-Si:H film.

SAMPLE	V_{oc} (mV)	J_{sc} (mA/cm^2)	FF (%)	η (%)
P	613	30.3	77.9	14.5
IP	618	29.6	75.0	13.7
P^+	500	13.6	S-shaped	-
IP^+	645	29.2	S-shaped	-

Table 6.6: Electrical parameters of the JV curves measured under AM1.5 irradiance for the heterojunction solar cells fabricated with the different low temperature BSF contacts.

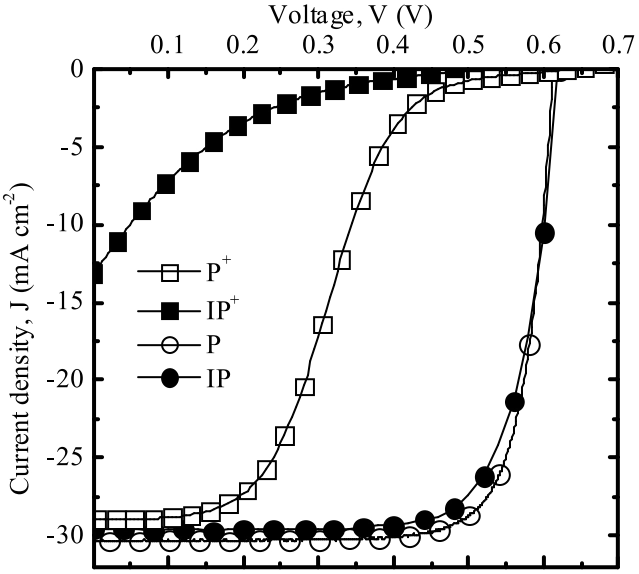

Figure 6.16: JV characteristics measured under AM1.5 irradiance (100mW·cm^{-2}) for the fabricated double-side heterojunction solar cells.

Finally, figure 6.17 shows the External Quantum Efficiency (EQE) curves of the double-side heterojunction solar cells with low doping BSF contacts (P, IP) and with an Al-BSF contact. Since the heterojunction emitter is the same in all cases, the lower response of the IP device in the short wavelength range ($\lambda < 600$ nm) is attributable to differences in the quality of the front contact, namely the ITO antireflection coating. In the long wavelength range ($\lambda > 900$ nm), the response with the low temperature IP back contact is very close to the case with a traditional Al-BSF. By contrast, the P back contact does not reach the quality of the other cases. The behaviour of the EQE curves agrees with the differences observed in the J_{sc} values of the solar cells (Table 6.6).

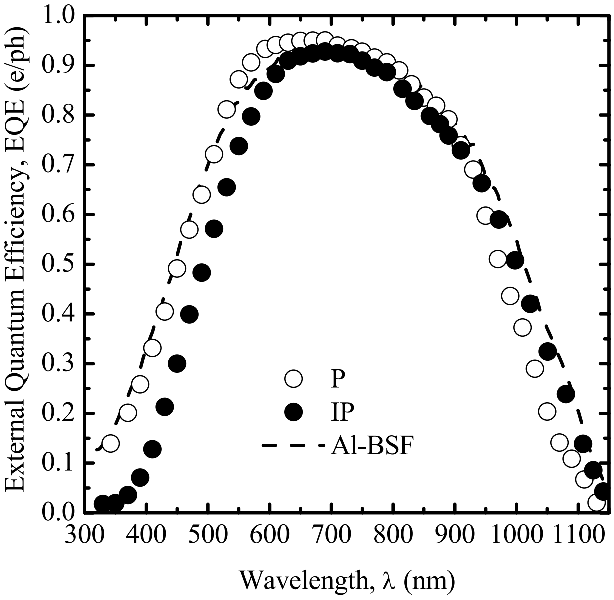

Figure 6.17: External Quantum Efficiency curves of the double-side heterojunction solar cells with P and IP BSF contacts compared to the case with a traditional Al-BSF contact.

6.3.3 Equivalent circuit and thermal dependence of the electrical characteristics

The best bifacial heterojunction solar cell on p-type c-Si was reproduced on n-type substrates as a first approach to the complementary technology. The JV characteristics of both cells have been measured under AM1.5 conditions (100 $\mathrm{Wcm^{-2}}$) for front and rear side illumination. The measured curves are shown in figure 6.18 and the resulting photovoltaic parameters have been summarized in table 6.7.

Two important conclusions can be extracted from these results. On the one hand, it is remarkable the photovoltaic response obtained when illuminating the solar cells from the rear side. This is an additional advantage of bifacial heterojunction solar cells, as it has been demonstrated by Sanyo with commercial bifacial modules [www.sanyo.com] where the power generated is increased more than 8% due to the diffuse rear side illumination.

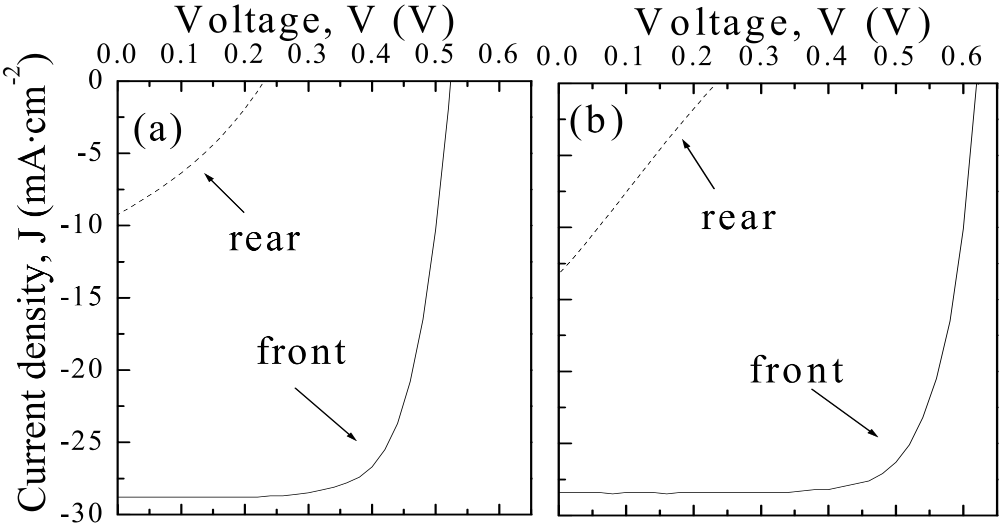

Figure 6.18: JV characteristics under AM1.5 illumination for a solar cell on n-type (a) and p-type c-Si wafers (b). In both cases the JV measurements are shown illuminating the device from the front and from the rear side.

solar cell	illumination	V_{oc} (mV)	J_{sc} (mAcm^{-2})	FF (%)	η (%)
p-type	front side	618	28.4	74.8	13.1
	back side	242	13.6	27	0.89
n-type	front side	525	28.8	71	10.7
	back side	226	9.3	32	0.68

Table 6.7: Photovoltaic parameters corresponding to the J-V characteristics of the bifacial heterojunction solar cells on p- and n-type c-Si (figure 6.18). Illumination from both sides is considered.

On the other hand, it is surprising the strong reduction in the V_{oc} values close to 100 mV when using n-type substrates. Maydell et al. have shown that the substrate strongly determines the required properties for the a-Si:H layers, especially concerning the doping level [Maydell et al., 2006]. To obtain a high V_{oc} value, the Fermi level in the thin amorphous emitter should be as close as possible to the band edge. It means that highly doped layers have to be used. But in the case of our (p)a-Si:H layers deposited by HWCVD, the conductivies are still far from the n-doped ones. Then, (p)a-Si:H layers used as emitters instead of back contacts allow lower built-in voltages that those obtained in the complementary structure.

In order to better understand the electronic behaviour of both heteroestructures, we have studied the thermal dependence of their electrical characteristics. The dark JV characteristics of the heterojunction solar cells have been measured in the temperature range 300 - 348K (figure 6.19).

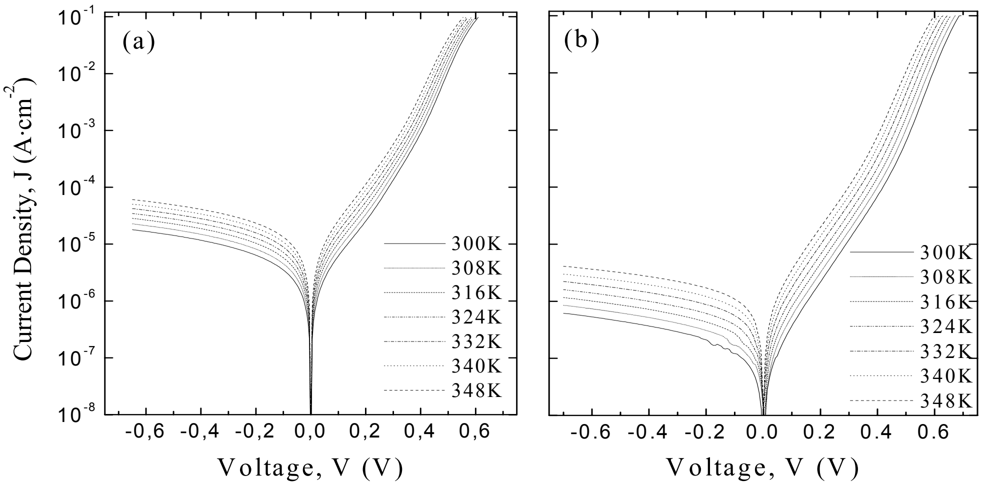

Figure 6.19: Dark JV characteristics of the n-type (a) and p-type (b) heterojunction solar cells measured at different temperatures in the range of 300-348K.

As it can be observed, the forward characteristic evidences two different regions that suggest a two-diode model: recombination (< 0.4 V) and diffusion diode (0.4 - 0.6 V). Then, we have described the electrical characteristics by means of the widely used equivalent circuit [Sze, 1981]:

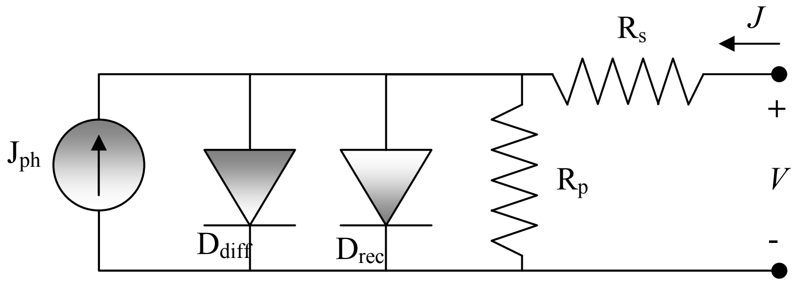

Figure 6.20: Equivalent circuit of the solar cells.

In this model (figure 6.20), the diffusion and recombination terms of the current density are represented by the corresponding diodes (D_{diff} and D_{rec}), together with the current source that takes into account the photogenerated current density (J_{ph}). Besides, parasitic parallel and series resistance are also considered (R_p and R_s). Then, the corresponding electrical characteristic can be calculated with the following equation:

$$J = J_{01}\left(\exp\left(\frac{V - R_s J}{n_1 kT}\right) - 1\right) + J_{02}\left(\exp\left(\frac{V - R_s J}{n_2 kT}\right) - 1\right) + \frac{V - R_s J}{R_p} - J_{ph} \qquad (6.1)$$

where J_{01} and J_{02} are the saturation current densities for the two diodes with their corresponding ideality factors n_1 and n_2. We have extracted these parameters for both solar cells on n- and p-type c-Si by fitting the dark JV curves shown in figure 6.19. The thermal dependences of J_{01}, J_{02}, n_1 and n_2 are shown in figure 6.21. The diffusion diode with an ideality factor around 1 and no significant thermal dependence is clear for both structures. The solar cell on p-type c-Si shows a much better room temperature saturation current density J_{01} = 0.7 pA than the device on n-type substrate J_{01} = 80 pA. As a consequence, the V_{oc} of the device on p-type wafer is higher than on n-type, as it was shown in table 6.7. The recombination diode presents an ideality factor higher than 2 in both cases, while the saturation current density J_{02} is again much higher for the n-type substrate.

The activation energy (E_a) of J_{01} for the p-type substrate is 1.17 eV that, as expected, is very close to the silicon band gap (E_g = 1.12 eV). The measured activation energy for J_{02} is 0.48 eV. In the literature, the activation energy of the recombination diode has been expressed as $E_a = E_g/2$ [Jensen et al., 2000] when considering one recombination level at midgap with the same capture cross-sections for electrons and holes. Since the value of E_a = 0.48eV is near to $E_g/2$ = 0.56 eV, it is possible to deduce one recombination level close to the midgap for this structure.

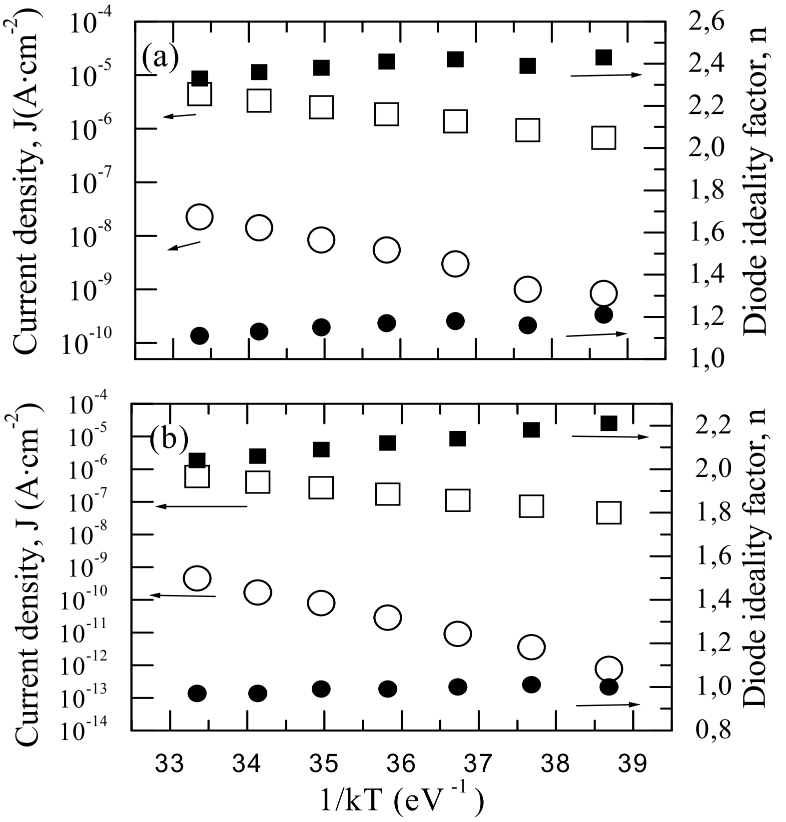

Figure 6.21: Thermal dependence of the saturation current density and diode ideality factor for the recombination (□) and diffusion diodes (O) on n- (a) and p-type c-Si substrates (b).

By contrast, the behaviour of the solar cell on n-type c-Si is more complicated. The activation energy for the diffusion diode was $E_a = 0.65$ eV, while for the recombination one it was only $E_a = 0.3$ eV. These two values are far from simply the gap and midgap, respectively. Then, it is possible that the band discontinuity in the valence band or a different defect structure affect the transport mechanisms in the solar cell fabricated on n-doped c-Si. Besides, the reduced quality of the p-doped a-Si:H layer strongly affects the final performance of the device because now it is the emitter instead of a BSF contact. Actually, since it is rather difficult to obtain quality highly p-doped a-Si:H layers by HWCVD, state-of-the-art heterojunction solar cells by this technique have been fabricated on p-type substrates.

Chapter 7: Conclusions

"An author is a fool who, not content with boring those
he lives with, insists on boring future generations"
Montesquieu

The possibility to fabricate a-Si:H/c-Si heterojunction devices by Hot-Wire Chemical Vapor Deposition (HWCVD) has been demonstrated in this thesis. This deposition technique has some technological advantages compared to PECVD in terms of deposition rate, gas decomposition and scalability. Besides, the lack of ion bombardment could be beneficial for the interface between amorphous and crystalline silicon. Furthermore, the a-Si:H and μc-Si:H materials obtained by HWCVD fulfill all the optical and electrical requirements to form a good heterojunction with c-Si substrates.

We have deeply studied the influence of the intrinsic thin buffer layer in the heterojunction emitter. Ellipsometry measurements have been very useful to identify the properties of the interface and the quality of the films. We have observed that the thin intrinsic a-Si:H layer reduces the interface state density, which leads to a better surface passivation. Besides, it also has a great influence in the growth mechanism of the n-doped layer promoting the formation of an abrupt heterojunction. The most dense and amorphous layers have allowed very low surface recombination velocities ($S_{eff} < 30$ cm·s^{-1}) and high implicit-V_{oc} values (> 700 mV) measured by the QSSPC technique. On the contrary, a partially epitaxial growth has been observed in heterojunction emitters deposited directly without thin buffer layer obtaining implicit–V_{oc} values limited to only 600 mV.

We have optimized the heterojunction emitter of the solar cell onto p-type wafers with a traditional Al-BSF contact. Complete solar cells with a conversion efficiency of 15.4% (V_{oc} = 622 mV J_{sc} = 32.7 mA·cm^{-2}, FF = 75.7%) have been fabricated. In fact, since the implicit-V_{oc} measured by QSS-PC was close to 700 mV for the optimized emitters, the final V_{oc} values of around 620 mV could be limited by the quality of the Al-BSF rear contact. Actually, reported surface recombination velocities for Al-BSF contacts are usually in the range of 10^3 cm×s^{-1}, while we have obtained values as low as 30 cm×s^{-1} for a-Si:H layers.

Low temperature deposited BSF contacts based on boron-doped a-Si:H films deposited by HWCVD have been used to replace traditional high temperature Al-BSF contacts. Extensive experiments to optimize these low temperature BSF contacts were performed with relatively good results. QSS-PC measurements indicate that the intrinsic buffer layer reduces interface recombination at the back surface leading to lower S_{eff} values. The growth mechanism of the doped layer is also altered with the presence of the intrinsic buffer layer, which allows a compact stack formed by an a-Si:H layer followed by a conducting µc-Si:H one. Then, a good passivation quality (implicit-V_{oc} > 650 mV) can be achieved if we are able to form the desired abrupt heterojunction. Nevertheless, the back contact is still the factor limiting the performance of our devices in terms of V_{oc}.

A comprehensive optimization of the front contact has been also done. On the one hand, the ITO layer has been optimized for a high optical transmittance (> 90%) and low electrical resistivity (< 4×10^{-4} Ωcm^{-1}). State-of-the-art values have been achieved for ITO films deposited by RF sputtering magnetron at room temperature. Nevertheless, the control of the work function is still a subject for further research, since it has appeared as a critical parameter to avoid parasitic Schottky barriers in the device. On the other hand, we have also considered final technological steps such as the isolation of the solar cell by dry-etching, the metallization process and the geometric design of the metallic grid. Very low series resistances (< 1.5 Ωcm^2) combined with high shunt resistances (> 10^6 Ωcm^2) and low optical looses (shadowing < 6.2%) have been systematically obtained in our heterojunction solar cells.

Double-side heterojunction solar cells by HWCVD with a conversion efficiency of 14.5% (V_{oc} = 613 mV J_{sc} = 30.3 mA·cm^{-2}, FF = 77.9%) have been fabricated in a fully low temperature process (< 200ºC). Unfortunately, the low temperature BSF structures with better surface passivation presented an unfavourable band configuration to contact complete devices. Only p-doped layers with a significant crystalline fraction allowed a good ohmic contact with the rear ITO layer. Then, the diborane flow can not be increased too much due to its amorphization effect in HWCVD processes.

Finally, we have also started the research of heterojunction solar cells on n-type c-Si substrates. The best structure obtained on p-type substrates was symmetrically replicated on n-type wafers. Then, preliminary heterojunction solar cells on n-type substrates reached promising efficiencies up to 10.7%. The JV characteristics of bifacial solar cells on p- and n-type wafers have also been measured for illumination from the rear side. A slight response is obtained in both cases with V_{oc} over 200 mV, moderated J_{sc} around 10 mA×cm^{-2} and FF around 25%.

References

Aberle A.G., Crystalline Silicon Solar Cells – Advanced Surface Passivation and Analysis, Center for Photovoltaic Engineering, University of New South Wales, Sydney, (1999)

Aberle A.G., Prog. Photovolt: Res. Appl. 8 (5) (2000) p.473

Alpuim P., Chu V., Conde J.P., J. Vac. Sci. Technol. A 19 (5) (2001) p.2328

Alsema E., De Wild-Scholten M., MRS Fall meeting, Boston (2005), G3.3

Altermatt P.P., Heiser G., Aberle A.G., Wang A., Zhao J., Robinson S.J., Bowden S., Green M.A., Prog. Photovolt. Res. Appl. 4, (1996) p. 399

Anderson R. L., Solid-State Electron. 5 (1962) p. 341

Antonini A., Stefancich M., Vincenzi D., Malagu C., Bici F., Ronzoni A., Martinelli G., Solar Energy Materials & Solar Cells 80 (2003) p.155

Aspnes D. E., Studna A., Kinsbron E., Phys. Rev. B 29 (1984) p. 768

Ayral A., *"Techniques innovantes pour la caractérisation optique microstructurale de couches minces"* , CNRS EDITIONS

Bauer S., Schröder B., Oechsner H., J. Non-Cryst. Solids 227-230 (1998) p. 34

Bergmann R.B., Applied Physics A, 69, (1999) p. 187

Blakers W., Weber K. J., Everett E., Franklin E., Deenapanray P., Proc. of the 4th World Conference on Photovoltaic Energy Conversion (WCPEC '06) vol.2, Waikoloa, Hawaii, (2006) p. 2181

Boccara A. C., Fournier D., and Badoz J., Appl. Phys. Lett. 36, (1979) p. 130

Boycheva S., Krasilnikova Sytchkova A., Grilli M.L., Piegari A., Thin Solid Films 515 (2007) p. 8469

Branz H. M., Teplin C. W., Young D. L., Page M. R., Iwaniczko E., Roybal L., Bauer R., Mahan A.H., Xu Y., Stradins P., Wang T., Wang Q., Thin Solid Films, In Press, Corrected Proof (2007)

Brodsky M.H., Cardona M., Cuomo J.J., Phys. Rev. B 16, (1977) p. 3556

Brogueira P., Chu V., Ferro A.C., Conde J.P., J. Vac. Sci. Technol. A 15 (6) (1997) p.2968

Bruggemann D.A.G., Ann Phys. (Leipzig) 24 (1935) p. 636

Burgers A. R., Prog. Photovolt: Res. Appl. 7, (1999) p.457

Burgers R., Prog. Photovolt. Res. Appl. 7, (1999) p.457

Burstein E.,Phys. Rev. 93, (1954) p. 632

Bustarret E., Hachicha M.A., Brunel M., Appl. Phys. Lett. 52 (1988) p.1675

Centurioni E., Iencinella D., IEEE Electron Device Letters 24, 4 (2003) p.177

Centurioni E., Iencinella D., Rizzoli R., Zignani F., IEEE Transaction on Electron Devices 51 (11) (2004), p. 1818

Chapin D. M., Fuller C. S., Pearson G. L., J. Appl. Phys., 25 (1954) p. 676

Chen M., Pei Z.L., Wang X., Yu Y.H., Liu X.H., Sun C., Wen L.S., J. Phys. D: Appl. Phys. 33 (2000) p. 2538

Christensen J.S., Ulyashin A.G., Maknys K., Kuznetsov A.Yu. and Svensson B.G., Thin Solid Films 511 (2006) p.93

Collins R.W., Appl. Phys. Lett. 53 (12) (1988) p. 1086

Conrad E., Korte L., Maydell K. v., Angermann H., Schubert C., Stangl R., Schmidt M., Proc. Of 21st European Photovoltaic Solar Energy Conference, Dresden (2006) p.784

Cuevas A., Russell D., Prog. Photovolt. Res. Appl. 8 (2002) p. 603

Cuniot M. Lequeux N., Philosophical Magazine B, 64, 6 (1991) p.723

Curtins H., Veprek S., Solid State Communications 57 (4) (1986) p. 215

Damon-Lacoste, J., Ph.D. Thesis, Ecole Polytechnique Paris (2007)

Dauwe S, Schmidt J, Hezel R. Proceedings of the 29th IEEE Photovoltaic Specialists Conference, New York, (2002) p.1246

Doyle, J., Robertson, R., Lin, G. H., He, M. Z., Gallagher, A. J.Appl. Phys. 64 (1988) p.3215

Duerinckx F. Szlufcik J., *Solar Energy Materials and Solar Cells 72 (2002) p. 231*

El Akkad F., Marafi M., Punnoose A., Prabu G., Phys. Stat. Sol. (a) 177, (2000) p. 445

Fedders P. A., Leopold D. J., Chan P. H., Borzi R., and Norberg R. E., Phys. Rev. Lett. 85 (2000) p. 401

Feenstra K. F., Schropp R. E. I., Van der Weg W. F., J.Appl. Phys. 85 (1999) p. 6843

Ferre R., Martin I., Ortega P., Vetter M., Torres I., and Alcubilla R., J. Appl. Phys. 100, (2006) p. 073703

Ferre R., Martín I., Vetter M., Garín M., and Alcubilla R., Appl. Phys. Lett. 87, (2005) p. 202109

Fesquet L., Olibet S., Vallat-Sauvain E., Shah A., Ballif C., Proc. of the 22th EU-PVSC Conference, Milan, (2007)

Fonrodona M., Escarré J.,Villar F., Soler D., Asensi J.M., Bertomeu J.,Andreu J., Solar Energy Materials and Solar Cells 89 (2005) p. 37

Fonrodona M.., Ph.D. Thesis, University of Barcelona (2003)

Fontcuberta i Morral A., Roca i Cabarrocas P., Clerc C., Physical Review B 69 (2004) p.125

Fontcuberta i Morral A., Roca i Cabarrocas P., Thin Solid Films 383 (2001) p. 161

Froitzheim A., Angermann H., Elstner L., Fussel W., Kliefoth K., Knechtel J., Schmidt M., Sinh N., Weiser H., Fuhs W., Proc. of the 16th European PVSEC, Glasgow (2000) p. 1580

Froitzheim A., Brendel K., Elstner L., Fuhs W., Kliefoth K., Schmidt M., J. Non-Cryst Solids 299 (2002) p.663

Fritts, C. E., American Journal of Science 26 (1883) p. 465

Fthenakis V., Alsema E., Prog. Photovolt: Res. Appl. 14 (3) (2006) p. 275

Funke C., Sciurova O., Möller H.J., Stephan M., Fröhlich K.J., Seifert C., Bachmann A., Müller A., Proc. 19th PVSEC, Paris, (2004) p.1266ç

Fuhs W., Niemann K. and Stuke J., Bull. Am. Phys. Soc. **19** (1974) p. 393

Glunz S.W., Solar Energy Materials and Solar Cells 90 (2006) p.3276

Glunz S. W., Grohe A., Hofmann M., Janz S., Schultz O., Vetter M., Martín I., Ferre R., Bermejo S., Wolke W., Warta W., Preu R., and Willeke G., 20th European Photovoltaic Solar Energy Conference, Barcelona (2005) p. 572

Goetzberger A., Hebling C. Schock H.W., Mater. Sci. Eng., R 40 (2003), p. 1

Goetzberger A., Luther J., Willeke G., Solar Energy Materials & Solar Cells 74 (2002) p.1

Green M.A., Emery K., King D.L., Igari S., Warta W., Prog. Photovolt: Res. Appl. 14 (2006) p.14

Green M.A., Prog. Photovolt: Res. Appl. 14 (2006) p.383

Green M.A., Prog. Photovolt: Res. Appl. Vol. 8, 5 (2000) p.443

Green M.A, Blakers A.W., Zhao J., Milne A.M., Wang A., Dai X., IEEE Transactions on Electron Devices 37 (1990) p.331

Green M.A., Solar Cells, University of New South Wales, Sydney, Australia, (1982) p. 52

Green M.A., Solar Cells: Operating Principles, Technology and System Applications, Prentice Hall (1981)

Gruenbaum PE, Gan JY, King RR, Swanson RM. Proc. of the 21st IEEE Photovoltaic Specialists Conference, Kissimimee, (1990) p. 317

Gudovskikh A.S., Ibrahim S., Kleider J.-P., Damon-Lacoste J., Roca i Cabarrocas P., Veschetti Y., Ribeyron P.-J., Thin Solid Films, In Press, Corrected Proof (2007)

Guha S., Narasimhan K.L., Pietruszko S.M., J. Appl. Phys. 52 (2) (1981) p. 859
Hall R.N., Phys. Rev. 87, (1952) p. 387

Hamakawa Y., Okamoto H., Okuda K., United States Patent 4,496,788, (1985)

Hamakawa Y., Thin-Film Solar Cells: Next Generation Photovoltaics and Its Applications, Springer (2004)

Han D., Wang K., Owens J.M., Gedvilas L., Nelson B., Habuchi H., Tanaka M., J. Appl. Phys. 93 (7) (2003) p. 3776
Han D., Yue G., Lorentzen J.D., Lin J., Habuchi H., Wang Q., J. Appl. Phys. 87 (2000) p. 1882

Hegedus S., Prog. Photovolt: Res. Appl. 14, (2006) p.393

Heintze M., Zedlitz R., Wanka H.N., Schubert M.B., J. Appl. Phys. 79 (1996) p. 2699

Hering G., Spectrolab reports 40.7-percent cell efficiency—world record, Photon international (2007) p. 1

Hermle, M., Dicker, J.,Warta, W.,Glunz, S.W., Willeke, G. Proc. of 3rd World Conference on Photovoltaic Energy Conversion, Vol.2 (2003) p.1009

Hermle M., Schneiderlöchner E. , Grupp G., Glunz S. W., Proc. of the 20th European Photovoltaic Solar Energy Conference, Barcelona (2005) p.810

Honda N., Masuda A., Matsumura H., J. Non-Cryst. Solids 266 (2000) p.100

Horbach C., Beyer W., Wagner H., J. Non-Cryst. Solids 137 (1991) p.661

http://us.sanyo.com/industrial/solar/downloads/0619%20SANYO%20HIT%20Energy%20Conversion%20Efficiency.pdf

http://www.avasolar.com/

http://www.ecn.nl/library/reports/2006/c060010.html

http://www1.eere.energy.gov/solar/pv_basics.html

Huster F., Proceedings of the 20th European Photovoltaic Solar Energy Conference and Exhibition, Barcelona, (2005) p. 635

Ishibashi K, Thin Solid Films 395 (2001) p. 55

Jadkar S. Jaydeep R., Sali V., Musale D. V., S. Kshirsagar T., Takwale M. G., Solar Energy Materials and Solar Cells 71 (2002) p.153

Jellison Jr. G.E. Chisholm M.F., Gorbatkin S.M., Appl. Phys. Lett. 62 (25) (1993) p. 348

Jellison Jr. G.E., Modine F.A., Appl. Phys. Lett, 69 (1996) p. 371

Jellison Jr. G.E., Thin Solid Films 234 (1994) p. 419

Jeong J.W., Rohatgi A., Yelendur V., Ebong A., Rosenblum M.D., Kalejs J.P., IEEE Transactions on Electron Devices 48 (2001) p. 2836

Jensen N., Rau U., Hausner M., Uppal S., Oberbeck L., Bergmann R.B., Werner J. H., J. of Appl. Phys., 87, 5 (2000) p.2639

Jensen, N., Hausner, R.M., Bergmann, R.B., Werner, J.H., Rau, U., Prog. Photovolt: Res. Appl., 10, (2003) p. 1

Kail F., Ph.D. Thesis, Ecole Polytechnique Paris (2005)

Karasawa T. and Miyata Y., Thin Solid Films 223, (1993) p. 135

Kim J. S., Lagel B., Moons E., Johansson N., Baikie I. D., Salaneck W. R., Friend R. H., Cacialli F., Synth. Metal 111(2000) p. 311

Kim Y.S., Drowly C.I. Hu C., Conf. Record 14th IEEE Photovoltaic Specialists Conference, San Diego, (1980) p. 560

King D.L., Schubert W.K., Hund T.D., Conf. Record, 1st World Conference on Photovoltaic Energy Conversion, Hawaii, (1994) p.1660

Knapp K., Jester T. Solar Energy, 71 (3), (2001) p. 165

Kobayashi H., Ishida T., Nakato Y., Tsubomura H., J. Appl. Phys. 69 (1991) p.6065

Koh J., Ferlauto A.S., Rovira P.I., Wronski C.R., Collins R.W., Appl. Phys. Lett. 75 (1999) p. 2286

Kunst M., von Aichberger S., Citarella G., Wünsch F., J. Non-Cryst. Sol. 299 (2002) p.1198

Kunst M., Abdallah O. and Wünsch F., Sol. Energy Mater. Sol. Cells 72, 335 (2002b)

Langford A.A., Fleet M.L., Nelson B.P., Lanford W.A., Maley N., Phys. Rev. B 45 (1992) p. 13367

Lauinger T., Schmidt J., Aberle A.G., Hezel R., Appl. Phys. Lett. 68 (1996) p.1232

Le Quang N. , Goaer G., Coustier F., Gauthier M., Duffar T., Delannoy Y., Mangelinck N., Barvinschi F.- Proc. of the 19th European Photovoltaic Solar Energy Conference and Exhibition (2004) p. 1259

Lee J.Y., Glunz S.W., Solar Energy Materials and Solar Cells 90 (2006) p.82

Leguijt C, Lölgen P, Eikelboom JA, Weeber AW, Schuurmans FM, Sinke WC, Alkemade PFA, Sarro PM, Marée CHM, Verhoef LA, Solar Energy Materials and Solar Cells 40, (1996) p.297

Liu F., Zhu M., Feng Y., Han Y., Liu J., Kasouit S., Vanderhaghen R., J. Non-Cryst. Sol. 299 (2002) p.385

Losurdo M., Grimaldi A., Sacchetti A., Capezzuto P., Ambrico M., Bruno G., Roca F., Thin Solid Films 427(2003) p. 171

Lucovsky G., Nemanich R.J., Knights J.C., Physical Review B 19 (4) (1979) p. 2064

Mäckel H., Lüdemann R., J Appl Phys 92 (2002), p. 2602

Mahan A. H., Carapella J., Nelson B. P., Crandall R. S., Balberg I., J.Appl. Phys. 69, (1991) p.6728

Mahan A.H., Thin Solid Films 501 (2006) p. 3

Mahan A.H., Nelson B.P., Salamon S., Crandall R.S., J. Non-Cryst Solids 137 (1991) p.657

Mahan A.H., Sol. Energy Materials & Solar Cells 78 (2003) p. 299

Mahan A.H., Yang J., Guha S., Williamson D.L., Phys. Rev. B 61 (3) (2000) p. 1677

Mahan, A. H., Carapella, J., Nelson, B. P., Crandall, R. S., J . Appl. Phys. 69, (1991) p.6728

Maissell L.I. Glang R. (eds.), Handbook of Thin film Technology, Mc Graw Hill, New York, (1970)

Martín I., Vetter M., Orpella A., Puigdollers J., Cuevas A. , Alcubilla R., Appl. Phys. Lett. 79 (2001) p. 2199

Martín I., Vetter M., Orpella A., Voz, C., Puigdollers J., Alcubilla R., Kharchenko A.V., and Roca i Cabarrocas P., Appl. Phys. Lett. 84 (2004) p. 1474

Martín I., Vetter M., Garín M., Orpella A., Voz C., Puigdollers J., and Alcubilla R., J. Appl. Phys. 98, (2005) p. 114912

Martín I., Vetter M., Orpella A., Voz C., Puigdollers J., and Alcubilla R., Appl. Phys. Lett. **81**, (2002) p. 4461

Martin, Ph.D. Thesis, Universitat Politècnica de Catalunya (2004)

Matsumura H., Jap.J. Appl.Phys. 25 (1886) p. 1949

Maydell K. v., Conrad E., Schmidt M., 15th International Photovoltaic Science and Engineering Conference, Shanghai, (2005) p. 881

Maydell K., Conrad E., Schmidt M., Prog. Photovolt: Res. Appl. 14 (2006) p.289

Maydell, K. v., Schmidt, M., Korte, L., Laades, A., Conrad, E., Stangl, R., Scherff, M. & Fuhs, W., 31 IEEE Photovoltaic Specialists Conference held in Coronado Springs Resort, Lake Buena Vista (2005) p. 1225

Maydell K.v., Korte L., Laades A., Stangl R., Conrad E., Lange F. and Schmidt M., J. Non-Cryst. Sol. 352 (2006) p. 1958

Meng L., dos Santos M.P., Thin Solid Films 322 (1998) p.56

Minami T., J. Vac. Sci. Technol. A, 17 (1999) p. 1765

Möller H.J., Adv. Eng. Mater. 6 (2004) p. 501

Morikawa H., Fujita M., Thin Solid Films 339 (1999) p.309

Morikawa H., Fujita M., Thin Solid Films, 359 (2000) p.61

Moutinho H.R., Romero M.J., Jiang C.-S., Xu Y., Nelson B.P., Jones K.M., Mahan A.H., Al-Jassim M.M., Proc. of the 29th IEEE PV Specialists Conference, New Orleans (2002)

Muñoz D., Voz C., Martin I., Orpella A., Puigdollers J., Alcubilla R., Villar F., Bertomeu J., Andreu J., Damon-Lacoste J., Roca i Cabarrocas P., Thin Solid Films 516, (2008) p.761

Nath P., Bunshah R.F., Basol B.M., Staffsud O.M., Thin Solid Films 72 (1980) p. 463

Nelson B., Iwaniczko E., Mahan A.H., Wang Q., Xu Y. Crandall R.S., Branz H.M., Thin Solid Films 395 (2001) p.292

Niikura C., Guillet J., Brenot R., Equer B., Bouree J.E., Voz C., Peiro D., Asensi J.M., Bertomeu J., Andreu J., J. Non-Cryst. Sol. 266 (2000) p.385

Nisha M., Anusha S., Antony A., Manoj R. and Jayaraj M.K., Appl. Surf. Sci. 252 (2005) p.1430

Ohring M., The materials science of thin films, Academic Press, (1992)

Olibet S., Vallat-Sauvain E., Ballif C., Physical Review B, 76, (2007) p.35326

Page M.R., Wang Q., Wang T.H., Yan Y., Johnston S.W., Ciszek T.F., Proc. Of 13th Workshop on Crystalline Silicon Solar Cell Materials and Processes, Colorado (2003)

Page, M. R., Iwaniczko, E., Xu, Y., Wang, Q., Yan, Y., Roybal, L., Branz, H. M., Wang, T. H., 4th IEEE World Conference on Photovoltaic Energy Conversion, Waikoloa, (2006) p. 6

Palik E. D., Handbook of Optical Constants of Solids, Academic, New York, (1991)

Peiró D., Ph.D. Thesis, University of Barcelona (1999)

Peumans P., Yakimov A., Forrest S.R., J . Appl. Phys. 93 (2003) p. 3693

Plagwitz H., Nerding M., Ott N., Strunk H.P., Brendel R., Prog. Photovolt: Res. Appl. 12, (2004) p.47

Puigdollers, J., Ph .D. Thesis, University of Barcelona (1995)

Radike M., Summhammer J., Prog. Photovolt: Res. Appl. 7, (1999) p.399

Ray S., Banerjee R., Basu N., Batabyal A.K. and Barua A. K., J. Appl. Phys. 54 (1983) p.3497

Roca i Cabarrocas P., Appl. Phys. Lett. 65 (13) (1994) p. 1674

Roca i Cabarrocas P., Hamma S., Sharma S.N., Viera G., Bertran E., Costa J., J. Non-Cryst. Solids 227 (1998) p. 871

Roca i Cabarrocas P., Kumar S., Drevillon B., J. Appl. Phys. 66 (7) (1989) p. 3286

Rose D., Koehler O., Kaminar N., Mulligan B., King D., IEEE 4th World Conference on Photovoltaic Energy Conversion, Waikoloa, (2006) p. 2018

Rose D., Powell R., Jayamaha U., Maltby M., Giolando D., McMaster A., Kormanyos K., Faykosh G., Dorer G., Conf. Rec. 28th IEEE Photovoltaic Spec. Conf. (2000) p.428

Staebler D.L., Wronski C.R., Appl. Phys. Lett., 31, (1977) p. 292

Scheer h., Economía solar, Estrategias para la modernidad ecológica, Círculo de Lectores-Galaxia Guttemberg. Barcelona, (2002)

Schlaf R., Murata H., Kafafi Z.H., Journal of Electron Spectroscopy and Related Phenomena 120 (2001) p.149

Schmidt J. and Aberle A.G., J. Appl. Phys. 85 (7) (1999) p. 3626

Schmidt J., and M. Kerr, Sol. Energy Mater. Sol. Cells 65 (2001), p. 585

Schmidt M., Korte L., Laades A., Stangl R., Schubert Ch., Angermann H., Conrad E., Maydell K.v., Thin Solid Films 515 (2007) p.7475

Schmidt W., Woesten B., Kalejs J.P., Prog. Photovolt: Res. Appl. 10(2) (2002) p. 129

Schneidorlöchner E., Preu R., Lüdemann R., Glunz S.W., Prog. Photovolt: Res. Appl. 10 (2002) p.29

Schropp R.E.I., Franken R.H., Goldbach H.D., Houweling Z.S., Li H., Rath J.K., Schüttauf J.W.A., Stolk R.L., Verlaan V. , van der Werf C.H.M., Thin Solid Films, In Press, Corrected Proof (2007)

Schropp R.E.I., Thin Solid Films 451 (2004) p. 455

Schropp R.E.I., Zeman M., Amorphous and Microcyrstalline Silicon Solar Cells: Modeling, Materials and Device Technology, Kluwer Academic Publishers (1998)

Schultz O., Riepe S., Glunz S. W., Proc. 19th PVSEC, Paris (2004) p.516

Schumacher J. O., Ph D thesis, Fraunhofer-Institut für Solare Energiesysteme Freiburg, (2000)

Seitz H., Bauer S., Dusane R. O., Schröder B., Thin Solid Films 395 (2001) p.120

Shockley W. and Read W.T., Phys. Rev. 87 (1952) p. 935

Sinton R., User Manual: WCT-100 Photoconductance Tool, Sinton Consulting, Boulder, CO, (1999)

Sinton R.A., Cuevas, A., Appl. Phys.Lett 69 (1996) p. 2510

Soler D., Ph.D. Thesis, University of Barcelona (2004)

Song Y.J. Anderson W.A., Solar Energy Materials & Solar Cells 64, (2000) p. 241

Spear W.E., Le Comber P.G., Solid State Communications 17 (1975) p. 1193

Stangl R, Froitzheim A, Elstner L, FuhsW., Proc. of the 17th EPVSEC, Munich, (2001) p.1387

Stangl R., Froitzheim A., Schmidt M., Fuhs W., 3rd World Conference on Photovoltaic Energy Conversion, Osaka (2003) p.1005

Stocks M.J., Weber K.J., A.W. Blakers A.W., Babaei J., Everett V., Neuendorf A., Kerr M. and Verlinden P.J., 3rd World Conference on Photovoltaic Solar Energy Conversion, Osaka, Japan (2003)

Stocks M.J., Weber K.J., A.W. Blakers A.W., Babaei J., Everett V., Neuendorf A., Kerr M. and Verlinden P.J., 3rd World Conference on Photovoltaic Solar Energy Conversion, Osaka, Japan (2003) p. 184

Street R.A., Hydrogenated Amorphous Silicon, Cambridge University Press, Cambridge (1991)

Sugiyama K., Ishii H., Ouchi Y., Seki K., J. Appl. Phys. 87 (2000) p. 295
Swanepoel R., J. Phys. E: Sci. Instrum., vol. 16, 1983, p.1214

Swanson, R.M., 19th European Photovoltaic Solar Energy Conference, Paris, (2004) p.1078

Sze M., Physics of semiconductor devices, 2nd ed. (Wiley, New York, 1981)

Sze S.M., Physics of semiconductor devices, Wiley & Sons, New York (1985)

Szlufcik J., Duerinckx F., Horzel J., E. Van Kerschaver E., Dekkers H., De Wolf S., Choulat P., Allebe C., Nijs J., Solar Energy Materials and Solar Cells 74, (2002) p. 155

Tadayyon S.M., Grandin H.M., Griths K. , Coatsworth L.L., Norton P.R., Aziz H., Popovic Z.D., Organic Electronics 5 (2004) p.199

Taguchi M., Kawamoto K., Tsuge S., Baba T., Sakata H., Morizane M., Uchihashi K., Nakamura N., Kiyama S., Oota O., Prog. Photovolt: Res. Appl. 8 (2000) p. 503

Taguchi M., Tanaka M., Matsuyama T., Matsuoka T., Tsuda S., Nakano S., Kishi Y., Kuwano Y. Technical Digest of the International PVSEC-5, Kyoto, (1990) p.689

Taguchi M., Terakawa A., Maruyama E., Tanaka M., Prog. Photovolt. Res. Appl. 13 (2005) p. 481

Tanaka M., Okamoto S., Tsuge S., Kiyama S., Proc. of the 3rd World Conf. PV Energy Conv., Osaka, (2003) p.955

Tauc J., Amorphous and Liquid Semiconductors, Plenum Press, London (1974)

Terzini E., Thilakan P., Minarini C., Materials Science and Engineering B77 (2000) p.110

Torres P., Meier J., Flückiger R., Kroll U., Anna Selvan J.A., Keppner H., Shah A., Appl. Phys. Lett. 69 (1996) p. 1373

Tsu D.V., Chao B.S., Ovshinsky S.R., Guha S., Yang J., Appl. Phys. Lett. 71 (10) (1997) p. 1317

Tsu R., González-Hernández J., Chao S.S., Lee S.C., Tanaka K., Appl. Phys. Lett. 40 (1982) p. 534

Tucci M., della Noce M., Bobeico E., Roca F., de Cesare G. Palma F., Thin Solid Films 451 (2004) p.355

Tucci M., Salurso E., Roca F., Palma F., Thin Solid Films 403 (2002) p. 307

Ulyashin A. G., Job R., Scherff M., Meizhen Gao, Fahrner W. R., Lyebyedyev D., Roos N. and. Scheer H., Thin Solid Films 403, (2002) p.359

Unold T., Rösch M., Bauer G.H., J. Non-Cryst. Solids 266 (2000) p.1033

Van Cleef M. W. M., Rath J. K., Rubinelli F. A., van der Werf C. H. M., Schropp R. E. I., van der Weg W. F., J . Appl. Phys 82, (1997) p. 6089

Van der Walle C.G., Neugebauer J., Applied Physics Letters 70, (1997) p. 2577

Van Hove L., Phys. Rev. 89 (1953) p. 1189

Van Veen M., Ph.D. Thesis, Utrech University (2003)

Van Veenendaal P.A.T.T., Gijzeman O.L.J., Rath J.K., Schropp R.E.I., Thin Solid Films 395 (2001) p. 194

Veschetti Y., Muller J.-C., Damon-Lacoste J., Roca i Cabarrocas P., Gudovskikh A.S., Kleider J.-P., Ribeyron P.-J. , Rolland E., Thin Solid Films 511, (2006) p. 543

Veschetti, Ph.D. Thesis, Université Louis Pasteur Strasbourg 1 (2005)

Villar F., Ph.D. Thesis, University of Barcelona (2008)

Voz C. , Peiro D., Bertomeu J., Soler D., Fonrodona M., Andreu J., Mater. Sci. Eng. B 69/79 (2000) p.278

Voz C., Martin I., Orpella A., Puigdollers J., Vetter M., Alcubilla R., Soler D., Fonrodona M., Bertomeu J. and Andreu J., Thin Solid Films 430 (2003) p.270

Voz C., Peiró D., Bertomeu J., Soler D., Fonrodona M., Andreu J., Materials Science and Engineering B 69-70 (2000) p. 278

Voz C., Ph.D. Thesis, University of Barcelona (2000)

Wald FV. In Crystals: Growth, Properties and Applications 5, Grabmaier J (ed.). Springer: Berlin, (1981) p. 147–198

Wang T.H., Iwaniczko E., Page M.R., Levi D.H., Yan Y., Branz H.M., and Wang Q., Yelundur V., Rohatgi A. Proc. of the 31st IEEE Photovoltaics Specialists Conference and Exhibition, Florida (2005)

Wang T.H., Iwaniczko E., Page M.R., Levi D.H., Yan Y., Branz H.M., Wang Q. Thin Solid Films 501 (2006) p.284

Wang T.H., Page M.R., Iwaniczko E., Levi D.H., Yan Y., Branz H.M., Yelundur V., Rohatgi A., Bunea G., Terao A., Wang Q., Proc. of 14th Workshop on Crys. Silicon Solar Cells and Modules, (2004)

Wang T.H., Wang Q., Iwaniczko E., Page M.R., Levi D.H., Teplin C.W., Xu Y., Wu X.Z., Branz H.M., Proceedings 19th European PVSEC (Paris) (2004), p. 1296

Wiesmann H., Gosh A.K., McMahon T., Strongin M., J. Appl. Phys. 64 (1979) p.3752

Winer K., Street R. A., Johnson N. M., Walker J., Phys. Rev. B 42, (1990) p. 3120

Yamamoto K., Nakajima A., Yoshimi M., Sawada T., Fukuda S., Suezaki T., Ichikawa M., Koi Y., Goto M., MeguroT., Matsuda T., Kondo M., Sasaki T., Tawada Y., Prog. Photovolt: Res. Appl. 13 (2005) p. 489

Zebaze Kana M.G., Centurioni E., Iencinella D. Summonte C., Thin Solid Films 500, (2006) p.203

Zedlitz R., Kessler F., Heintze M., J. Non-Cryst. Solids 164 (1993) p. 83

Zhao J, Wang A, Yun F, Zhang G, Roche DM, Wenham SR, Green MA. Progress in Photovoltaics: Research and Applications 5 (1997) p.269

Zhao J. H., Wang A. H., Green M. A., Ferrazza F., Appl. Phys. Lett. 73 (1998) p. 1991

Zhao J., Wang A., Green M.A, Prog. Photovolt: Res. Appl. 7 (6) (1999) p.471

Zhao J., Wang A., Yun F., Zhang G., Roche D.M., Wenham S.R., Green M.A., Progress Prog. Photovolt: Res. Appl. 5 (1997) p.269

List of figure captions

Figure 1.1: Territory size shows the proportion of the world population living in poverty living there (calculated by multiplying population by one of two poverty indices [http://www.worldmapper.org/]. The human poverty index uses indicators that capture non-financial elements of poverty, such as life expectancy, adult literacy, water quality, and children that are underweight. [http://hdr.undp.org]).

Figure 1.2: Territory size shows the proportion of all people with some electrical power in their homes living there [http://www.worldmapper.org/]. Electricity access includes that sourced from a publicly used grid and self-generated electricity. This map shows access, not the quantities of electricity used. The percentage of people with access to electricity in their own homes is over 97% in Eastern Asia, Eastern Europe, North America, Western Europe and Japan. 7 of the 10 territories with the lowest access to electricity are in Africa.

Figure 1.3: Amount of solar energy in hours, received each day on an optimally tilted surface during the worst month of the year.

Figure 1.4: First solar cells and modules by Bell laboratories.

Figure 1.5: PERL (passivated emitter, rear locally-diffused) solar cell structure fabricated by the group of M. Green at University of New South Wales [Zhao et al., 1999].

Figure 1.6: Very thin solar cell (20.2% on 37 μm) fabricated at ISE. They have also the record 21.2% on a 75 μm wafer without wafer warpage [Glunz et al., 2005].

Figure 1.7: Structure of the bifacial heterojunction solar cells fabricated by Sanyo.

Figure 1.8: Scheme of the fabrication steps for a conventional solar cell compared to an heterojunction device. The temperatures involved in the different fabrication steps are indicated [Roca et al., 2004].

Figure 2.1: Diagram of the fabrication steps followed to obtain the complete solar cell.

Figure 2.2: CZ and FZ processes for the production of monocrystalline silicon ingots.

Figure 2.3: band diagram of n-type (a) and p-type (b) bifacial heterojunction devices [Wang et al., 2004].

Figure 2.4: dependence of the Voc with the diffusion length for p- and n-type wafers with different surface recombination velocities [Jensen et al., 2003]

Figure 2.5: Relation between the wafer thickness and the efficiency of a solar cell for different diffusion lengths (L_n) and surface recombination velocities (S_{0back}). A good surface passivation (S_{0back} < 100 cm/s) is essential for thinner wafers (< 200 μm) [Aberle, 2000].

Figure 2.6 Effective lifetime vs minority carrier density curves measured by QSSPC for the same emitter deposited either on the native oxide (○) or in a sample where it has been totally removed (□).

Figure 2.7: Schematic representation of the processes involved in the HWCVD technique.

Figure 2.8: Picture of the multichamber HWCVD set-up. The system was ensembled by the Scientific-Technical Services of Universitat de Barcelona.

Figure 2.9: Internal arrangement of the different components inside the HWCVD chamber.

Figure 2.10: Tantalum wire during a HWCVD process.

Figure 2.11: Thickness variation for an a-Si:H film deposited by HWCVD with the double wire configuration. The dotted lines indicate the inhomogeneity of a 2x2 cm^2 square area.

Figure 2.12: Deposition rate vs. RF power for layers deposited at room temperature (RT) and at 260ºC.

Figure 2.13: Device active area definition and etching of the doped a-Si:H emitter to avoid lateral leakage currents.

Figure 2.14: picture of one of the metallic masks used to evaporate the grid contact and example of two different patterns for 1 cm^2 solar cells.

Figure 3.1: Possible structural configurations of Hydrogen in the a-Si:H.

Figure3.2: Picture of the Jovin Yvon UVISEL set-up located at the LPICM in Paris.

Figure 3.3: Schematic of the Spectroscopic Phase Modulated Ellipsometry measurement in the UV-visible.

Figure 3.4: Imaginary part of the pseudo-dielectric function of c-Si, a-Si:H and μc-Si:H samples.

Figure 3.5: Dependence of τ_b on Δn with a base doping $N_A = 4.3\times10^{15}$ cm^{-3}, $\tau_{n0} = \tau_{p0} =$ 2.5 ms. At low-injection, τ_b is mainly determined by τ_{SRH}. On the other hand, at high-injection τ_b is dominated by Auger recombination [Martin, 2004].

Figure 3.6: Block diagram of the QSSPC set-up.

Figure 3.7: Effective lifetime vs. Average excess carrier density measured by the QSSPC technique. The arrow points the effective lifetime at 1 sun irradiance. In the inset, implicit-V_{oc} *vs* irradiance for the same sample.

Figure 3.8: Dark JV curves of a solar cell measured with 2, 3 and 4 probes.

Figure 3.9: Typical JV curve of a solar cell measured under standard AM1.5 irradiance.

Figure 3.10: Comparison of the SR, EQE, IQE and R curves measured for the same heterojunction solar cell.

Figure 4.1: Raman measurements for the samples deposited at different process pressures (see table 4.2).

Figure 4.2: FTIR measurements for the samples deposited at different process pressures (see table 4.2).

Figure 4.3: Values of σ_d and S for the samples deposited at different process pressures (see table 4.2).

Figure 4.4: Optical absorption coefficient of a reference a-Si:H layer deposited by PECVD compared to the Mp sample. The absorption coefficient was measured by PDS.

Figure 4.5: Raman measurements for the series of samples in table 4.3.

Figure 4.6: Dependence of crystallinity with all the other deposition parameters for intrinsic layers [Villar, 2008].

Figure 4.7: Raman measurements for the samples obtained varying the T_f.

Figure 5.1: Diagram of the two precursors used in this work: with a back a-SiC_x passivating layer deposited by PECVD (left) and bifacial precursor with the same layer on both sides (right).

Figure 5.2 Band diagram for a (n)a-Si:H/(p)c-Si heterojunction emitter.

Figure 5.3: Calculated V_{oc} according to equation 5.11 as a function of S_{it}. The value of Φ_c is considered 0.95 eV in all cases. Different diode ideality factors were also considered to study their influence.

Figure 5.4 Ellipsometry data (symbols) and fitting curves (lines) for an optimized a-Si:H/c-Si heterojunction emitter. On the right, model deduced from the effective media approximation.

Figure 5.5 Effective lifetime (τ_{eff}) as a function of the excess minority carrier density for an heterojunction emitter (n)a-Si:H/(i)a-Si:H/(p)c-Si. The arrow points the most significant values at one-sun.

Figure 5.6: Comparison between the Im(ε) of the same (n)a-Si:H layer deposited onto a c-Si wafer with and without an a-Si:H buffer layer. The model of the c-Si and a-Si:H are also shown for comparison.

Figure 5.7: High resolution TEM image of the sharp NREL amorphous/crystalline interface. The line indicates the interface [Mahan, 2006].

Figure 5.8: SE measurements (o) compared to the fitting (lines) of a 7 nm (i) a-Si:H. In the inset, the a-Si:H deposited by HWCVD used for the fitting compared to the standard a-Si:H. The parameters of the a-Si:H derived from the Tauc-Lorenz model are also shown.

Figure 5.8: Imaginary part of the pseudodielectric function of four heteroemitter configuration with different HWCVD H-treatments before the a-Si:H layers deposition.

Figure 5.9: Imaginary part of the pseudodielectric function of the initial heterojunction emitter compared to different post -treatments: hydrogenation and thermal annealing.

Figure 5.10: Imaginary part of the pseudo dielectric function for three heterojunction emitters with different n-doped layer thicknesses. The lines correspond to fittings of the experimental data using the Bruggemann effective media approximation. The corresponding models are shown in the enclosed table.

Figure 5.11 Internal Quantum Efficiency curves for solar cells fabricated with three different n-doped layer thicknesses.

Figure 5.12: Band diagram of a (p$^+$)a-Si:H/(p)c-Si (right) and (p$^+$)μc-Si:H/(p)c-Si heterojunction (left).

Figure 5.13: Implicit-V_{oc} values obtained by QSSPC as a function of the diborane flow for the two filament temperatures considered.

Figure 5.14: SE Measurements of the p-doped layers under study.

Figure 5.15: SE Measurements of the sample compared with the μc-Si:H models. The dashed line corresponds to the fitting of the experimental curve.

Figure 5.16: Band diagram of a (p)μc-Si:H/(i)a-Si:H/(p)c-Si back contact. The structure for an a-Si:H p-layer would be similar to the one showed in figure 5.12.

Figure 5.17: Implicit-Voc values measured by QSSPC for a series of diborane concentrations at low filament temperature. The results obtained with buffer layer (●) are compared to those obtained for simple heterojunctions (○).

Figure 5.18: Implicit-V_{oc} values measured by QSSPC for a doping series obtained at high filament temperature. The results obtained with (■) and without buffer layer (□) are compared.

Figure 6.1: Resistivity measured by four-probes and refraction index measured by ellipsometry for samples deposited by sputtering with different RF power.

Figure 6.2: Reflectance of ITO layers of different thickness deposited on c-Si compared with the AM1.5 Solar Spectrum.

Figure 6.3: XRD Measurements for the ITO samples deposited at room temperature and at 260ºC.

Figure 6.4: Resistivity and refraction index measured by four points and ellipsometry respectively for different oxygen partial pressures.

Figure 6.5: Band diagram of the ITO/(n)c-Si Schottky diodes.

Figure 6.6: ITO work function vs. Oxygen partial pressure.

Figure 6.7: JV measurements at AM1.5 irradiance for two solar cells with different active area.

Figure 6.8: Initial and after dry-etching JV characteristics of a solar cell measured in dark (a) and illuminated under AM1.5 conditions (b). The lateral leakage current is reduced in about three orders of magnitude with a consequent FF increase in more than 10%.

Figure 6.9: Specific contact resistance of different metallic contacts evaporated on ITO layers. The inset shows the mask used for the evaporation process.

Figure 6.10: JV characteristics measured in AM1.5 conditions for two heterojunction solar cell s on Al-BSF with different Ag grid thicknesses.

Figure 6.11: Reflectance spectra of the front ITO layer before and after evaporating the 1 μm thick silver grid. The curve with the light spot over the fingers is very close to the theoretical value.

Fig. 6.12: JV electrical characteristics measured under AM1.5 illumination (100mW·cm^{-2}) for the fabricated heterojunction solar cells.

Fig. 6.13: EQE curves of the fabricated heterojunction solar cells. The emitter thickness and microstructure clearly influenced the response at shorter wavelengths.

Figure 6.14: Picture and scheme of the fabricated bifacial heterojunction solar cells.

Figure 6.15: QSSPC data for the symmetric emitter and symmetric BSF structures compared to the solar cell precursor. The arrows point the values at 1 sun irradiance.

Figure 6.16: JV characteristics measured under AM1.5 irradiance (100 mW·cm^{-2}) for the fabricated double-side heterojunction solar cells.

Figure 6.17: External Quantum Efficiency curves of the double-side heterojunction solar cells with P and IP BSF contacts compared to the case with a traditional Al-BSF contact.

List of Table Captions

Summary in Spanish

El elevado coste de producción de los módulos de silicio cristalino (c-Si) de alta eficiencia dificulta el progreso de la industria fotovoltaica como una alternativa viable para la producción de energía limpia. Por esta razón, los fabricantes de células solares buscan diferentes alternativas para conseguir la deseada reducción de costes. Por ejemplo, considerando que las obleas de c-Si representan aproximadamente el 30 - 50 % en el precio del módulo, una opción es reducir el grosor de las obleas (< 200 μm) para obtener así más obleas por lingote. Sin embargo, si se reduce el grosor del sustrato es indispensable reducir también la recombinación superficial puesto que ésta es crítica para mantener altas eficiencias en los dispositivos. Aunque la superficie del c-Si puede pasivarse eficientemente mediante una oxidación térmica, las obleas delgadas tiendan a doblarse en estos procesos de alta temperatura (~ 1000°C). Por otra parte, el silicio multicristalino de bajo coste tampoco es compatible con pasos a alta temperatura debido a la fuerte degradación del tiempo de vida en el volumen. Por este motivo, métodos alternativos de pasivación a baja temperatura han ganado un especial interés debido a su compatibilidad tanto con sustratos delgados como con obleas de baja calidad o bajo coste.

Más concretamente, las células solares de heterounión en que se utilizan capas de silicio amorfo (a-Si:H) depositadas a baja temperatura sobre obleas de c-Si han ganado interés en la comunidad fotovoltaica debido a su alta eficiencia y rentabilidad. Sanyo ha conseguido eficiencias de más del 19% en módulos producidos industrialmente con la estructura denominada HIT (heterounión con capa intrínseca delgada). La novedad de este dispositivo es la introducción de una capa de silicio amorfo intrínseco muy delgada (5 nm) entre el c-Si y la capa dopada. Esta capa reduce drásticamente la velocidad de recombinación en la interfaz consiguiéndose así tensiones de circuito abierto por encima de 700 mV. La mayoría de grupos, incluido Sanyo, usan el depósito químico en fase vapor asistido por plasma de radiofrecuencia (PECVD) para obtener el silicio amorfo. Recientemente, la técnica de depósito asistida por filamento caliente (HWCVD) también ha demostrado un gran potencial para fabricar células de heterounión de alta eficiencia. En la técnica HWCVD, además de algunas ventajas tecnológicas, la ausencia de bombardeo iónico reduce el daño en la superficie del c-Si mejorando así las propiedades en la interfaz.

En este trabajo, hemos concentrado nuestro esfuerzo en la optimización de todos los pasos de fabricación para obtener células solares de heterounión obtenidas por HWCVD en un proceso completamente desarrollado a baja temperatura (200ºC). Primero, hemos optimizado el material obtenido por HWCVD variando los diferentes parámetros de depósito (presión, temperatura de filamento, flujos de hidrógeno y silano, nivel de dopaje, temperatura de sustrato) para obtener silicio amorfo y microcristalino de buena calidad. Se han conseguido buenas propiedades estructurales, eléctricas y ópticas tanto para material intrínseco como en capas dopadas.

Posteriormente, hemos optimizado el emisor de heterounión sobre sustratos tipo p de c-Si. En particular, se ha estudiado en profundidad la influencia de la capa intrínseca de a-Si:H así como de diferentes pretratamientos de hidrógeno en la superficie del c-Si. Se han realizado tanto estudios de microestructura con Espectroscopía por Elipsometría Óptica, como medidas de pasivación mediante Fotoconductancia en Estado Cuasiestacionario. Estos estudios han permitido optimizar los precursores de células solares hasta obtener tensiones implícitas de circuito abierto por encima de 690 mV. A continuación se ha desarrollado el electrodo frontal atendiendo a los requerimientos ópticos y eléctricos. Por una parte, se ha optimizado la capa antirreflectante (Oxido de Indio dopado con Estaño) en términos de resistividad ($\rho < 4\times10^{-4}\Omega$cm) y de reflectancia. Luego se ha diseñado el peine metálico frontal intentando obtener un buen compromiso entre resistencia serie y factor de sombra. Una vez optimizado todo por separado, se han podido fabricar células solares completas con una eficiencia de conversión de hasta el 15.4% sobre obleas de silicio CZ tipo p planas (14 Ωcm). En estos dispositivos se ha utilizado un contacto posterior de aluminio recocido a alta temperatura (Al-BSF).

Finalmente, hemos investigando la posibilidad de incorporar contactos posteriores depositados a baja temperatura basados en capas de silicio amorfo dopadas con boro obtenidas por HWCVD. Estas capas se utilizarían para sustituir los contactos tradicionales de Al-BSF a alta temperatura. Igual que se hizo para el emisor, hemos estudiado también la influencia de los diferentes parámetros de depósito así como el efecto de intercalar una capa intrínseca delgada. Hasta el momento, las células solares con doble heterounión fabricadas completamente por HWCVD han alcanzado una eficiencia de conversión del 14.5% en un proceso completo a baja temperatura (< 200ºC). Considerando el carácter preliminar de estos dispositivos, éste es un punto de partida realmente prometedor para células solares de heterounión bifaciales fabricadas por HWCVD.